

**Electromechanical Modeling of Encapsulated Ionic Polymer
Transducers**

by

John W. Franklin

Thesis submitted to the Faculty of the
Virginia Polytechnic Institute and State University
in partial fulfillment of the requirements for the degree of

Master of Science

in

Mechanical Engineering

Donald J. Leo, Chair
Daniel J. Inman
Harry H. Robertshaw

May 2003
Blacksburg, Virginia

Keywords: ICMP, EAP, Nafion, encapsulation, modeling, characterization

Copyright by John W. Franklin, 2003

Electromechanical Modeling of Encapsulated Ionic Polymer Transducers

John W. Franklin, M.S.

Virginia Polytechnic Institute and State University, 2003

Advisor: Donald J. Leo

Abstract

A model to allow the design and evaluation of encapsulated ionic polymer transducers is developed. This model is based on a linearly coupled, two port, electrical equivalent circuit model (Newbury, 2002). The proposed model incorporates multilayer beam theory to model the passive stiffness effects of the encapsulation layer and attempts to increase the prediction accuracy of the model by using distributed parameter system modeling to create the mechanical terms used in the model. Modal expansion is used to extend the applicability of the mechanical impedance terms through multiple resonances of the transducer. The test setup as well as the mathematical approach to characterize the viscoelastic properties of NafionTM as they relate to this work is described and the results presented. The model simulation is then compared to measured experimental data taken for a number of ionic polymer-metal composites before and after encapsulation. The applicable frequency range of the model is explored as well as data trends seen above previous frequency ranges ($\sim 1\text{kHz}$).

Free deflection was predicted to reduce by an order of magnitude when the transducers were encapsulated with KaptonTM. This trend was observed and correlates well with the measured response. Charge sensing and blocked force were found to increase for a transducer after encapsulation, this could be due to the higher coherence obtained in testing after encapsulation and is not predicted by the model. The model predicts charge sensing and blocked force should remain constant with encapsulation. Low frequency blocked force data for any given transducer was observed to be roughly an order of magnitude greater than the sensing response, before and after encapsulation. There is no explanation for this observation, future work should investigate this phenomenon.

Acknowledgments

I would like to acknowledge many people for their thoughts and support throughout my research adventure here at Tech.

- My advisor Dr. Donald Leo for his guidance, enthusiasm, thoughts, advice, and certainly the funding to be here.
- Dr. Daniel Inman and Dr. Harry Robertshaw for their insight and support.
- Mr. Barbar Akle, Mr. Matt Bennett, Mr. Kevin Farinholt and Mr. Curt Kothera for their help and ideas throughout this project.
- The rest of the CIMSS crew for making this a great place to be.
- My wife Jennifer for her often undeserved patience and love.
- My parents for their guidance and unfaltering support throughout my life in whatever I have undertaken.

and to anyone I have forgotten to mention, thank you.

Contents

| | |
|---|------------|
| Abstract | ii |
| List of Tables | vi |
| List of Figures | vii |
| Chapter 1 Introduction | 1 |
| 1.1 General History of Ionic Polymers | 1 |
| 1.2 Motivation for Research | 2 |
| 1.3 Literature Review | 3 |
| 1.4 Research Goals and Contributions | 6 |
| 1.5 Thesis Overview | 6 |
| Chapter 2 Three-Layer-Beam Model Development | 8 |
| 2.1 Lumped Parameter System Model | 9 |
| 2.1.1 Mechanical Terms | 9 |
| 2.1.2 Electrical Terms | 12 |
| 2.1.3 Lumped Parameter Model Comparison | 14 |
| 2.2 Distributed Parameter System Modeling | 17 |
| 2.2.1 Cantilever Boundary Conditions | 17 |
| 2.2.2 Transfer Function Analysis and Modeling of Test Fixture | 19 |
| 2.2.3 Incorporation of Viscoelastic Damping | 21 |
| 2.3 Experimental Testing Setup | 22 |
| 2.3.1 Post Processing of Data | 26 |

| | | |
|---------------------|---|------------|
| Chapter 3 | Viscoelastic Parameter Identification | 29 |
| 3.1 | Viscoelastic Parameters and Test Setup | 29 |
| 3.2 | Minimization Approach | 32 |
| 3.3 | Data Validation | 35 |
| 3.4 | Kapton TM Characterization | 36 |
| Chapter 4 | Three-Layer-Beam Model Verification | 40 |
| 4.1 | Model Parameters | 41 |
| 4.2 | Electrode Stiffness Effects | 43 |
| 4.3 | Low Frequency Range Model Comparison | 44 |
| 4.3.1 | Base Transducer Mechanics (Unencapsulated) | 44 |
| 4.3.2 | Kapton TM Encapsulated Transducers | 53 |
| 4.4 | Higher Frequency Data Observations | 62 |
| 4.4.1 | Non Encapsulated Transducers | 62 |
| 4.4.2 | Encapsulated Transducers | 65 |
| Chapter 5 | Discussion and Conclusions | 67 |
| 5.1 | Summary of Results | 67 |
| 5.2 | Future Work | 70 |
| Bibliography | | 72 |
| Appendix A | Full Results Plots | 75 |
| Vita | | 100 |

List of Tables

| | | |
|-----|---|----|
| 3.1 | Summary of GHM parameter fitting results for Nafion TM | 36 |
| 3.2 | Summary of GHM parameter fitting results for Kapton TM | 38 |
| 4.1 | Transducer geometry used for model verification | 41 |
| 4.2 | Summary of parameters used in model validation | 42 |
| 4.3 | Table of comparison of low frequency transducer response change with en- capsulation | 61 |

List of Figures

| | | |
|------|--|----|
| 2.1 | Electrical equivalent circuit model (Newbury and Leo, 2003a) | 9 |
| 2.2 | Cross section of 3 layer beam model | 9 |
| 2.3 | System used for model derivation | 10 |
| 2.4 | Transducer dimensions used in sliding-pin model adaptation. | 19 |
| 2.5 | Models for linear viscoelasticity | 22 |
| 2.6 | Diagrams of various test setups | 24 |
| 2.7 | Picture of testing setup | 25 |
| 2.8 | Close up of polymer and load cell fixture | 25 |
| 2.9 | Load cell and signal conditioning circuit modeling | 27 |
| 2.10 | Typical stiffness (f/u) run processed | 28 |
| 3.1 | GHM fitting results for run10 | 33 |
| 3.2 | GHM fitting results for run08 | 34 |
| 3.3 | Modulus curves for Nafion TM GHM fitting results | 35 |
| 3.4 | Kapton TM GHM fitting results for run 2 | 38 |
| 3.5 | Modulus curves for Kapton TM GHM fitting results | 39 |
| 4.1 | Electroplated sample vs single layer model (Nafion TM) | 43 |
| 4.2 | Stiffness test results of electroplated samples | 44 |
| 4.3 | Stiffness test results vs model for unencapsulated transducer I | 45 |
| 4.4 | Stiffness test results vs model for unencapsulated transducer III | 46 |
| 4.5 | Free deflection test results for unencapsulated transducer I | 47 |
| 4.6 | Free deflection test results for unencapsulated transducer III | 48 |
| 4.7 | Sensing test results for unencapsulated transducer I | 49 |
| 4.8 | Sensing test results for unencapsulated transducer III | 50 |

| | | |
|------|--|----|
| 4.9 | Blocked force test results for unencapsulated transducer I | 51 |
| 4.10 | Blocked force test results for unencapsulated transducer III | 51 |
| 4.11 | Electrical impedance test for unencapsulated transducer I | 52 |
| 4.12 | Electrical impedance test for unencapsulated transducer III | 53 |
| 4.13 | Stiffness test results vs model for encapsulated transducer III | 54 |
| 4.14 | Stiffness test results vs model for encapsulated transducer I | 54 |
| 4.15 | Free deflection test results for encapsulated transducer III | 55 |
| 4.16 | Free deflection test results for encapsulated transducer I | 56 |
| 4.17 | Sensing test results for encapsulated transducer III | 57 |
| 4.18 | Sensing test results for encapsulated transducer I | 57 |
| 4.19 | Blocked force test results for encapsulated transducer III | 58 |
| 4.20 | Blocked force test results for encapsulated transducer I | 59 |
| 4.21 | Electrical impedance test for encapsulated transducer III | 59 |
| 4.22 | Electrical impedance test for encapsulated transducer I | 60 |
| 4.23 | Free deflection of encapsulated transducer III with low Kapton TM GHM fit | 61 |
| 4.24 | Stiffness of encapsulated transducer III with low Kapton TM GHM fit | 62 |
| 4.25 | Free deflection response of unencapsulated transducer III, full frequency range. | 63 |
| 4.26 | Sensing response of unencapsulated transducer I, full frequency range. . . . | 64 |
| 4.27 | Blocked force response of unencapsulated transducer I, full frequency range. | 65 |
| 4.28 | Free deflection response of encapsulated transducer III, full frequency range. | 66 |
| 4.29 | Sensing response of encapsulated transducer III, full frequency range. . . . | 66 |
| A.1 | Unencapsulated transducer I stiffness. | 76 |
| A.2 | Unencapsulated transducer I free deflection. | 76 |
| A.3 | Unencapsulated transducer I charge sensing. | 77 |
| A.4 | Unencapsulated transducer I blocked force. | 77 |
| A.5 | Unencapsulated transducer I electrical impedance. | 78 |
| A.6 | Unencapsulated transducer II stiffness. | 79 |
| A.7 | Unencapsulated transducer II free deflection. | 79 |
| A.8 | Unencapsulated transducer II charge sensing. | 80 |
| A.9 | Unencapsulated transducer II blocked force. | 80 |
| A.10 | Unencapsulated transducer II electrical impedance. | 81 |

| | |
|--|----|
| A.11 Unencapsulated transducer III stiffness. | 82 |
| A.12 Unencapsulated transducer III free deflection. | 82 |
| A.13 Unencapsulated transducer III charge sensing. | 83 |
| A.14 Unencapsulated transducer III blocked force. | 83 |
| A.15 Unencapsulated transducer III electrical impedance. | 84 |
| A.16 Unencapsulated transducer IV stiffness. | 85 |
| A.17 Unencapsulated transducer IV free deflection. | 85 |
| A.18 Unencapsulated transducer IV charge sensing. | 86 |
| A.19 Unencapsulated transducer IV blocked force. | 86 |
| A.20 Unencapsulated transducer IV electrical impedance. | 87 |
| A.21 Encapsulated transducer I stiffness. | 88 |
| A.22 Encapsulated transducer I free deflection. | 88 |
| A.23 Encapsulated transducer I charge sensing. | 89 |
| A.24 Encapsulated transducer I blocked force. | 89 |
| A.25 Encapsulated transducer I electrical impedance. | 90 |
| A.26 Encapsulated transducer II stiffness. | 91 |
| A.27 Encapsulated transducer II free deflection. | 91 |
| A.28 Encapsulated transducer II charge sensing. | 92 |
| A.29 Encapsulated transducer II blocked force. | 92 |
| A.30 Encapsulated transducer II electrical impedance. | 93 |
| A.31 Encapsulated transducer III stiffness. | 94 |
| A.32 Encapsulated transducer III free deflection. | 94 |
| A.33 Encapsulated transducer III charge sensing. | 95 |
| A.34 Encapsulated transducer III blocked force. | 95 |
| A.35 Encapsulated transducer III electrical impedance. | 96 |
| A.36 Encapsulated transducer IV stiffness. | 97 |
| A.37 Encapsulated transducer IV free deflection. | 97 |
| A.38 Encapsulated transducer IV charge sensing. | 98 |
| A.39 Encapsulated transducer IV blocked force. | 98 |
| A.40 Encapsulated transducer IV electrical impedance. | 99 |

Chapter 1

Introduction

1.1 General History of Ionic Polymers

Electroactive Polymers (EAP) and specifically ionic EAP's are a class of polymers that exhibit coupling between the mechanical and electrical domains. This characteristic makes them suitable for use as flexible transducers. This coupling is thought to be due to the mobility of cations in the polymer network. They are often referred to as IPMC (Ionomeric Polymer-Metal Composite) (Shahinpoor et al., 1998) because of the metal deposited on the surface of the polymer for electrodes to facilitate electrical signal transmission to and from the polymer. An example of the electromechanical coupling observed is if an electric potential is applied across the material a deformation of the polymer is observed and conversely imposing a deformation on the polymer produces an electrical signal. Actuation voltages are typically low, on the order of 1-10 volts. The actuation response was first discovered by three groups of researchers in 1992: Oguro et al. in Japan, Shahinpoor, and Sadeghipour et al. on the United States (Bar-Cohen, 2001). Other researchers are currently investigating IPMC and their modeling contributions will be discussed in the literature review section. Two popular types of base materials are used for IPMC, NafionTM (perfluorosulfonate), produced by Dupont, and FlemionTM(perfluorocarboxylate), produced by Asahi Glass, Japan. Before their use as IPMC they were widely used as membranes in fuel cells. Other polymers are being developed in an attempt to overcome some of the limitations associated with these materials, such as stiffness and hydration. NafionTM (used in this work) is relatively soft (static modulus of as low as 64MPa when hydrated) especially compared to other electromechanically coupled materials such as piezo ceramics. The electrodes are

typically created by introducing metal ions (typically Platinum because of its resistance to corrosion) throughout the polymer and then reducing the ions to their metal form in another solution, this occurs at the surface and creates a conductive electrode. This conductive layer can be further enhanced as an electrode by depositing a highly conductive metal to the Pt base layer, typically Gold. For a detailed description of a new process and review of other processes see Bennett (2002). Ionic content has been linked to transducer performance (Nemat-Nasser and Thomas, 2001) and Lithium (Li+) has been shown to generally produce the best results in NafionTM, which is the material and ion used throughout this work. This phenomena, like almost all aspects of IPMC is still under investigation by numerous researchers around the world. The following section will present the motivation for this work.

1.2 Motivation for Research

This work was inspired by the interest in the research of small ionic polymer transducer array performance and applications. The NafionTM samples utilized for preliminary application were $50\mu\text{m}$ thick cantilevered beams measuring approximately 1mm wide with a free length of approximately 4mm. This transducer geometry is a large deviation from the typical size of transducer used in Newbury and Leo (2003a) and Newbury and Leo (2003b) (approx $200\mu\text{m}$ thick by 5mm by 20mm). Preliminary free deflection results indicated a considerable reduction of amplitude when the measured data was compared to the response predicted by the work of Newbury and Leo (2003b). This reduction was thought to possibly be due to a contribution of the electrodes as a passive stiffness not modeled in Newbury and Leo (2003a). The sensors did however have adequate sensing performance indicating that it was not just a poorly fabricated batch of transducers.

This result is motivation along with the lack of existing modeling capability to predict and evaluate encapsulated transducer performance both in general and in Newbury and Leo (2003a). Encapsulation is one of the methods under investigation for the solution of the ongoing problem of maintaining hydration for optimal performance of ionic polymer transducers used in air, as well as where it is necessary to isolate the polymer from its environment. The first path taken was to generalize a three-layer-beam model adaptation for the mechanical aspects of the model presented in Newbury (2002). This result was

then remodeled using distributed parameter system modeling of the transducer and with improvements in test apparatus the frequency range of observation and comparison was extended. This process, results, and validation will be the focus of this work.

1.3 Literature Review

The modeling of ionic polymers in the past has generally consisted of two approaches. One earlier method models the response of a transducer with various parameters to match measured responses. This is more of an empirical type of model, the parameters are found by fitting the model to the measured response. This type of model was first developed when there was very little knowledge of ionic polymer dynamics but a need for a model to evaluate implementation of EAP's into various possible applications. Most early models focused on the modeling of actuation. An example of this type of model can be found in Kanno et al. (1994) and is referred to as a black-box model because only input and output relationships are modeled by a time-series where the parameters are determined for each transducer for a desired relationship. This model is therefore only applicable to the particular scenario and must be recomputed and used separately for other transducers, inputs and/or outputs. Another example is the model proposed in Tadokoro et al. (2000) where a white-box model is proposed. White box refers to the fact that some parameters are still found empirically, but the model also has some terms based on physical principles. This model is based on the relationship between three transducer properties, electrical, stress generation, and mechanical. Tadokoro et al. (2000) proposed that a voltage applied to the transducer causes mobile cations to move from the anode (positive) to the cathode (negative) side of the transducer, pulling water with along too. This water distribution causes a swelling of one side and a shrinking of the other, creating a curvature of the sample. Osmotic pressure then causes the water to redistribute, causing the transducer to slowly return to near its starting position. Removal of the voltage redistributes the cations and pulls water again causing a motion in the opposite direction as the initial motion. This model results in a system of coupled partial differential equations that can be simplified and solved. The equations are composed of relationships between physical and chemical parameters not well understood or directly measurable. They did however show good data correlation between measured and predicted motion.

The other type of model attempts to model the underlying microscopic physics and resulting transducer response. These models are not usually well suited for an engineering application because of the complexity of the resulting equations. Nemat-Nasser and Li (2000) proposed a micromechanics model based on coupled three dimensional field equations. The constitutive parameters in the model are estimated based on the microstructure of the transducer using micromechanics or by experimental measurement. Nemat-Nasser and Li (2000) proposed that the cations in the transducer migrate under an applied field and the anions that are attached to the backbone of the polymer move in an attempt to rebalance the local charge, this electrostatic motion creates the motion of the polymer and water migration and hydrostatics are secondary phenomena. This explanation of actuation is much different than the treatment of Tadokoro et al. (2000) where water migration was the primary cause of motion. Nemat-Nasser and Li (2000) explain sensing in ionic polymers by the stress created by motion displaces the charge center of the ionic cluster and the resulting dipole creates a voltage across the electrodes of the transducer. The equations needed to describe an ionic polymer transducer in this model are much more complicated than is desirable for engineering and the applications of ionic polymer transducers. Since then, Nemat-Nasser has focused on the micro-mechanics associated with the phenomenon of actuation in ionic polymers (Nemat-Nasser, 2002).

These two types of models both have drawbacks from an engineering design standpoint. The first type lacks the scalability and physical relevance of terms, the second lacks simplicity and macroscopic relevance of the terms and equations involved. The ideal design model would consist of easily obtainable material properties and easily measurable transducer dimensions. This lack of design models leaves a niche to fill, and the following model attempts to fill it. The model proposed in Newbury (2002) and Newbury and Leo (2003a) attempts to address these issues and provide a linearly coupled set of equations that allow scaling of transducers and their performance prediction without having to redetermine parameters in the model. The model proposed is a two-port equivalent electrical circuit. The resulting pair of linearly coupled equations relate current and force to velocity and voltage in the polymer. The terms in the equations contain measurable macroscopic physical and electrical properties of the transducer as well as its geometry. Material parameters include the modulus, density, and electrical permittivity. Since NafionTM is viscoelastic (Uan-Zo-li, 2001), the modulus is a function of frequency, and since ionic polymers are not purely ca-

capacitive or resistive, the electrical permittivity is also a function of frequency. The coupling within the polymer is also modeled as a function of frequency. This allows the scaling of transducers without having to redetermine coefficients in the equations. This model allows the prediction of various input-output relationships and was validated in Newbury (2002) and Newbury and Leo (2003b) for different transducer sizes for a frequency range of up to 20Hz. The model does not try to explain or incorporate the fundamental phenomena within the transducer but rather provides an engineering model useful in the design and application of ionic polymer transducers. One of the limitations with this model is the relatively low frequency range of validation; higher frequency exploration has not been performed. Another limitation is that the model proposed by Newbury (2002) also uses a measured bulk modulus, which for an existing manufacturing process and typical transducer size is adequate, but allows no insight into the effect of various encapsulation materials on transducer applications.

Encapsulation applied to ionic polymer transducers is a subject readily acknowledged but very little has been published regarding passive encapsulation of IPMC. To the best of the author's knowledge, nothing has been presented regarding modeling the change in transducer performance with passive encapsulation. It was noted in Shahinpoor et al. (1998) that encapsulation of transducers in Saran plastic membrane reduced the vibration amplitude observed by a cantilever sample. The goal of encapsulation here was to keep the transducer hydrated longer and extend the time between rehydration cycles. No evaluation of other encapsulation materials is noted, and no modeling is presented. This is typical of most literature encountered related to encapsulated ionic polymer transducers. The multilayered transducer work presented in Akle (2003) deals with encapsulation of ionic polymer transducers as insulation layers in stacks. The encapsulation/insulation material used was also Saran plastic, and similar results were reported to those of Shahinpoor et al. (1998), reduced free deflection amplitude after encapsulation. The Newbury and Leo (2003a) model adapted in Akle (2003) to multilayer transducer applications was modified and the encapsulation layers were effectively neglected, which for Saran in that application was determined to be valid. The KaptonTM film used in this work is much stiffer than Saran and does not allow the same simplification (this will be justified in Chapter Four).

1.4 Research Goals and Contributions

The goals of this work include the development of a model incorporating a multilayered beam approximation into the ionic polymer model developed in Newbury (2002) and Newbury and Leo (2003a). The NafionTM is treated as the active inner layer with a passive layer laminated to the outside of the transducer. This multilayer-beam addition is proposed to provide a better means of modeling and predicting macroscopic ionic polymer transducer performance with encapsulation. Another goal of this work is to investigate transducer response and model prediction ability extending to a frequency range approaching 1kHz.

The contributions of this work include:

- The development of a multi-layered-beam model to model the effects of the addition of an outer passive layer on ionic polymer transducer performance. This outer layer could be an encapsulation layer or possibly the transducer electrodes at lower transducer thickness.
- The Golla-Hughes-McTavish (GHM) method is applied to the characterization of the viscoelastic properties of NafionTM and results are presented.
- The current ionic polymer test fixture is refined to address data quality issues and allow a higher frequency range of transducer response exploration.
- The valid frequency range of the model created is explored and phenomena observed gives further insight into the fundamental characteristics of ionic polymer transducers and how subsequent models may be improved to better model higher frequency macroscopic transducer response.

1.5 Thesis Overview

The structure of this work is as follows:

Chapter Two contains the modeling development of the circuit terms in Newbury (2002) rederived for a three-layered-beam model. These equivalent circuit terms are created for multilayer beams with both a lumped parameter method (similar to Newbury (2002)) as well as a distributed parameter method to model the mechanical dynamics of ionic polymer

transducers. Input-Output relationships for the multilayer beam model formulation of ionic polymer transducers are compared to the original expressions derived in Newbury (2002). The incorporation of viscoelastic damping to the model using the Golla-Hughes-McTavish (GHM) method is introduced and discussed. The experimental testing setup used in this work is outlined as well as the model terms adapted to the new fixture geometry.

Chapter Three contains the viscoelastic parameter identification approach and results. The needed GHM parameters of NafionTM are found and the error minimization method used to find them is discussed. The results of the characterization of KaptonTM, which is used as the passive layer for model validation in Chapter four is also presented.

Chapter Four contains the evaluation of the model created in Chapter Two. Transducer measured response is compared to the simulated model response before and after encapsulation for two frequency ranges, low and high. The lower frequency range extends from dc levels to capture the first resonance of the transducers (\sim 1-20Hz for unencapsulated and 1-200 Hz for KaptonTM encapsulated). This is similar to the range used in Newbury (2002) for the unencapsulated transducers and was the original frequency range intended for this model formulation. The higher frequency range extends to 500Hz for unencapsulated and 1kHz for encapsulated transducers. This higher range is now possible due to test fixture refinements performed for this work that allow the observation of higher frequencies than was possible in Newbury (2002) and Newbury and Leo (2003a). Higher frequency response of the transducers is compared to model results and conclusions are made.

Chapter Five contains the summary of results and conclusions for the research presented in this work. Recommendations for future research are presented.

Appendix A contains the measured data vs the model predictions for the tests of the four transducers used in the evaluation of the model created in this work, (only partially presented in Chapter 4).

Chapter 2

Three-Layer-Beam Model

Development

The model developed in this work is an expansion of the electrical equivalent model of cantilevered beam ionic polymer transducers developed in Newbury (2002) and Newbury and Leo (2003a). The derivation will use the same modeling method in the lumped parameter section for comparative purposes. An electrical equivalent circuit with the same equivalent terms will be developed and evaluated. The main difference in this work is the utilization of a three-layer sandwich beam as opposed to the homogenous beam used in Newbury and Leo (2003a). This addition is an attempt to model the effects of a passive layer (either encapsulation material or possibly the electrodes at smaller NafionTM thickness) that was not explored in Newbury and Leo (2003b). The contribution of the electrodes to the mechanical characteristics of the transducer is neglected since the electrodes created by the current manufacturing process are typically less than $1\mu\text{m}$ in thickness (Bennett, 2002) and do not have much effect, this will be justified experimentally in the results chapter. The outer layers of passive material are expected to add passive stiffness resulting in the reduction of the free deflection of the beam. The system transfer functions are also rederived for the change in the test fixture setup, as well as expanded to additional beam modes to attempt to extend the useful frequency range of the model. The first section rederives the Newbury and Leo (2003a) model terms that change with layered beam theory using the same lumped parameter modeling approach, the second section uses a distributed parameter beam model to generate the terms in the circuit model, as well as extend the frequency range of the

model with additional modes of the beam.

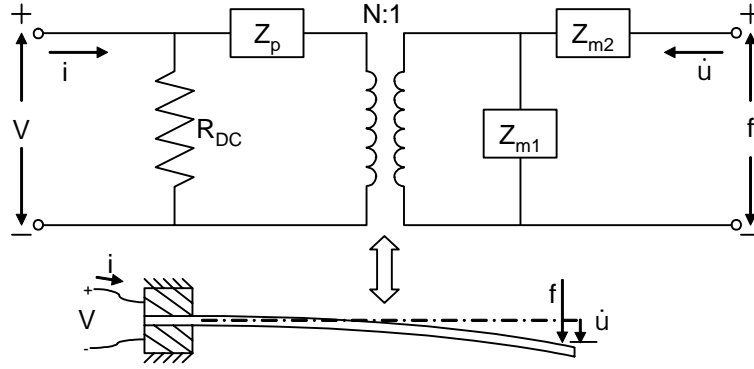


Figure 2.1: Electrical equivalent circuit model (Newbury and Leo, 2003a)

To begin the model revision, a three-layer sandwich beam is proposed. The outer layers are passive and the inner active layer is the NafionTM transducer.

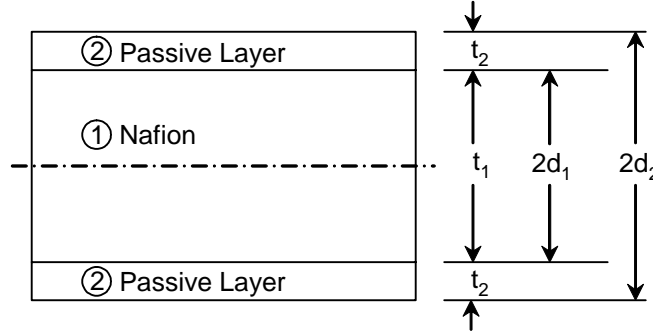


Figure 2.2: Cross section of 3 layer beam model

2.1 Lumped Parameter System Model

2.1.1 Mechanical Terms

To compare the differences between the proposed model and the Newbury-Leo model, a similar modeling approach with the same boundary conditions is taken. The static shape and first mode approximation terms (Z_{m1} and Z_{m2}) are rederived using a layered beam. Figure 2.3 illustrates the system modeled and its dimensions for reference.

The static deflection shape and associated stiffness term Z_{m1} derivation begins by realizing the moment M applied to a layered beam is related to the curvature ($1/\rho$) of the

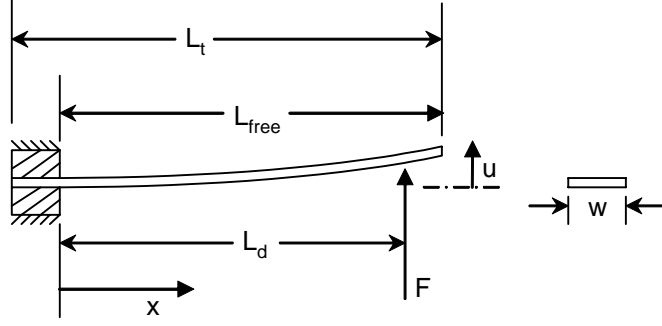


Figure 2.3: System used for model derivation

beam by the equation (Gere and Timoshenko, 1997)

$$\frac{1}{\rho} = \frac{d^2 u}{dx^2} = \frac{M}{E_1 I_1 + E_2 I_2}, \quad (2.1)$$

where I is the moment of inertia for the two separate sections and E is their modulus (static)

$$I_1 = \frac{w}{12} t_1^3, \quad (2.2)$$

and,

$$I_2 = \frac{w}{12} \left((t_1 + 2t_2)^3 - t_1^3 \right). \quad (2.3)$$

Substituting

$$M = f (L_d - x)$$

into Equation 2.1 and integrating with respect to x twice yields the equation

$$u(x) = \frac{f}{E_1 I_1 + E_2 I_2} \left(-\frac{x^3}{6} + \frac{L_d x^2}{2} + C_1 x + C_2 \right). \quad (2.4)$$

The parameters C_1 and C_2 are computed by enforcing the Boundary Conditions (BC's) for a cantilever beam, $u'(0) = 0$ and $u(0) = 0$. The first BC yields $C_1 = 0$, the second yields $C_2 = 0$. Substituting in C_1 and C_2 as well as the area moments of the section as a function of the section dimensions gives the relationship between the motion at $u(L_d)$ and the force applied at L_d ,

$$u(L_d) = \frac{4fL_d^3}{w (t_1^3 E_1 + (6t_1^2 t_2 + 12t_1 t_2^2 + 8t_2^3) E_2)}. \quad (2.5)$$

To obtain Z_{m1} , Equation 2.5 is rearranged and transformed into the Laplace domain to take the form of mechanical impedance

$$Z_{m1} = \frac{f}{su} = \frac{1}{s} \frac{w (t_1^3 E_1 + (6t_1^2 t_2 + 12t_1 t_2^2 + 8t_2^3) E_2)}{4L_d^3} . \quad (2.6)$$

When comparing this result to that in Newbury and Leo (2003a), the immediate difference is the addition of the terms associated with E_2 which are because of the introduction of passive layers. For a sanity check, when t_2 is set to zero (effectively removing the passive layer), the equation reduces to the same as found in Newbury and Leo (2003a), as expected.

For the derivation of Z_{m2} the same approach will be taken again as in Newbury and Leo (2003a) with the addition of passive layers. To begin, recall the equation for the natural frequency of a cantilever beam (Blevins, 1995),

$$\omega_i = \frac{\lambda_i^2}{L_{free}^2} \sqrt{\frac{EI_{eq}}{m_{eq}}} , \quad (2.7)$$

where λ_i is the solution to the characteristic equation for each mode (only the first will be considered here), L_{free} is the free length of the beam, and EI_{eq} is now the equivalent composite stiffness defined as (Blevins (1995))

$$EI_{eq} = \frac{2w}{3} \sum_{k=0,1,2} E_k (d_{k+1}^3 - d_k^3)$$

$$EI_{eq} = \frac{2w}{3} \left[E_1 \left(\left(\frac{t_1}{2} \right)^3 - 0 \right) + E_2 \left(\left(\frac{t_1}{2} + t_2 \right)^3 - \left(\frac{t_1}{2} \right)^3 \right) \right]$$

$$EI_{eq} = \frac{w}{12} (t_1^3 E_1 + (6t_1^2 t_2 + 12t_1 t_2^2 + 8t_2^3) E_2) . \quad (2.8)$$

The term m_{eq} is the equivalent mass per unit length defined as,

$$m_{eq} = 2w \sum_{k=0,1,2} \rho_k (d_{k+1} - d_k)$$

$$m_{eq} = 2w \left(\rho_1 \left(\frac{t_1}{2} \right) + \rho_2 \left(\left(\frac{t_1}{2} + t_2 \right) - \frac{t_1}{2} \right) \right)$$

$$m_{eq} = w (t_1 \rho_1 + 2t_2 \rho_2) . \quad (2.9)$$

Also utilizing the well known relationship,

$$\omega_i^2 = \frac{k}{m} \quad (2.10)$$

where k and m are the equivalent stiffness and mass of the lumped mass equivalent system, along with equations 2.7 and 2.5 allows the determination of the equivalent mass of the lumped polymer beam system for the first mode. Solving Equation 2.5 for $\frac{f}{u}$ and substituting it in for k into Equation 2.10 along with Equation 2.7 for ω_i into Equation 2.10 yields the equation for the equivalent mass of the beam.

$$m = \frac{3(t_1\rho_1 + 2t_2\rho_2)wL_{free}^4}{\lambda^4 L_d^3} \quad (2.11)$$

Converting the above equation into Z_{m2} utilizes Newton's Second Law in the (Laplace domain) $f = s^2mu$. Substituting in Equation 2.11 and solving for force over velocity (f/su) yields,

$$Z_{m2} = s \frac{3(t_1\rho_1 + 2t_2\rho_2)wL_{free}^4}{\lambda^4 L_d^3} . \quad (2.12)$$

Again this result can be compared with Newbury Leo and the passive layer effects are apparent as an increase to the mass of the transducer. As was for Z_{m1} , a sanity check is to set $t_2 = 0$ and observe that Equation 2.12 reduces to the same found for Z_{m2} in Newbury-Leo, as expected.

2.1.2 Electrical Terms

The rederivation of the electrical terms in the layered beam model are required for those which are affected by the mechanical properties of the beam, specifically, the transformer turns ratio N , which will be rederived next. Following the same method as in Newbury and Leo (2003a), for small deflections the stress at the boundary between the NafionTM (2.13) and the passive layers (2.14) are as follows (Gere and Timoshenko, 1997).

$$\sigma_{x1} = \frac{MyE_1}{E_1I_1 + E_2I_2} \quad (2.13)$$

$$\sigma_{x2} = \frac{MyE_2}{E_1I_1 + E_2I_2} \quad (2.14)$$

Where y is the distance from the neutral axis of the cross section and corresponds to half the total thickness of the NafionTM .

To arrive at the expression for the coupling term N in Figure 2.1, we first begin with the expression for the stress at the outer layer of the NafionTM layer (Equation 2.13). By substituting in $y = t_1/2$ and $M = f(L_d - x)$ Equation 2.13 simplifies to

$$\sigma_{x1} = \frac{f(L_d - x)t_1E_1}{2(E_1I_1 + E_2I_2)}. \quad (2.15)$$

Recalling that in piezoelectric materials the electrical displacement Q is related to both the stress and electrical field in the material.

$$D = d\sigma + \epsilon^\sigma E \quad (2.16)$$

where d is the coupling coefficient, and ϵ^σ is the electric permittivity of the material. The coupling coefficient used here to model the electromechanical coupling seen in the polymer. It is important to stress that the fundamental coupling mechanism observed in the polymers is not believed to be the same as in piezoelectric, the d coefficient simply models the linear coupling between the two domains. For all cases in this model, the electrodes are considered perfectly conductive (no potential of current loss) and the NafionTM is the only layer that contributes anything to the electrical properties of the polymer transducer.

Substituting Equation 2.15 into Equation 2.16 and realizing that the electric field is the applied voltage divided by the thickness of the NafionTM layer yields an expression for the electrical displacement per unit area. The total electrical displacement Q for the particular transducer geometry is found by integrating over the length and width of the transducer as shown below.

$$Q = \int_0^{L_t} \int_{-w/2}^{w/2} \left(d \frac{f(L_d - x)t_1E_1}{2(E_1I_1 + E_2I_2)} + \frac{\eta^\sigma v}{t_1} \right) dz dx \quad (2.17)$$

evaluating the integrals and substituting in the geometry terms results in the expression for the electrical displacement of the polymer transducer.

$$Q = \frac{3L_d^2t_1dE_1}{(6t_1^2t_2 + 12t_1t_2^2 + 8t_2^3)E_1 + E_2t_1^3} f + \frac{\eta^\sigma wL_t}{t_1} v \quad (2.18)$$

where η^σ is a frequency dependent electric permittivity.

Now to find the turns ratio of the transformer in the electrical equivalent system, set $Q = 0$ in Equation 2.18 and solve for v/f which results in the following equation.

$$N = \frac{v}{f} = \frac{t_1}{\eta^\sigma wL_t} \frac{3dL_d^2t_1E_1}{((6t_1^2t_2 + 12t_1t_2^2 + 8t_2^3)E_1 + E_2t_1^3)} \quad (2.19)$$

The remainder of the electrical terms needed for the model will remain the same as in Newbury and Leo (2003a) because the passive layer introduction has no influence on their definition. Included here for reference,

$$R_{DC} = \frac{\rho_{DC} t_1}{L_t w} . \quad (2.20)$$

R_{DC} is the dc resistance of the transducer, composed of ρ_{dc} , the resistivity, t_1 , the thickness, w , the width, and L_t , the total length of the polymer.

$$Z_p = \frac{t_1}{s L_t w} \frac{1}{\sum_{i=1}^n \frac{\epsilon_i}{1 + s \epsilon_i \rho_i}} \quad (2.21)$$

Z_p , the electrical impedance, is composed of the transducer dimensions and a summation of permittivities and resistances to approximate the electrical behavior of the transducer. See Newbury (2002) for a complete explanation and justification.

$$\eta^\sigma(s) = \sum_{i=1}^n \frac{\epsilon_i}{1 + s \epsilon_i \rho_i} \quad (2.22)$$

η^σ is the frequency dependant electrical permittivity approximation of the transducer where the σ superscript indicates zero stress condition.

2.1.3 Lumped Parameter Model Comparison

Now that equivalent lumped parameter terms are developed for the layered beam model, it can now be compared directly with that developed in Newbury and Leo (2003a). Specifically since no terms were added or removed to the equivalent circuit, (which would change the mesh analysis) the input/output relationships can be assembled and compared. The assembled and simplified circuit analysis of the system in Figure 2.1 results in the following matrix of equations, see Newbury (2002) for detailed circuit analysis.

$$\begin{Bmatrix} v \\ f \end{Bmatrix} = \begin{bmatrix} \frac{R_{dc}(N^2 Z_{m1} + Z_p)}{R_{dc} + N^2 Z_{m1} + Z_p} & \frac{N R_{dc} Z_{m1}}{R_{dc} + N^2 Z_{m1} + Z_p} \\ \frac{N R_{dc} Z_{m1}}{R_{dc} + N^2 Z_{m1} + Z_p} & \frac{(Z_{m1} + Z_{m2})(R_{dc} + Z_p) + N^2 Z_{m1} Z_{m2}}{R_{dc} + N^2 Z_{m1} + Z_p} \end{bmatrix} \begin{Bmatrix} i \\ \dot{i} \end{Bmatrix} \quad (2.23)$$

For convenience, the convention adopted in Newbury and Leo (2003a) will be followed here as well, the variable set to zero will be used as the superscript. For example,

$$\left(\frac{f}{v}\right)^{\dot{i}}$$

represents force output with a voltage input, with the velocity held at zero, commonly referred to as blocked force. It has been shown experimentally that the assumption of reflected mechanical impedance being negligible compared to the electrical impedance in an ionic polymer transducer is valid (Newbury, 2002). This is a valuable simplification and takes two forms depending on the mechanical boundary condition. For the blocked case,

$$N^2 Z_{m1} \ll Z_p \quad (2.24)$$

and for the free case,

$$N^2 \frac{Z_{m1} Z_{m2}}{Z_{m1} + Z_{m2}} \ll Z_p \quad (2.25)$$

The following sections will use this assumption to simplify the results of Equation 2.23 for various input-output relationships.

Actuator Equations

Setting $\dot{u} = 0$ in Equation 2.23 corresponds to a blocked mechanical boundary condition and yields the equation for blocked force,

$$\left(\frac{f}{v}\right)\dot{u} = \frac{N Z_{m1}}{Z_p} = \frac{3dt_1 w E_1}{4L_d} \quad (2.26)$$

when compared to the result in Newbury and Leo (2003a), denoted by subscript (NL)

$$\left(\frac{f}{v}\right)\dot{u}_{(NL)} = \frac{3dtwY^E}{4L_d} \quad (2.27)$$

the equations are remarkably similar. This result is not surprising since the passive layers would have no effect until motion occurs. The biggest difference is that now the stiffness of the transducer is only determined by the modulus of the NafionTM layer, as opposed to the bulk modulus measured and used in Newbury and Leo (2003b).

Setting f in Equation 2.23 to zero and performing an s domain integration results in the expression for free deflection with a voltage input of a cantilever transducer.

$$\left(\frac{u}{v}\right)^f = \frac{-N Z_{m1}}{s Z_p (Z_{m1} + Z_{m2})} = \frac{-3dt_1 E_1 L_d^2}{\frac{12(\rho_1 t_1 + 2\rho_2 t_2) L_f^4}{\lambda^4} s^2 + t_1^3 E_1 + (6t_1^2 t_2 + 12t_1 t_2^2 + 8t_2^3) E_2} \quad (2.28)$$

when again compared with Newbury and Leo (2003a),

$$\left(\frac{u}{v}\right)^f_{(NL)} = \frac{-3dL_d^2}{\frac{12\rho_m L_f^4}{\Gamma^4 Y^E} s^2 + t^2} \quad (2.29)$$

Comparing these two results, if t_2 is set to zero in Equation 2.28, it reduces to the result in Newbury and Leo (2003a), with the only difference that now the density and thickness of the NafionTM are used instead of the composite values.

Sensor Equations

Ionic polymer transducers are especially useful as sensors due to their high sensitivity and low stiffness. Equation 2.23 can be solved for various sensor equations where either short-circuit charge or open circuit voltage can be measured. If current measurement is desired, an s domain conversion can be performed to obtain the desired relationship. Setting v equal to zero in Equation 2.23 will yield the sensor equation of current over velocity,

$$\left(\frac{i}{\dot{u}}\right)^v = \frac{-NZ_{m1}}{Z_p} = \frac{-3dt_1wE_1}{4L_d} \quad (2.30)$$

$$\left(\frac{i}{\dot{u}}\right)^v_{(NL)} = \frac{-3dtwY^E}{4L_d}. \quad (2.31)$$

This equation is the negative reciprocal of blocked force and the same observations apply. Performing a Laplace domain integration (dividing by s on the numerator and denominator of Equation 2.30) will give the sensor relationship between charge and displacement which is the same as current over velocity.

Another useful sensor equation is open circuit voltage from a displacement input. This expression is found by setting $i = 0$ on Equation 2.23 and solving for voltage over velocity. This expression can then be multiplied by s (effectively integrating velocity in the denominator) to yield voltage over displacement.

$$\left(\frac{v}{u}\right)^i = \frac{sNR_{dc}Z_{m1}}{R_{dc} + Z_p} = \frac{s3dt_1^2E_1\rho_{dc}}{4L_dL_t(1 + s\eta\rho_{dc})} \quad (2.32)$$

when compared with the Newbury and Leo (2003a) result,

$$\left(\frac{v}{u}\right)^i_{(NL)} = \frac{s3dt^2Y\rho_{dc}}{4L_dL_t(1 + s\eta\rho_{dc})} \quad (2.33)$$

the main difference is that now the thickness and modulus used is the thickness of the NafionTM layer only instead of the total transducer thickness.

The input/output equations derived with the passive layers allow the modeling of a passive layer of arbitrary thickness, stiffness and density. The resulting equations reduce to those of Newbury and Leo (2003a) when the passive layer thickness is set to zero. These relationships will be explored experimentally in the results chapter.

2.2 Distributed Parameter System Modeling

This section will develop a model based on distributed parameter system modeling. Using a distributed parameter approach should give a better approximation of beam behavior at frequencies above the first resonance when compared to lumped parameter approximations. Modal expansion will be used to increase the useful frequency range of the ionic polymer model.

2.2.1 Cantilever Boundary Conditions

Taking a distributed parameter modeling approach to the generation of the mechanical model parameters in Newbury (2002) reduces the number of terms needed to approximate the system to higher modes since the second term can contain the dynamics of numerous modes. To begin the development, the partial differential equation for the motion of a beam in transverse free vibration is (Inman, 2001),

$$\rho A(x) \frac{\partial^2 u(x, t)}{\partial t^2} + \frac{\partial^2}{\partial x^2} \left(EI(x) \frac{\partial^2 u(x, t)}{\partial t^2} \right) = 0, \quad (2.34)$$

where ρ is the density of the beam, $A(x)$ is the cross sectional area, E is the modulus of the beam, and $I(x)$ is the section moment of inertia. Assuming a solution form of Equation 2.34 of (Inman, 2001),

$$u(x, t) = \sum_{i=1}^n y_i(x) q_i(t), \quad (2.35)$$

where $y_i(x)$ is the mode shape of the i^{th} mode and $q_i(t)$ is the temporal response of the i^{th} mode.

Assuming constant cross sectional area and moment inertia, the mode shapes for a clamped-free (cantilevered) beam are (Blevins, 1995)

$$y_i\left(\frac{x}{L}\right) = \cosh \frac{\lambda_i x}{L} - \cos \frac{\lambda_i x}{L} - \sigma_i \left(\sinh \frac{\lambda_i x}{L} - \sin \frac{\lambda_i x}{L} \right), \quad (2.36)$$

where λ_i is a dimensionless parameter associated with the boundary conditions, and σ_i is a simplified value from the characteristic equation, not to be confused with stress also used in this work.

For modeling the free deflection of ionic polymer transducers, it should be adapted to the loading case of a distributed moment. The approach taken here is similar to the

formulation of a piezo-electric bimorph in a cantilevered condition. The governing partial differential equation follows from Hamilton's principle as (Fanson and Caughey, 1990),

$$m(x) \frac{\partial^2 u}{\partial t^2} + \frac{\partial^2}{\partial x^2} \left(E(x) I(x) \frac{\partial^2 u}{\partial x^2} \right) = \frac{\partial^2 M(x, t)}{\partial x^2} \quad (2.37)$$

Substitution of the multi-layer theory terms into the above equation, multiplying by the mode shape $y_i(x)$, and enforcing orthogonality of mode shapes is performed. Then transforming the resulting equation into the Laplace domain yields,

$$\left(m_{eq} \frac{L_d}{2} s^2 + \frac{EI_{eq}}{2L_d^3} \lambda_i^4 \right) q_i(s) = M_o y'_i(L_d) M(s), \quad (2.38)$$

where M_o is the arbitrary magnitude of the applied moment.

Substituting Equation 2.35 and solving for u/M the general solution of Equation 2.38 takes the form,

$$\frac{u(s)}{M(s)} = \sum_{i=1}^n \frac{M_o y'_i(L_d) y_i(L_d)}{m_i s^2 + k_i} \quad (2.39)$$

where $m_i = m_{eq} \frac{L_d}{2}$ and $k_i = \frac{EI_{eq}}{2L_d^3} \lambda_i^4$. Values for λ_i can be found in Blevins (1995).

Equation 2.39 can be simplified to only include the first mode of vibration and takes the form,

$$\frac{u_1(s)}{M(s)} = \frac{M_o y'_1(L_d) y_1(L_d)}{m_1 s^2 + k_1} \quad (2.40)$$

To put the equation into the form of mechanical impedance M/su , Equation 2.40 can be inverted and divided by s ,

$$Z_m = \frac{M}{su_1} = \frac{m_1 s^2 + k_1}{s \phi_1} \quad (2.41)$$

where $\phi_1 = M_o y'_1(L_d) y_1(L_d)$. Substituting in values and simplifying yields,

$$Z_m = \frac{m_{eq} L_d}{2 \phi_1} s + \frac{EI_{eq} \lambda_i^4 L_d}{2 s L^4 \phi_1} \quad (2.42)$$

This equation is really a summation of Z_{m1} and Z_{m2} , if only the static term were needed, the lumped approximation Z_{m1} (which is a static representation of a cantilever beam) could be used. For the simulation in this work, the term Z_m is used to replace the summation of Z_{m1} and Z_{m2} . Note that if additional modes were desired to extend the frequency range of the model, Equation 2.39 could simply be expanded using more modes. This form of the mechanical impedance uses only one term to model the dynamics and is adjusted according to the number of modes of interest for comparison. This is in contrast to the approach taken in Newbury (2002) where additional modes meant additional terms in the circuit.

2.2.2 Transfer Function Analysis and Modeling of Test Fixture

This section adapts the distributed parameter model derived in the previous section to the current test fixture geometry of a sliding-pinned beam. The reasons for this change are discussed in the test setup section. A proposal for a GHM viscoelastic damping model of the beam is then presented. The post processing required to remove the force transducer dynamics from the data is also discussed.

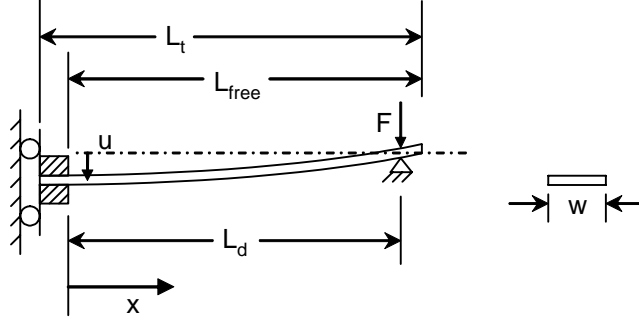


Figure 2.4: Transducer dimensions used in sliding-pin model adaptation.

Sliding - Pinned Beam Transfer Function

The mechanical quantities measured in the modulus and sensing test fixture are the input, displacement at $x = 0$ and the output, force at $x = L_d$. Experimentally these quantities are represented by the transfer function $\frac{f_r(L_d, s)}{u(0, s)}$. To derive this relationship and correctly simulate the model results first the transfer function between $f(0, s)$ and $u(0, s)$ is defined for each mode in the Laplace domain,

$$\frac{f(0, s)}{u(0, s)} = \frac{1}{\sum_{i=1}^n \frac{y_i(0)^2}{m_i s^2 + k_i}}, \quad (2.43)$$

where y_i is the sliding-pinned mode shape. The equation for the mode shape of a sliding-pinned BC beam is (Blevins, 1995),

$$y_i\left(\frac{x}{L}\right) = \cos\left(\frac{(2i-1)\pi x}{2L}\right). \quad (2.44)$$

The next key term to develop for the desired transfer function relationship of the fixture is $\frac{f_r(x, t)}{f(0, t)}$. To begin the development, the reaction force in the pin at $x = L_d$ is equal to the shear force in the beam at $x = L_d$ (Inman, 2001),

$$f_r(x, t) = EI_{eq} \frac{\partial^3}{\partial x^3} u(x, t), \quad (2.45)$$

where $u(x, t)$ is defined again by Equation 2.35. Substituting Equation 2.35 into Equation 2.45 and transforming into the Laplace domain yields,

$$f_r(x, s) = EI_{eq} \sum_{i=1}^n \frac{\partial^3}{\partial x^3} y_i(x) q_i(s) . \quad (2.46)$$

The above equation can be divided on both sides by $f_i(0, s)$, then substituting in $\frac{y_i}{m_i s^2 + k_i}$ in for $\frac{q_i(s)}{f_i(0, s)}$ yields the equation relating the applied force at $x = 0$ to the reaction force at another point along the length of the beam,

$$\frac{f_r(x, s)}{f(0, s)} = EI_{eq} \sum_{i=1}^n \frac{y_i'''(x) y_i(0)}{m_i s^2 + k_i} . \quad (2.47)$$

Now multiplying equations 2.47 and 2.43 together, expanding the sum to the desired number of modes, and evaluating $x = L_d$ will yield the desired transfer function between the force in the pin at $x = L_d$ and the motion input to the beam at $x = 0$ (Equation 2.48).

$$\frac{f_r(L_d, s)}{u(0, s)} = \left(EI_{eq} \sum_{i=1}^n \frac{y_i'''(L_d) y_i(0)}{m_i s^2 + k_i} \right) \frac{1}{\sum_{i=1}^n \frac{y_i(0)^2}{m_i s^2 + k_i}} \quad (2.48)$$

It is important to notice that this is essentially an equation for the stiffness of the beam. The input to the system will be the motion at $u(0)$, not a force at the pin. A force at the pin will produce no motion at the base of the beam.

To arrive at the first mode impedance approximation to compare to previous Z_m formulations, only the first mode will be considered now,

$$\frac{f_r(L_d, s)}{u_1(0, s)} = EI_{eq} \frac{y_1'''(L_d) y_1(0)}{m_1 s^2 + k_1} \cdot \frac{m_1 s^2 + k_1}{y_1(0)^2} \Rightarrow EI_{eq} \frac{y_1'''(L_d)}{y_1(0)} \left(\frac{\pi}{2L} \right)^3 . \quad (2.49)$$

An interesting characteristic of this system is evident in the equation and can be observed even with higher modal expansion simulation, the first mode is canceled out and frequency response is flat across the first natural frequency.

To transform Equation 2.49 into mechanical impedance, the equation is divided by s to change displacement to velocity,

$$Z_{m-sp} = \frac{f_r(s)}{s u_1(s)} = \frac{1}{s} EI_{eq} \frac{y_1'''(L_d)}{y_1(0)} \left(\frac{\pi}{2L} \right)^3 \quad (2.50)$$

Basically this result indicates that in order to see any dynamics of the system in a sliding-pinned BC, the frequency and model must extend to at least the second mode. This fixture also has a more subtle effect of increasing the ‘low’ frequency range for observing ‘static’ stiffness and other parameters by giving a flat response through the first mode of the beam.

2.2.3 Incorporation of Viscoelastic Damping

Since ionic polymers exhibit damped response to stimuli, a method of damping must be introduced to the model to increase its accuracy, especially near resonances of the system. Polymers generally exhibit viscoelastic damping, which means the damping and the stiffness of the material is frequency dependent (Macosko, 1993). Stiffness generally increases with frequency to a certain level and damping has a frequency range of influence. Some research has been conducted investigating the viscoelastic properties of NafionTM, and hydrated NafionTM specifically (Uan-Zo-li (2001)). The majority of the experiments performed by Uan-Zo-li were done by varying the temperature of the material and keeping excitation frequency constant as opposed to varying the frequency of excitation with constant temperature, which was the nature of the experiments and applications in this work. Consistent results were difficult to obtain in the hydrated state since static modulus has such a strong dependence on hydration level (Dupont, 2000b). Dupont has measured the modulus of NafionTM per ASTM D 882 and has found it to range from 64 MPa when saturated at 100°C to 249 MPa at 50% RH and 23°C. These changes in modulus were also seen in experimental work done for this project.

To incorporate damping into the model, a viscoelastic material model is used for the NafionTM layer and results in a complex modulus. While many models exist for characterizing viscoelastic material properties, the simplest for possible application to NafionTM is that of a standard linear solid (Macosko (1993)), see Figure 2.5(a). The left branch accounts for a static storage modulus or stiffness and the right branch attempts to model the change of stiffness and loss factor of the modulus with frequency. Another possible model and the one chosen for this work is similar to that presented by McTavish and Hughes (1993), called the GHM Method, (see Figure 2.5(b)). The GHM Method utilizes a ‘mini-oscillator’ in the material model to account for the stress levels encountered above static conditions. The spring on the left accounts for the static storage modulus or stiffness, and as the excitation frequency changes, the oscillator has a changing effect on the overall stiffness and damping of the material. The GHM Method is a good model for structural dynamics because it contains second and first order terms to preserve the symmetry of the mass, damping, and stiffness matrices. This is also the material model used by Newbury Leo and since only one ‘mini-oscillator’ term is used for material characterization in both models, the curve fit

parameters can be compared. The curve fitting and value comparisons will be discussed in detail in Chapter 3.

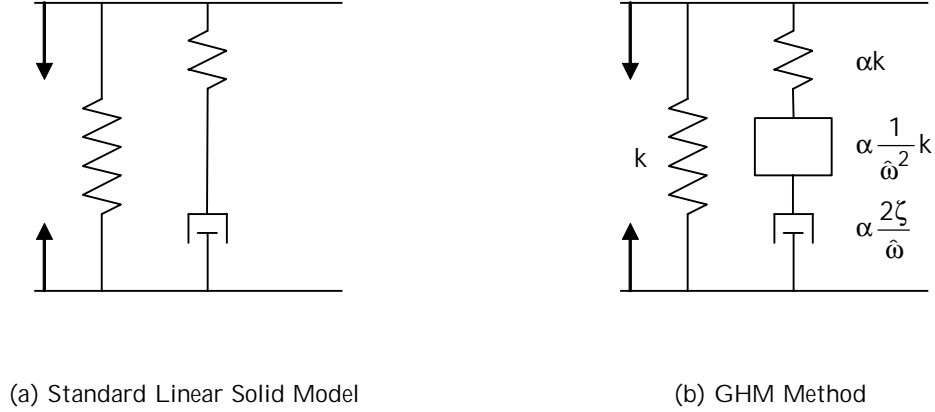


Figure 2.5: Models for linear viscoelasticity

To incorporate viscoelasticity into the model, the NafionTM modulus E_1 is changed to include the GHM terms. The modulus expression for the combined branches of Figure 2.5(b) (in the Laplace domain) adapted to the polymer model is,

$$E_1 = E_{static} \left(1 + \alpha \frac{s^2 + 2\zeta\hat{\omega}s}{s^2 + 2\zeta\hat{\omega}s + \hat{\omega}^2} \right) \quad (2.51)$$

where E_{static} is the static modulus of the NafionTM, and α , ζ , and $\hat{\omega}$ are ‘GHM’ parameters.

2.3 Experimental Testing Setup

This section will describe the testing equipment and setup used to acquire the data reported in this work. The mechanical modulus testing setup used in the next chapter consisted of an electromagnetic shaker (Bruel and Kjaer Mini Shaker Type 4810 ± 3 mm max. stroke) for the displacement input to the system. A linear potentiometer was used for measurement of the shaker motion, its signal was amplified and conditioned to give a sensitivity of 2.71E-3 mm/mV. Force was measured at a location on the beam with a GSO-10 (10 gram) load cell connected to a TMO-1 signal conditioning circuit (both from Transducer Techniques) which gave a force measurement resolution of 12.3 μ N/mV. All schematics of electrical circuits used for signal measurement/conditioning can be found in Newbury (2002).

The modulus tests used a clamped-pinned beam mechanical boundary condition with

the motion input applied to the clamped end and the force measured at the pin, see Figure 2.6(a) for diagram. There are a couple reasons for this fixture change, one reason is the accelerometer effect observed in Newbury (2002) when the load cell was mounted to the end of the shaker. This phenomena is avoided by mounting the load cell in a stationary position and putting the polymer clamp on the end of the shaker. Due to the sensitivity of the load cell, it was further isolated by placing the load cell and the shaker on separate adjacent tables and both of the devices were supported on Sorbothane rubber to reduce vibration transmission between the shaker and the load cell. This was found to be necessary by examining the transfer function between the shaker and load cell without a polymer in the clamp, ideally there would be no coherence between the signals. The steps taken here are a great improvement over previous setups, but there is still some feed through especially at the load cell resonant frequency where any excitation results in large signal amplification. The second reason for separating the load cell and shaker is reduced mass on the end of the shaker and increased shaker frequency performance (a smaller shaker is utilized currently than the long throw shaker used in Newbury (2002)).

The polymer was held by a clamp machined from DelrinTM. Gold was bonded to the inner clamp surfaces to allow the signals to be sent to and measured from the polymer, although for the mechanical modulus tests this connection was not used. The signal sent to the shaker was from the output of a Tektronics 2300 Fourier Analyzer and was fed through a HP power amplifier before entering the shaker. The displacement signal from the potentiometer was sent through a signal conditioning circuit to amplify and remove the DC bias before entering the Tektronics. The force signal was sent directly from the TMO-1 to the Tektronics.

The other tests used to characterize the polymer transducers consisted of imposing a mechanical deformation of the polymer with the shaker in the same configuration as above and measuring a charge signal from the polymer (sensing), see Figure 2.6(d), or keeping the polymer base stationary and sending a voltage signal to the polymer and measuring force (blocked force since the load cell does not move under these forces), see Figure 2.6(b). For free deflection testing the load cell was removed from the fixture and a laser vibrometer with variable resolution (0.5 to 1280 $\mu\text{m}/\text{V}$) was used to measure the free deflection of the tip of the now cantilevered polymer, see Figure 2.6(c).

A picture of the general testing setup can be seen in Figure 2.7. The only changes to

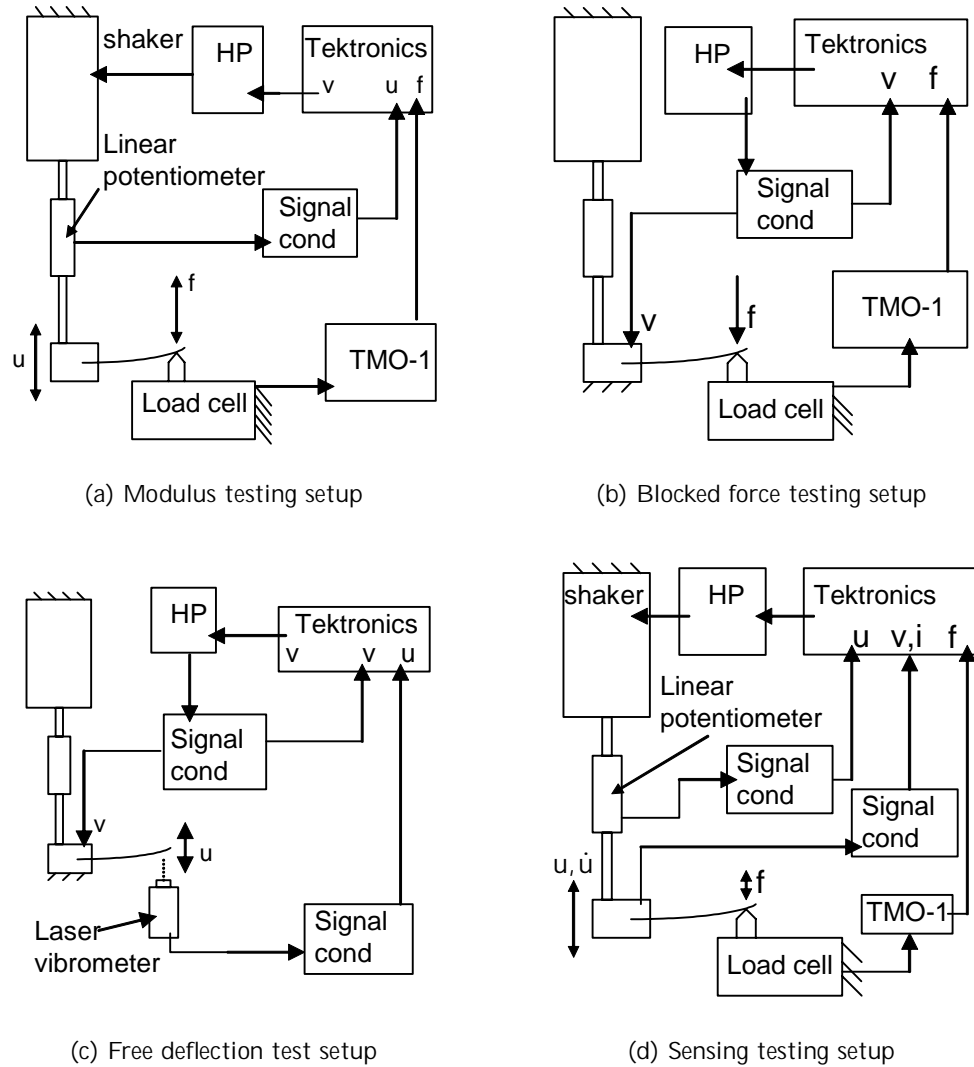


Figure 2.6: Diagrams of various test setups

this are when free deflection is measured, the load cell is moved away and a laser vibrometer is used to measure the deflection of the tip of the now cantilevered beam. Figure 2.8 is a close up of the load cell, polymer, clamp setup configuration used for all tests other than free deflection.

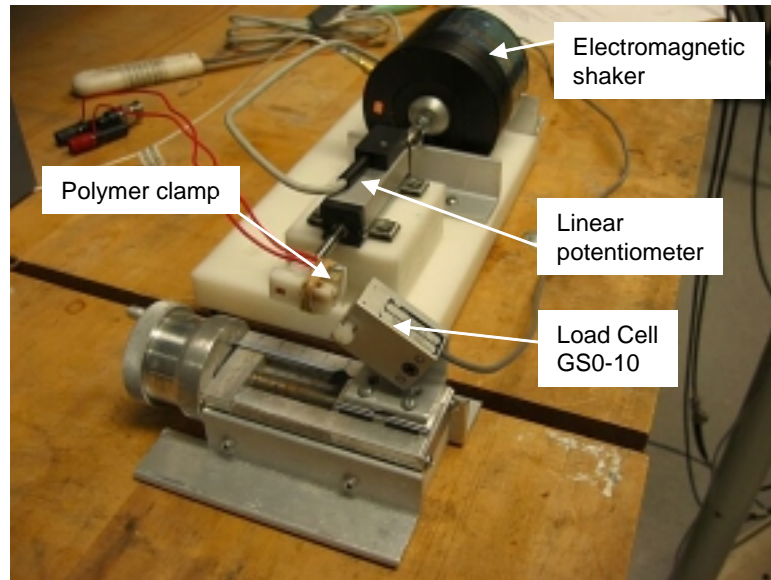


Figure 2.7: Picture of testing setup

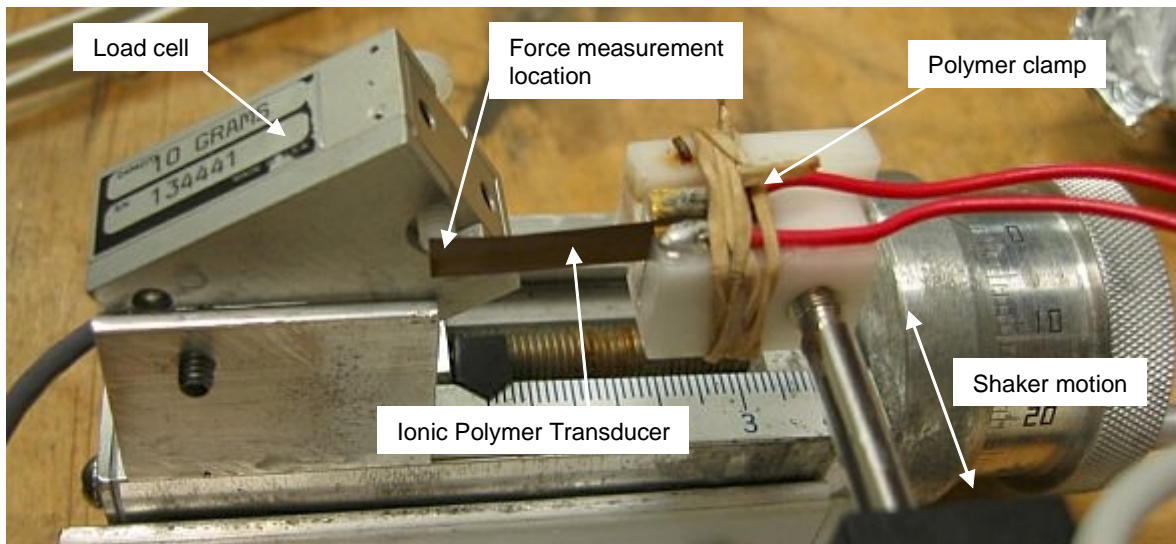


Figure 2.8: Close up of polymer and load cell fixture

2.3.1 Post Processing of Data

The load cell and signal conditioning circuit have inherent higher frequency ($>100\text{Hz}$) dynamics that must be removed to improve accuracy of the results as the frequency range of the experiments are extended. The goal of post processing was to extend the useful testing range to 1kHz in order to have a larger frequency range to view the viscoelastic properties of the polymer. This range would also allow the investigation of smaller polymers that might have a much larger actuation bandwidth than the current typical size polymer beam, as well as the investigation of polymer behavior beyond typical useful actuation range (for example, in sensing).

There are two dynamic phenomena that must be removed, one is the high-Q mechanical resonance of the load cell itself, the other is the low pass filter utilized in the TMO-1 circuitry. Without removing these two effects, the data is corrupted beyond acceptable limits as low as 140 Hz . The load cell resonance occurring at $\sim 209\text{Hz}$ adds amplification near resonance and then attenuation after as well as an additional -180° of phase to the data after resonance. The TMO-1 was modified as per Transducer Techniques instruction to change the corner frequency of the filter from 220Hz to 2200Hz , the change removes the magnitude attenuation above the previous 220Hz corner frequency, but phase processing is still necessary to remove the filter effects even as low as 200Hz .

The post processing methodology was to measure the characteristics of the load cell-conditioning system and then approximate the system with a model in Matlab that could be simulated and that simulated frequency response used to remove the system characteristics from the measured data. This is opposed to normalizing the load cell data directly and removing it from the measured polymer response. By only removing a ‘smooth’ simulated system response, the remaining data still had information regarding other effects that could be noted. This is felt to be important when investigating other noise sources in the experiments such as fixture resonances that could change with time/setup and cause improper data correction actually making the signals false. The characteristics of the system were measured by attaching an accelerometer to the housing of the load cell and ringing the load cell chassis. The accelerometer response was flat from $\sim 30\text{Hz}$ to well above the frequency range of interest for polymer testing. The load cell signal conditioning circuit output and the amplified accelerometer output were fed into the Tektronics. The transfer function

between the two channels was then computed using the accelerometer as the reference in order to see the characteristics of the GSO-10/TMO-1 dynamics. The results of these tests as well as the model approximation developed next can be seen in Figure 2.9.

To begin the modeling, first the transfer function data was compensated by removing the dynamics of the filter which is an analog low-pass Butterworth filter with a corner frequency of 2200Hz (Techniques, 2000). This filter was simulated with the `butter` function in Matlab, and then its frequency response was simulated and divided out of the measured response. Next a 3rd order system model was fit to the data range from 50Hz to 1000Hz in Matlab using `invfreqs` to obtain the system associated with the load cell. This system was then combined with the filter system and the DC gain was normalized to 1 to not distort the magnitude of the corrected data. Now that a system is created for the GSO-10/TMO-1 combination, all data taken with the load cell can be compensated by simulating this system in Matlab over the desired frequency range and dividing out the simulated response from the measured data.

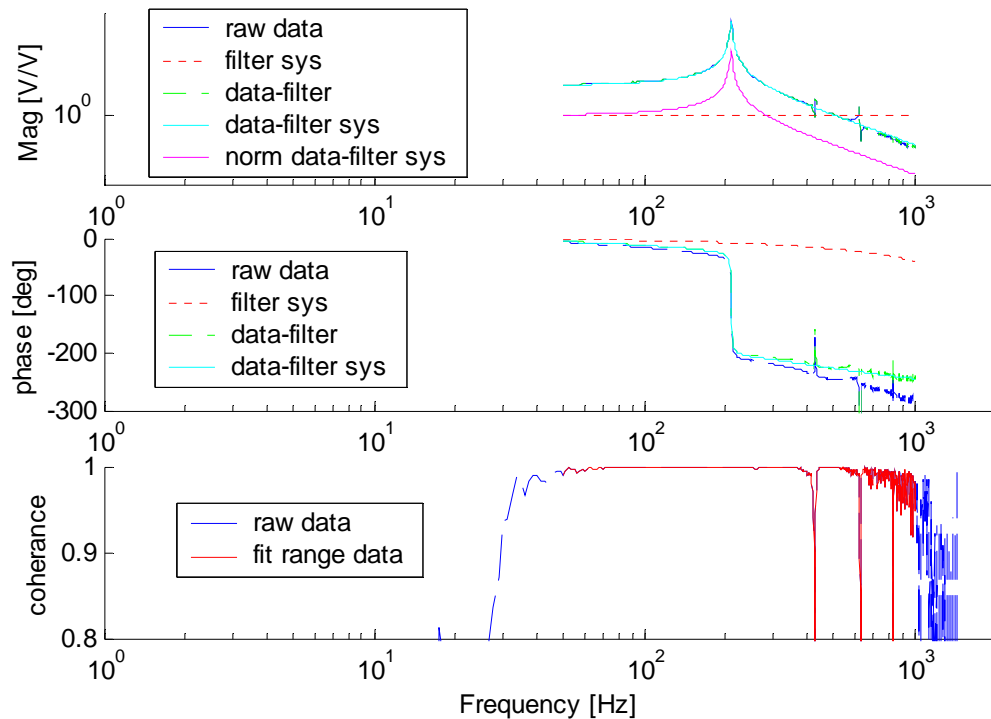


Figure 2.9: Load cell and signal conditioning circuit modeling

A typical modulus test data set is shown in Figure 2.10, the small discontinuity in

the processed data at the load cell resonance (209Hz) is most likely due to a small amount of water on the stinger of the load cell which adds mass and can shift the natural frequency slightly. This load cell resonance shift and resulting discontinuity is seen in some data sets where a small amount of water from the beam remains on the threads of the stinger used to measure the force from the beam. Effects are usually very local due to the high Q of the load cell resonance and the small amount of water typically trapped in the stinger threads.

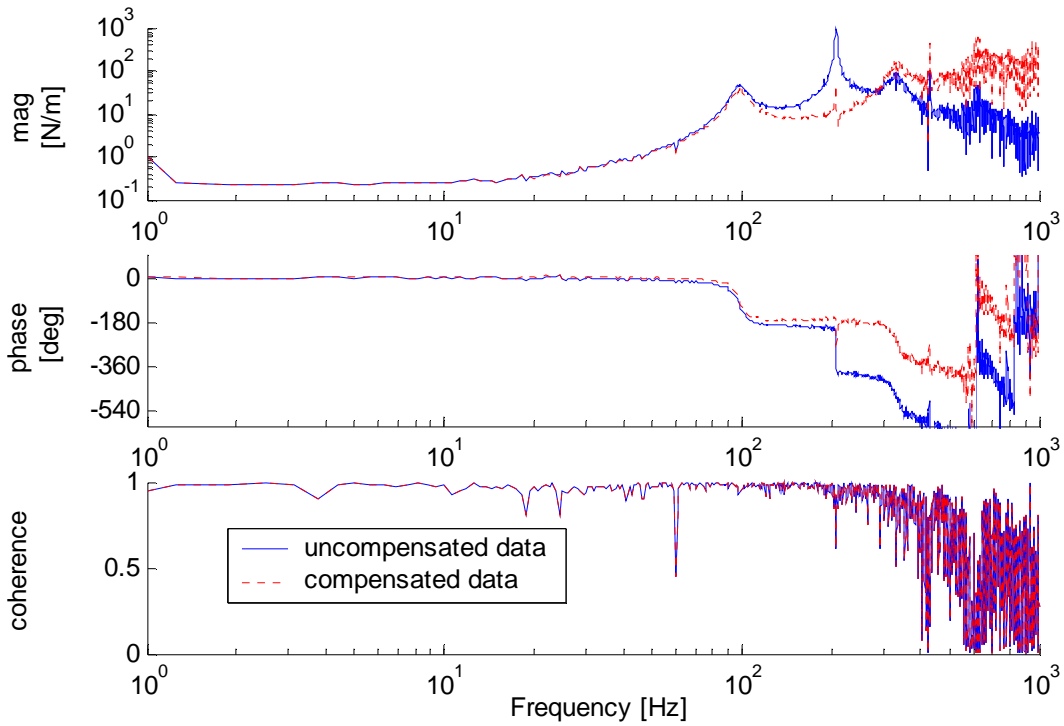


Figure 2.10: Typical stiffness (f/u) run processed, the blue line is the raw measured data, the red dotted line is the data processed to remove the load cell dynamics

Chapter 3

Viscoelastic Parameter Identification

This chapter will discuss the approach and results of the characterization of the viscoelastic material properties of NafionTM, specifically in the room temperature saturated state (unboiled, hydrated in Deionized (DI) H₂O at 23°C). Test setup and considerations will be discussed, the minimization approach will be outlined, and the Golla Hughes McTavish (GHM) parameter fit results will be presented and discussed. Characterization results of the KaptonTM polyimide film used as the encapsulation layer in Section 4.3.2 will also be presented and discussed.

3.1 Viscoelastic Parameters and Test Setup

When utilizing the GHM method, three parameters are introduced for each oscillator term used. This model will use only one oscillator term to model the frequency effects of the material. A single GHM term requires three parameters, $\hat{\alpha}$, $\hat{\zeta}$ and $\hat{\omega}$ introduced in the previous chapter. These parameters were found by minimizing the error between the measured frequency response and the simulated system response using the GHM parameters. This process will be discussed in the next section. Only one GHM term is used in this work due to the added burden of introducing additional terms, (mostly in the system simulation and minimization time) as well as because the single GHM term seems to fit the experimental response reasonably well over the frequency range used in this work (1-500Hz). Additional terms might give a better approximation if the frequency range is changed or extended,

essentially providing more curve fit parameters for the frequency response characterization.

The NafionTM 117 samples used for the viscoelastic characteristics were cut directly from the main sheet of NafionTM 117, roughened, placed in water at room temperature and allowed to sit overnight. The thickness was measured to be $200\mu m$, this is more than the $180\mu m$ thickness at room conditions due to the swelling induced by water uptake. The samples were never boiled in a solution (which would reduce the static modulus to 64 MPa, even after cooling), this results in a static modulus of the NafionTM of 114MPa (Dupont, 2000b). This 114 MPa static modulus was used for this work and is supported by the low frequency stiffness correlation between the experimental data and the simulated model response, because GHM viscoelasticity has very little effect on the dc modulus of a material.

The viscoelastic characterization tests consisted of taking a NafionTM beam and measuring the stiffness frequency response in the sliding-pinned configuration as described in the previous chapter (see Section 2.3). The beam was slightly preloaded against the load cell stinger to avoid separation of the beam from the load cell. Data coherence was strongly dependent on proper preload, too little and tapping occurred, too much and the angle of the beam misdirected the force in relation to the load cell measurement axis. Because of the strong dependence of the modulus of NafionTM on hydration state, tests were performed quickly. The sample was removed from water, placed in the fixture, excess water was quickly wiped off of the beam to remove extra mass that would change the resonant response of the sample, and the test was run. Using the Tektronics Fourier signal analyzer with a bandwidth setting of 500Hz and a window resolution of 4096 samples with 5 avgs was all that time would allow. Shortly after the end of the experiment the polymer would visually dry out, (curl and change opacity). The resonant peak also shifts with hydration, so if additional averages were taken, requiring more time, the last avgs would round out the resonant peaks due to the shift of resonant frequency with increasing stiffness, also decreasing coherence of the data. Directly after the test, the sample was placed back in the storage beaker of DI water and allowed to soak for at least a minute to assure complete resaturation. This procedure was adopted instead of just brushing water in the sample because of inconsistent data, (most likely due to incomplete rehydration of the NafionTM). Since gravity pulls the water to the bottom of the beam it is difficult to fully rehydrate the top of the beam. Lightly roughening the surface of the NafionTM (similar to the prep used to electrode the transducers) also seemed to allow the NafionTM to remain uniformly hydrated for a longer

amount of time.

Since damping is most apparent near resonance, this will be frequency range of interest for determining GHM parameters (in addition to near DC levels for static modulus verification). This was done for two different width samples, one 5mm, one 4mm. The lengths of the beams were varied by changing the amount of the beam extending from the fixture clamp. The lengths of the beams were varied from 18mm to 24mm, corresponding to the second sliding-pinned BC mode (first observed) natural frequencies in the range of 60 to 150Hz. These lengths were chosen for two reasons. The first reason is because of the testing apparatus. The load cell used to measure the force output from the beam has a natural frequency of 210Hz, and its output response decreases at 40dB/decade afterwards (attenuated below 0dB after 300 Hz). This sets the practical upper limit of frequency response that can be measured because the measured resonant peaks of the beam at high frequency are often not smooth. This upper limit is also encountered sooner because of the fact that the first mode of the beam in the sliding-pinned boundary condition is canceled so the first peak observed is at the second mode natural frequency. The lower limit of frequency response is limited by the stiffness of the beam and the resolution of the load cell. Using a longer beam to lower the resonance frequency in an attempt to stay below the load cell roll off makes it increasingly difficult to measure the already small force output from the beam and again the resonant peaks and overall behavior is not 'clean'. It is also desirable to have the beam resonance away from the load cell dynamics in the uncompensated data to lessen the possibility of losing response characteristics when post processing is applied to remove the load cell and signal conditioning circuit dynamics. So transducer length is a compromise, a shorter stiffer beam gives better signal coherence (due to higher force signals) but can push the resonance frequency higher than practical limit to avoid the load cell roll off, a softer beam that has a resonant peak below the load cell resonance makes it difficult to get good coherence because of the lower force signal level away from resonance, and the beam should not have a second mode resonance near the load cell resonance. The second reason for using the geometries here is that they are what has been typically explored in other works and allows useful comparison of results and response. Ideally the viscoelastic properties would be observed over a wide frequency range, and accurately represented over the frequency range of use and influence.

3.2 Minimization Approach

The Matlab function `fmincon` was utilized for this work. It performs constrained nonlinear optimization useful for the task of optimizing the GHM parameters. The cost function utilized for the minimization was the square of the difference between the experimental and simulated frequency response.

$$Cost = \sum_{j=1}^{npoints} (u_{measured}(j\omega) - u_{predicted}(j\omega))^2, \quad (3.1)$$

The magnitude and phase of the response were compared separately and summed together, this allows the weight of the phase to be adjusted to allow a trade off between the magnitude and phase error of the response. Expanding Equation 3.1, we obtain

$$Cost = \sum_{j=1}^{npoints} (|u_m(j\omega)| - |u_p(j\omega)|)^2 + \alpha (|\angle u_m(j\omega)| - |\angle u_p(j\omega)|)^2, \quad (3.2)$$

where $u_m(j)$ is the measured and $u_p(j)$ is the predicted complex frequency response and j is the index of a vector of desired frequency comparison points, α allows the relative weighting of the phase error compared to the magnitude error (chosen as 0.75 in this work as a good trade off). Lower and upper bounds were placed on the values used in the minimization of the cost function, implemented in the `fmincon` call in the processing routine. `Fmincon` also requires a seed for the optimization routine initialization, the values used for $\hat{\alpha}$, $\hat{\zeta}$ and $\hat{\omega}$ were, 1, 60, and 20000 respectively. These values were arrived at after trying other seed values and most often ending near these results after more iterations. Allowing a slight variation in the density (enforced with the `fmincon` bounds) was also experimented with in the minimization routine. This was found to increase fitting accuracy very little, in fact GHM fit results were often worse and the density would go to the limit imposed most every time. This is felt to be because the density has a very direct effect on the predicted resonant frequency, as opposed to the subtle stiffening of the modulus by the viscoelastic modulus. Without holding one fixed, there was not a unique solution, increasing density lowers the natural frequency while increasing the GHM stiffness increases natural frequency, both can be done with no net insightful result. A logarithmic frequency sample spacing was utilized for comparison over two adjoining regions, allowing more or less relative weight between the low frequency and near resonance response. A typical good fit response can be seen in Figure 3.1, where the circles indicate frequencies evaluated in the cost function, the blue

line is experimental data and the red line is the simulated response, the resulting complex modulus function is also plotted over the range of error minimization for reference. An

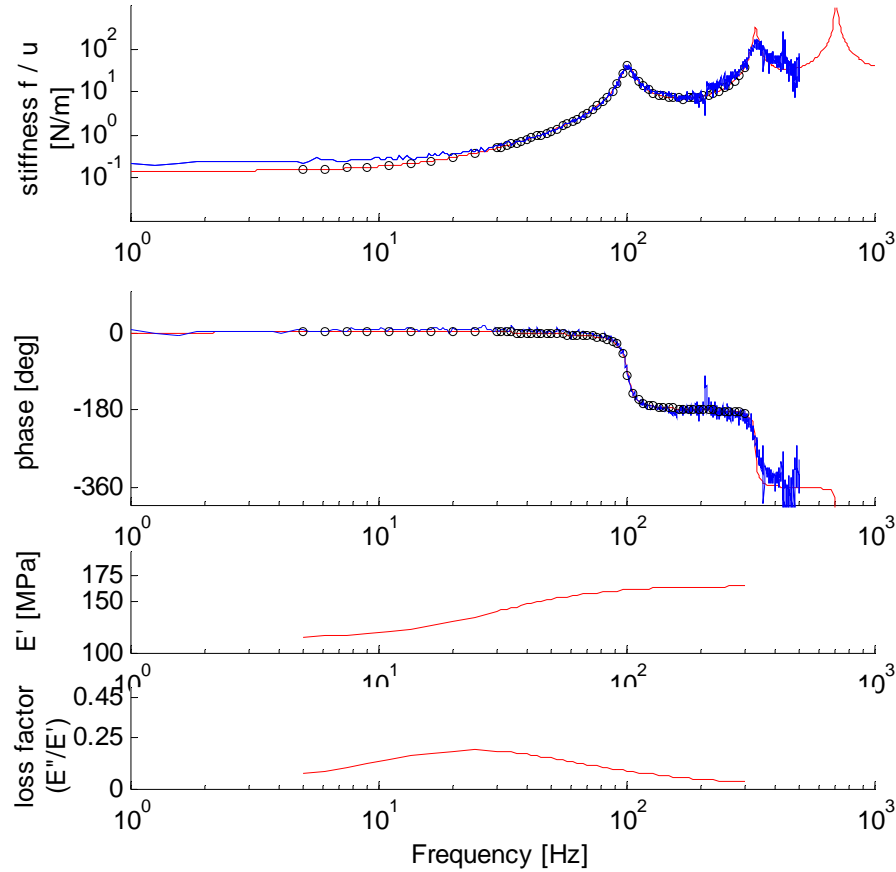


Figure 3.1: GHM fitting results for run10, blue is measured data, red is predicted response, circles indicate frequency points of comparison in the cost function. Parameter fit results: $\hat{\alpha}=0.451$ $\hat{\zeta}=53.87$, $\hat{\omega}=20E3$, with a cost of 39.49.

example of a more difficult run to fit to is in Figure 3.2, the cost is higher than for run10 and the GHM parameters are different. Note the peak of the data is not captured by the model and the phase roll is slower in the model as well. This could be due to a number of effects, from inaccuracies in the free length measurement to hydration effects. Most of the cost difference is in the higher frequency where the coherence was low, all runs were sampled over the same frequency range, regardless of each run's resonant frequency. The cost of the various fits ranged from as low as 25 to as high as 500, but none were visually determined to be poor enough to omit, most of the high costs were due to decreasing coherence at

the end of the frequency comparison range. Each run was optimized individually and the

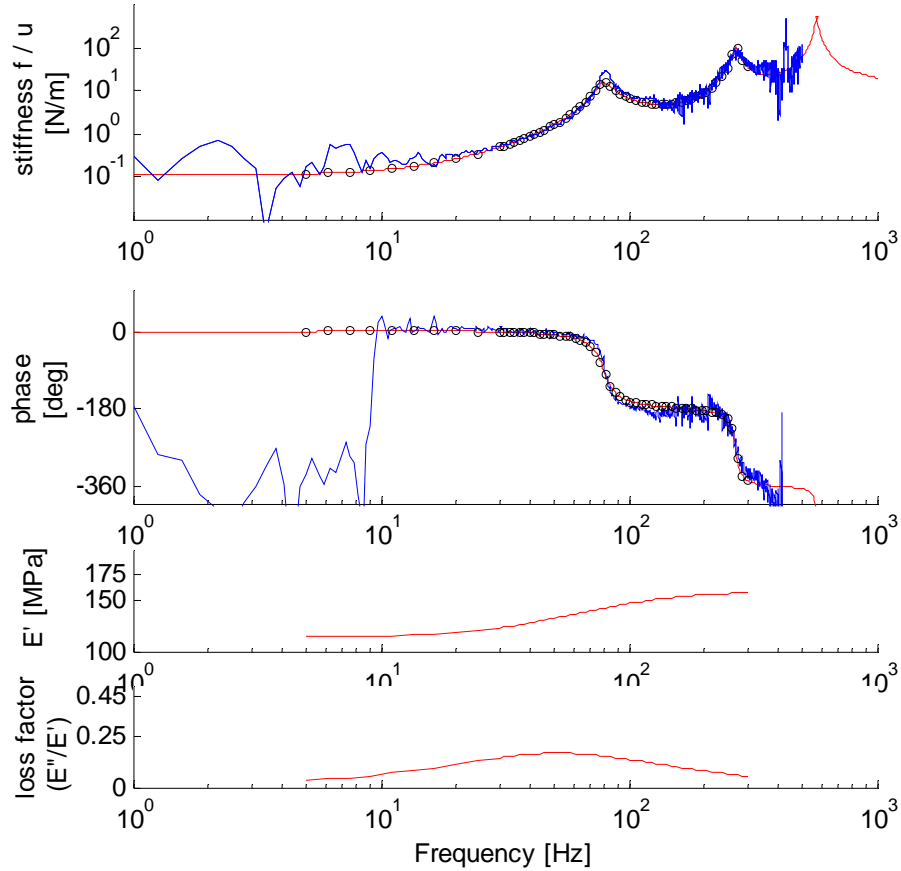


Figure 3.2: GHM fitting results for run08, blue is measured data, red is predicted response, circles indicate frequency points of comparison in the cost function. Parameter fit results: $\hat{\alpha}=0.397$ $\hat{\zeta}=26.19$, $\hat{\omega}=20E3$, and a cost of 502.18

different GHM values were substituted into the modulus function, Equation 2.51. The various values and the resulting modulus systems can then be compared and an average approximation of the complex modulus could be chosen to approximate the viscoelastic properties of NafionTM over the working frequency range (1-500Hz). The variation among the GHM parameters could be due to inaccuracies in transducer dimension measurements, or the level of hydration during testing.

3.3 Data Validation

Nine data runs were analyzed with different beam geometries and the resulting GHM parameter fit (see Table 3.1) modulus functions can be seen in Figure 3.3. The storage modulus (E') is the real part of the complex modulus and the loss factor is the imaginary part divided by the real part (E''/E'). These curves are similar to an expected viscoelastic modulus. For the final GHM parameter values and resulting modulus function, the storage modulus increases to ~ 170 MPa from the 114 MPa static value and the peak loss factor of ~ 0.18 occurs at 33Hz.

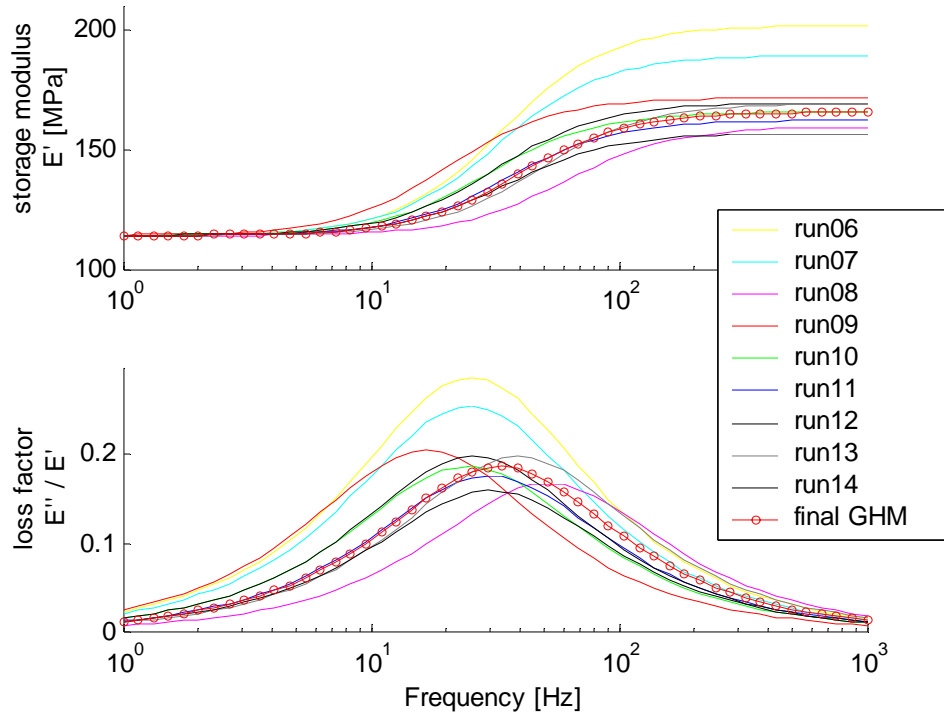


Figure 3.3: Modulus curves for Nafion[™] GHM fitting results: final result $\hat{\alpha} = 0.45$, $\hat{\zeta} = 40$, and $\hat{\omega} = 20000$.

These final GHM parameters were chosen because they appear to give a good average of the resulting modulus functions. The GHM parameters were not simply averaged because they are really a matched pair $\hat{\alpha}$ and $\hat{\zeta}$. Since $\hat{\omega}$ never really changed in the optimization, it is possible that it is not truly independent of the other parameters, and has the least effect on the resulting modulus function. It was observed that $\hat{\alpha}$ directly effects the high frequency asymptote of the modulus, and when $\hat{\alpha}$ is increased, $\hat{\zeta}$ must be changed to restore

Table 3.1: Summary of GHM parameter fitting results for NafionTM

| Run | L_d [mm] | w [mm] | $\hat{\alpha}$ | $\hat{\zeta}$ | $\hat{\omega}$ | Cost |
|--------------|------------|----------|----------------|---------------|----------------|--------|
| 6 | 24.13 | 5.45 | 0.766 | 47.027 | 20000 | 98.76 |
| 7 | 24.13 | 5.45 | 0.658 | 49.468 | 20000 | 115.33 |
| 8 | 22.00 | 5.45 | 0.397 | 26.191 | 20000 | 502.18 |
| 9 | 20.00 | 5.45 | 0.502 | 78.171 | 20000 | 42.312 |
| 10 | 20.00 | 5.45 | 0.451 | 53.868 | 20000 | 39.49 |
| 11 | 18.00 | 5.45 | 0.4207 | 44.617 | 20000 | 28.583 |
| 12 | 18.00 | 5.45 | 0.4833 | 50.27 | 20000 | 48.33 |
| 13 | 22.00 | 5.45 | 0.482 | 33.34 | 20000 | 103.73 |
| 14 | 20.00 | 5.45 | 0.374 | 44.609 | 20000 | 25.18 |
| final result | | | 0.45 | 40 | 20000 | |

a similar shape to the modulus function if peak loss factor is to occur at the same frequency.

It should be noted that the parameter results shown here are not necessarily exactly the same when the minimization is run again, even with an cost difference threshold of 1e-9. Small variation was observed from optimization to optimization even using the same seed, but all results give similar modulus functions. The accuracy of the parameter finding could be increased if the modulus function could be measured directly instead of being embedded in the beam frequency response. Relatively large changes in the GHM parameters have less effect on the modulus function, and even less effect on the beam simulation response. These GHM parameters are not necessarily unique and other possible combinations can be used with similar model simulation results.

The last row of Table 3.1 is the final values of the GHM parameters used throughout the rest of this work, and will be utilized in the modeling section to compare input-output relationships in the next chapter.

3.4 KaptonTM Characterization

Since KaptonTM polyimide film was chosen as the encapsulation layer for model verification in the next chapter and is a polymer itself, the accuracy of the model can be increased by using single term GHM approximation for the material modulus representation instead of just a static value. The same characterization process was used for the KaptonTM as was for the NafionTM. Since the film used was an adhesive backed tape, the test samples

were created by folding the adhesive side of the tape onto itself to create a two-layer beam more easily testable. These test specimens were then trimmed to the shape of a rectangular beam, one 4.05mm, the other 3.4mm wide. These two beams were then placed in the fixture used to test the stiffness of the NafionTM samples. The KaptonTM static modulus (2.5GPa (Dupont, 2000a)) is considerably higher than NafionTM and the beam geometry used gave second mode sliding-pinned BC resonances between 170 and 450Hz. This frequency range was acceptable because this is the frequency range typically observed for resonance when the polymer transducers were encapsulated and tested in Section 4.3.2. Twelve different runs with the two KaptonTM samples were performed and the data was processed with the same method and cost function as was used for the NafionTM. All characterizations were run on the Tektronics with a bandwidth of 10Hz-1kHz with 4096 samples and 10 avgs. A larger number of averages was chosen here because there are no hydration issues with KaptonTM and time was not an issue. The tape used was specified to be 1mil of KaptonTM with 1mil of silicone adhesive, when the folded samples used for testing were measured, the total thickness was measured to be $140\mu m$. The thickness used in the modeling will be $50\mu m$ since it gives good static stiffness correlation to the encapsulation data and is closer to what was specified by the supplier, the static modulus was also chosen to be 2.0GPa since the silicone adhesive should have a lower modulus than the KaptonTM and will lower the bulk static modulus used. A plot of one of the characterization runs with it's corresponding curve fit can be found in Figure 3.4. A plot of the modulus functions from the various GHM parameter fits of the KaptonTM samples can be found as Figure 3.5. Table 3.2 is the values of the GHM values found by the minimization of the cost function. The 'fit range' column lists the frequency range a constant number of points were evaluated at in log space for the cost function. The range was modified per run to only contain information up to shortly after the first resonant peak. This was done because the resonant frequency was often high enough to lose clarity due to load cell roll off shortly after the resonance. The results indicate that KaptonTM is less viscoelastic than NafionTM and sample handling supports this result.

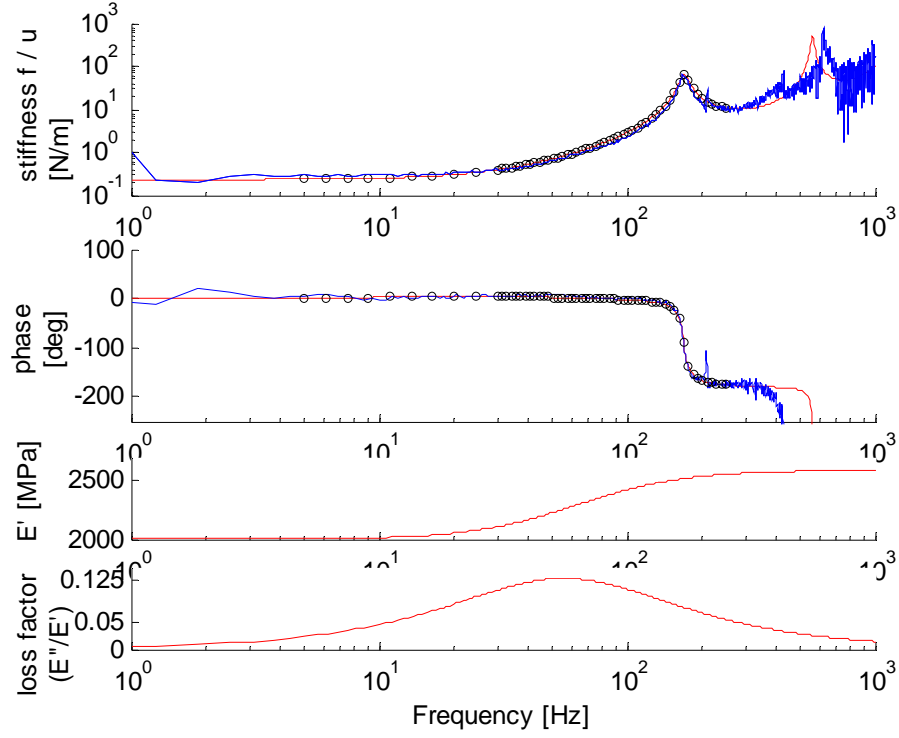


Figure 3.4: KaptonTM GHM fitting results for run 2, blue is measured data, red is predicted response, circles indicate frequency points of comparison in the cost function. Parameter fit results: $\hat{\alpha} = 0.29$, $\hat{\zeta} = 25$, $\hat{\omega} = 20000$, with a cost of 37.95.

Table 3.2: Summary of GHM parameter fitting results for KaptonTM

| Run | L_d [mm] | w [mm] | $\hat{\alpha}$ | $\hat{\zeta}$ | $\hat{\omega}$ | Cost | Fit range | |
|--------------|------------|-----------------------|----------------|---------------|----------------|-------|-----------|--|
| 1 | 24.00 | 4.05 | 0.38 | 14.7 | 20000 | 23.34 | 1-300Hz | |
| 2 | 28.00 | 4.05 | 0.29 | 25.0 | 20000 | 37.95 | 1-250Hz | |
| 3 | 24.00 | 4.05 | 0.44 | 16.0 | 20000 | 19.66 | 1-300Hz | |
| 4 | 22.00 | 4.05 | 0.43 | 13.8 | 20000 | 17.8 | 1-400Hz | |
| 5 | 19.20 | 4.05 | 0.28 | 7.8 | 19900 | 36.3 | 1-400Hz | |
| 6 | 18.00 | 4.05 | 0.28 | 4.99 | 20000 | 62.9 | 1-500Hz | |
| 7 | 16.00 | data quality too poor | | | | | | |
| 8 | 19.12 | 3.4 | 0.19 | 7.71 | 20000 | 68.1 | 1-400Hz | |
| 9 | 26.5 | 3.4 | 0.45 | 24.3 | 20000 | 19.6 | 1-300Hz | |
| 10 | 24.00 | 3.4 | 0.52 | 19.7 | 20000 | 36.3 | 1-400Hz | |
| 11 | 22.00 | 3.4 | 0.38 | 16 | 20000 | 16.6 | 1-400Hz | |
| 12 | 19.00 | 3.4 | 0.5 | 13.7 | 20000 | 54.8 | 1-500Hz | |
| final result | | | 0.30 | 15 | 20000 | | | |

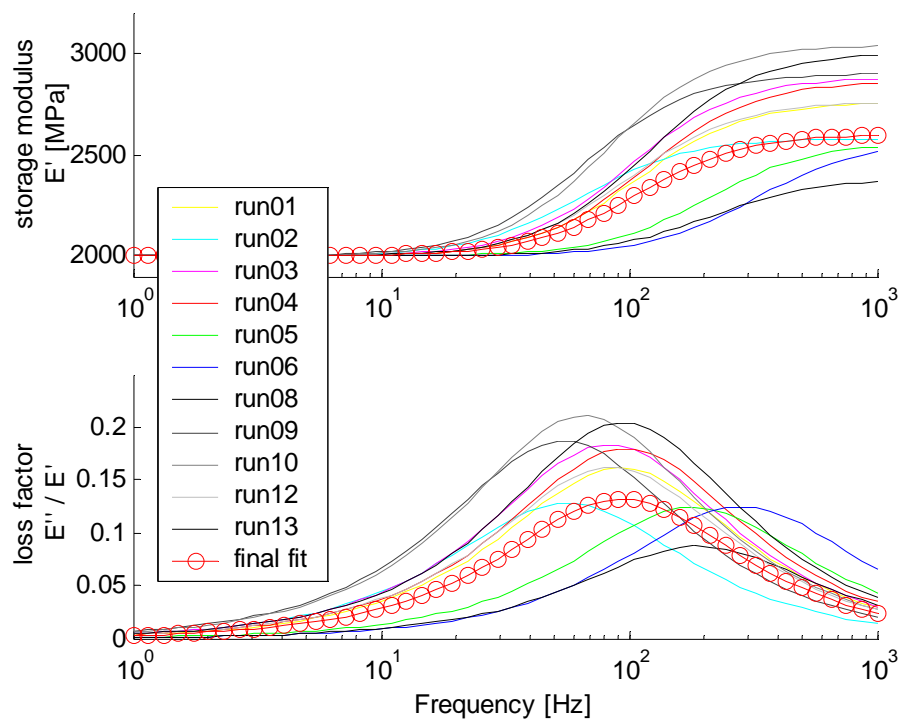


Figure 3.5: Modulus curves for Kapton™ GHM fitting results: final result $\hat{\alpha} = 0.3$, $\hat{\zeta} = 15$, and $\hat{\omega} = 20000$

Chapter 4

Three-Layer-Beam Model

Verification

The following chapter outlines the parameter values used in the ionic polymer transducer model and compares the model to experimental data for both unencapsulated and encapsulated ionic polymer transducers. The mechanical response as well as various input-output relationships are compared. Two frequency ranges of comparison are examined, low frequency (up to and including the first mode resonance), to compare multi-layer theory modeling results to those of Newbury and Leo (2003b) over a similar frequency range; and high frequency (as high as data quality allows, typically $>500\text{Hz}$), to examine trends observed in the higher frequency response of polymer transducers. Four transducers of various sizes were used for this comparison, from two different batches, all using Copper/Platinum alloy electrodes with a gold over layer (process developed in Bennett (2002)). See Table 4.1 for a summary of the geometries.

The electroding process requires boiling of the transducers at various times and reduces the static modulus to 64 MPa (Dupont, 2000b). Because of the fact that NafionTM was characterized in the previous chapter at the 114 MPa hydration state, these transducers were all dried and allowed to rehydrate in DI water at room temperature. The drying process involved placing the transducers in an oven at 60°C and -20 inHg gauge pressure for 30 minutes. They were then placed in Lithium hydroxide at room temperature for several days to improve the transducer performance (through ion exchange).

Once the polymer was placed into the clamp for testing, it was not moved in order

Table 4.1: Transducer geometry used for model verification

| Transducer | Batch | L_t [mm] | L_d [mm] | w [mm] | t [μm] |
|-------------|-------|------------|------------|----------|-----------------------|
| I | A | 28 | 17.7 | 3.84 | 200 |
| II | B | 32 | 20.1 | 5.2 | 200 |
| III | A | 28 | 17.3 | 4.14 | 200 |
| IV | B | 30 | 19.13 | 5.4 | 200 |
| I (encap) | A | 28 | 21.3 | 3.84 | 300 |
| II (encap) | B | 32 | 20.7 | 5.3 | 300 |
| III (encap) | A | 28 | 19.2 | 4.6 | 300 |
| IV (encap) | B | 30 | 21.1 | 5.4 | 300 |

to minimize the inconsistency associated with moving and remeasuring the length of the exposed polymer, and to allow direct comparison among the tests for each transducer. Baseline data was taken for the four transducers, then they were encapsulated with KaptonTM tape and retested to observe the change in transducer performance. This is done so that the relative effects of the tape will be better observed because the transducers were evaluated before the tape was applied. A poor transducer should perform poorly before it is encapsulated and poor encapsulated performance will be expected.

4.1 Model Parameters

The physical parameters needed for the model terms developed in Chapter 2 will be defined and discussed in this section. All models were created and their frequency responses were simulated in Matlab. As a general process, all parameters were defined, the modulus functions were assembled and then the various modal expansion summations were computed. Next the various input-output relationships were defined and computed using the previously defined terms. Once these i/o relationship systems are created, they can be simulated over a desired frequency range, which is typically the frequency range of the data used for comparison.

The frequency dependent coupling coefficient function d was used directly from Newbury (2002) and was found to work well with the transducers for this work. The Laplace domain representation can be found in Equation 4.1.

$$d(s) = (2.63e - 6) \frac{(s - 0.0937)(s + 0.11)(s + 70)}{(s + 0.126)(s + 0.602)(s + 50)(s + 150)} \quad (4.1)$$

This is despite the creation process and performance differences between the transducers used in this work and those used in Newbury (2002). The transducers used in Newbury (2002) and Newbury and Leo (2003a) were created by Dr. Shahinpoor at the University of New Mexico and the transducers used in this work were created at Virginia Tech with the process outlined in Bennett (2002). The fundamental differences are the thickness of the electrodes and resulting stiffness of the transducers, the static stiffness reported in Newbury and Leo (2003b) is four times that of the transducers used here.

The electrical impedance function (Z_p) as well as the dc resistance (R_{dc}) used in Newbury and Leo (2003b) was found to be much too low for the transducers in this work. Instead of going back to first principles as was done in Newbury (2002), the electrical impedance of encapsulated transducer IV was selected as a good average of the impedances measured (there was little variation between the measured blocked impedance) and Z_p was approximated by a 5th order system fit to the data using *invfreqs* in Matlab. The dc resistance of each polymer was measured by applying 1 Volt across the electrodes of the polymer and measuring the resulting current with a HP digital voltmeter, all transducers had a resistance very near $10\text{k}\Omega$ (possible because of their similar geometries). This result is much higher than the value reported in Newbury (2002) and is most likely due to the difference in manufacturing process used in the fabrication of the transducers used in this work.

Table 4.2 is a summary of the values used in the models for this chapter.

Table 4.2: Summary of parameters used in model validation

| Material Parameters | | |
|--|----------------------|---|
| Density of Nafion TM | [kg/m ³] | 2000 |
| Static modulus of Nafion TM | [MPa] | 114 |
| Thickness of Nafion TM layer | [μm] | 200 |
| GHM parameters of Nafion TM | | $\hat{\alpha} = 0.45, \hat{\zeta} = 40, \hat{\omega} = 20\text{E}3$ |
| Density of Kapton TM layer | [kg/m ³] | 1420 |
| Static modulus of Kapton TM layer | [GPa] | 2.0 |
| Thickness of Kapton TM layer | [μm] | 50 |
| GHM parameters of Kapton TM layer | | $\hat{\alpha} = 0.3, \hat{\zeta} = 15, \hat{\omega} = 20\text{E}3$ |
| Electrical Parameters | | |
| R_{dc} of all transducers | [k Ω] | 10 |
| Z_p | [V/A] | curve fit to run07 electrical impedance |

4.2 Electrode Stiffness Effects

In order to justify the combination of the electrodes with the NafionTM for this chapter and to use the KaptonTM as the passive layer in the model and essentially neglect the electrodes, mechanical stiffness (Equation 2.48) was measured for electroded samples and compared to the expected response of an un-electroded NafionTM sample. Figure 4.1 is a plot of the measured stiffness of a transducer and its modeled response using a single layer of NafionTM with the distributed parameter sliding pinned beam model. Since there is

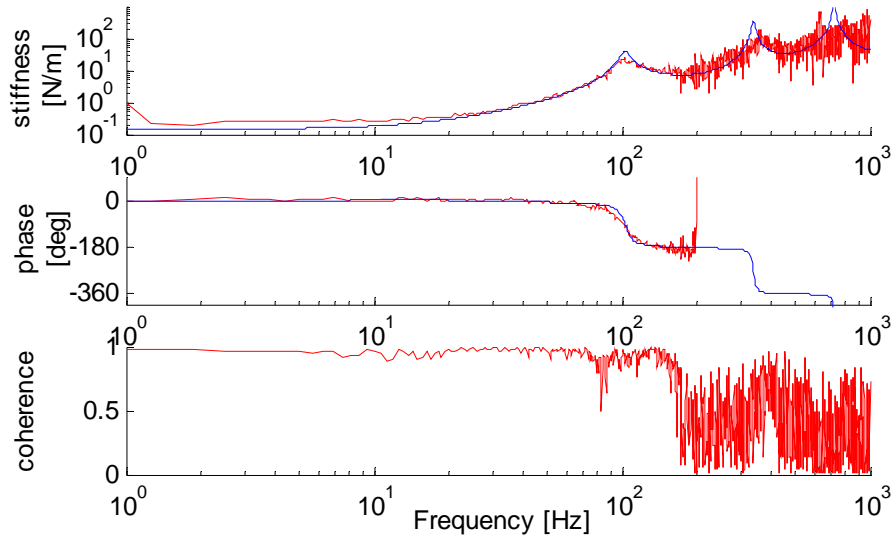


Figure 4.1: Electroplated sample vs single layer model (NafionTM)

not a discernable difference between the response of the predicted NafionTM beam and the electroded sample, the electrodes are assumed to have negligible contribution to the stiffness of the transducer (under the current plating and electroding process). This simplification is validated only for NafionTM 117 (where 117 is a thickness specification used by Dupont, converts to $180\mu\text{m}$) used in this work. The electrodes could conceivably have an effect on the mechanical response of ionic polymers when thinner NafionTM is used, since the electrodes become stiffer relative to the stiffness of the overall beam.

In the interest of investigating whether electrode stiffening could be observed in NafionTM 117, additional separate (from the four used with the KaptonTM encapsulation) NafionTM 117 samples from the same batch as two of the four samples were electroplated with additional gold. Figure 4.2 is a plot of samples electroded for increasing lengths of time

corresponding to higher charge per unit area values, which in theory increases the amount of gold deposited. The samples were electroplated with charge per areas of .1, .2, .3, .4, and .8 A-min/cm². The surface conductivity increased with charge density and additional gold was visually deposited onto the electrodes. The small variation of natural frequency

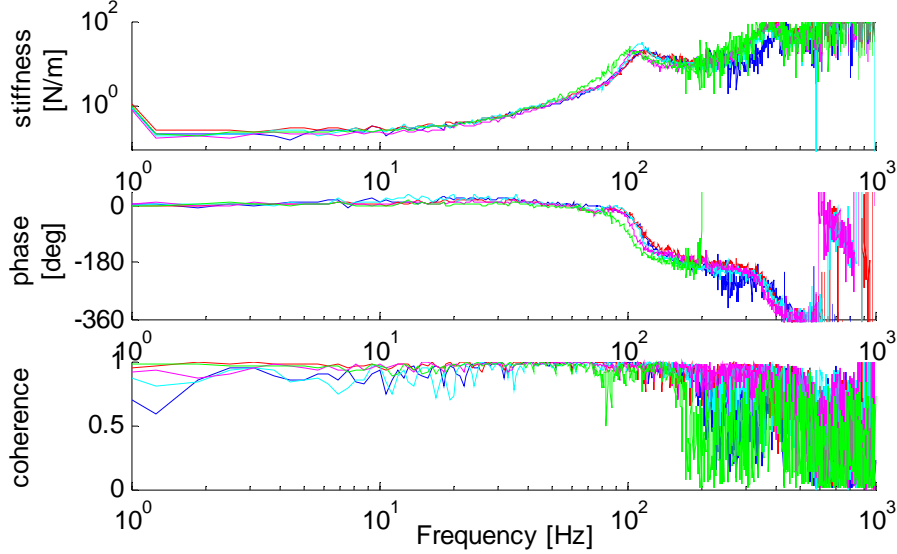


Figure 4.2: Stiffness test results of electroplated samples

observed in Figure 4.2 is due to the small differences in the width of the samples (the free length was kept constant), and no trend of stiffness change can be determined. Therefore the electrode contribution to the mechanical stiffness of the transducers will be neglected for the remainder of this work.

4.3 Low Frequency Range Model Comparison

4.3.1 Base Transducer Mechanics (Unencapsulated)

This section will compare the model simulation to experimental results over the frequency range up to the first mode natural frequency for unencapsulated ionic polymer transducers. This will be the baseline used to evaluate the change in performance of each transducer after encapsulation. The same three-layer model will be used as developed previously, with the exception that t_2 will be set to zero for the non encapsulated data sets. Figures of all the recorded data runs vs their model simulation results can be found in the Appendix. A good and bad model match result of the unencapsulated transducers tests will be

presented here for comparative purposes. The data sets taken include mechanical stiffness $(\frac{f}{u})^i$ (Equation 2.48), free deflection $(\frac{u}{v})^f$, sensing response $(\frac{q}{u})^v$, blocked force $(\frac{f}{v})^u$, and electrical impedance $(\frac{v}{i})^u$.

Mechanical Stiffness Modeling

The first unencapsulated transducer presented will be referred to as I. It is included here as a typical good transducer overall response. While some test runs of other transducers might have given a better response in one of the tests taken, other characteristics were not as good.

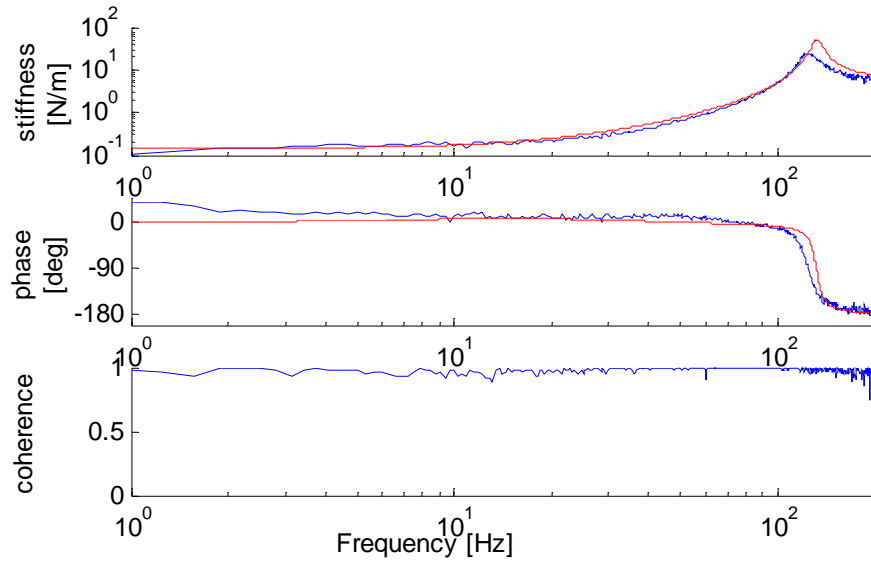


Figure 4.3: Stiffness test results vs model for unencapsulated transducer I, blue is measured data, red is model prediction.

Figure 4.3 is a plot of the mechanical stiffness of transducer I, measured vs predicted. The force signal is direct from the TMO-1 signal conditioner and the linear potentiometer used to measure the low frequency response of the test matches the model very well, but the response near resonance is slightly off ($\sim 8\text{Hz}$) and the magnitude predicted is roughly twice what was measured. However the shape of the response is very similar to the predicted response, which supports the GHM parameter selection. Inconsistencies could be due to a number of aspects of the model. The measurement of the free length of the beam could have been in error. It is difficult to measure L_d to a high degree of certainty and this error changes the resonant frequency by $1/L_d^2$. Also if the NafionTM viscoelastic approximation

is too stiff, it would push the predicted resonance higher than actual. Most likely these are all factors in the error of the model.

Figure 4.4 is a plot of the mechanical stiffness test results for transducer III vs the predicted model results. The low frequency stiffness again correlates well between the model

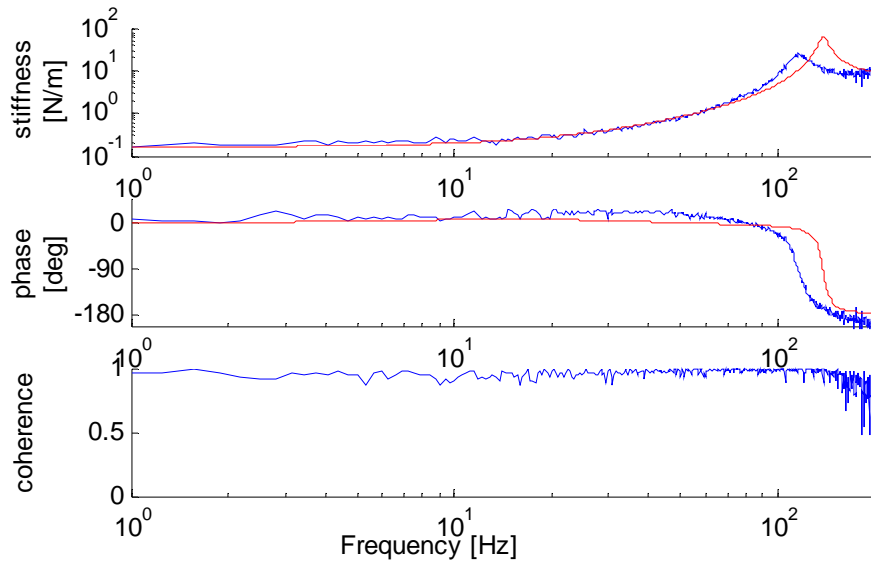


Figure 4.4: Stiffness test results vs model for unencapsulated transducer III, blue is measured data, red is model prediction.

and the experimental results. Behavior near the resonance is worse than transducer I; the peak responses are different by approximately 20 percent and the measured response is little more than a third of the predicted response. These two transducers are indicative of the inconsistent polymer behavior observed throughout this work. Repeatable results even with the same transducer from test to test is often a challenge to achieve.

Free Deflection

Figure 4.5 is a plot of the measured free deflection of transducer I along with the predicted response. The low frequency response of the lumped parameter model matches well with the measured results, only over predicting the response by approximately 10 percent. The distributed parameter model however overpredicts the dc response, this could be for various reasons. One reason could be that in the magnitude of the modeled applied moment is unknown and was arbitrarily scaled down to match the dc value of the encapsulated model's free deflection (dc levels match for encapsulated runs, discussed later). It is also unlikely that

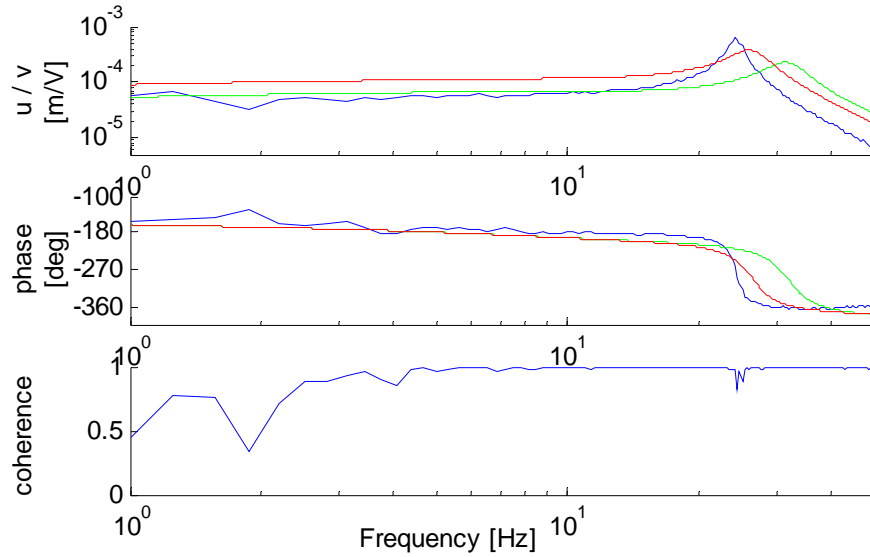


Figure 4.5: Free deflection test results for unencapsulated transducer I: blue is data, red is distributed parameter model, green is lumped parameter model.

the distributed moment is constant along the length (as assumed). the resistance along the length of the electrode could produce a large amount of the actuation current and subsequent voltage drop to occur near the base of the transducer where path resistance is lowest, tapering off to some value by the tip of the beam. This would in effect create a decreasing moment along the length of the beam. Future investigation of true mode shapes as a function of electrode conductivity could give insight into this possible phenomenon. Both models overpredict both the damping present and the natural frequency and underpredict the peak response of the transducer for the first mode of the cantilever beam. Another attribute to notice is that the cantilever distributed parameter approximation is closer to the measured natural frequency than the lumped parameter representation, indicating a better match to the system and an increase in modeling accuracy. Trends shown by both models are consistent with polymer free deflection behavior, however the damping shown in the data is much less than was characterized in Chapter 3. While boundary conditions should have no effect on the modulus of the material, possible future GHM characterization tests utilizing free deflection resonant behavior matching as additional criteria might give additional insight into the type of behavior seen for free deflection in this work because all free deflection predictions in this work are overdamped to some extent. Figure 4.6 is a plot of the free deflection performance of transducer III vs the predicted model response for both

the lumped parameter estimation and the distributed parameter estimation. Transducer

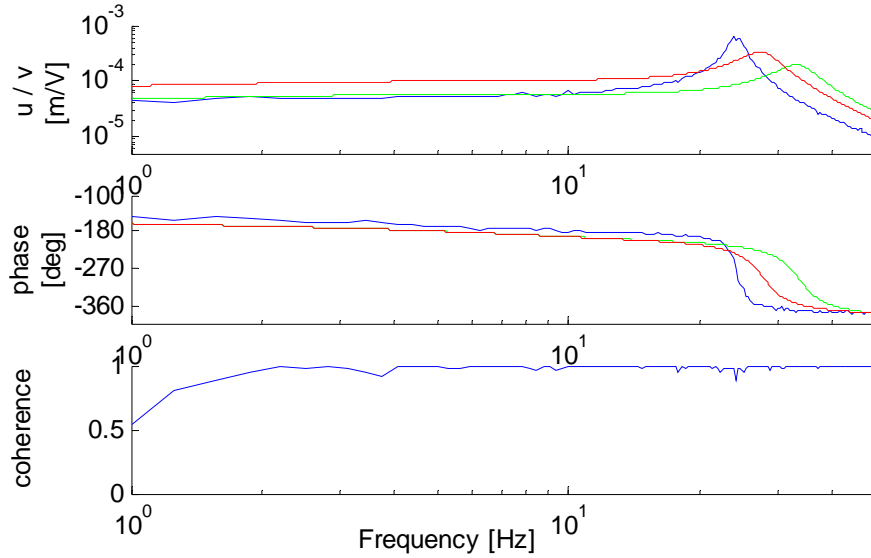


Figure 4.6: Free deflection test results for unencapsulated transducer III: blue is data, red is distributed parameter model, green is lumped parameter model.

III performance is only slightly worse than transducer I and the same observations apply, as expected.

Charge Sensing

Figure 4.7 plots the sensing response for transducer I, specifically $(\frac{d}{u})^v$, for both the model simulation and experimental results. It should be noted the sensing prediction of the model is strongly dependent on the d coefficient function used; the same function is used here as was found in Newbury and Leo (2003a) in order to investigate the correlation between the models and system results. The poor data coherence below 8Hz makes it difficult to observe any low frequency trends, but data above 8Hz approaches the model prediction in both magnitude and phase of the response. The low frequency coherence is reduced because of the high-pass filter effect of the charge sensing circuitry, the corner frequency is ~ 5 Hz. It should be noted that for d function estimation, either the blocked force (used in Newbury and Leo (2003a)), or it's negative reciprocal, charge sensing with displacement input, can be used to estimate the d function. This is possible due to the fact that besides measured transducer parameters, both i/o relationships are determined by only by the material modulus and the d function. Since often times the blocked force output of ionic

polymer transducers is difficult to measure due to its low magnitude, charge sensing might be a viable alternative relationship to use. This is because of the excellent sensing coherence attainable in charge sensing data. This alternate formulation is all dependent on the true reciprocity assumed and enforced by the model between sensing and actuation. Further research into the validity of this assumption might result in the better determination of the d function and increased accuracy of modeling.

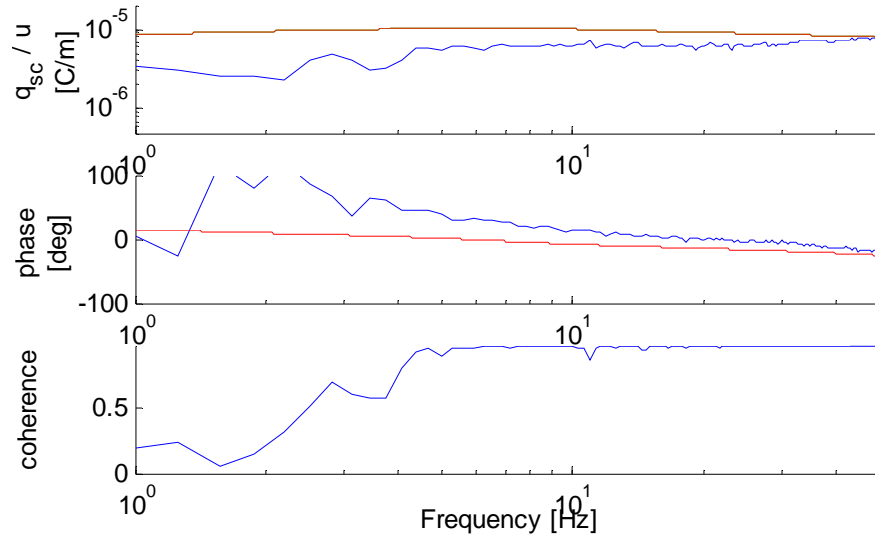


Figure 4.7: Sensing test results for unencapsulated transducer I

Figure 4.8 shows the test results of sensing for transducer III, the sensing magnitude performance is only half of that predicted by the model. This could indicate a poor transducer most likely caused by process inconsistencies, or an overestimation of the dc gain of the d function used in the model. A slight decrease in the dc gain of d would also slightly improve the prediction of transducer I.

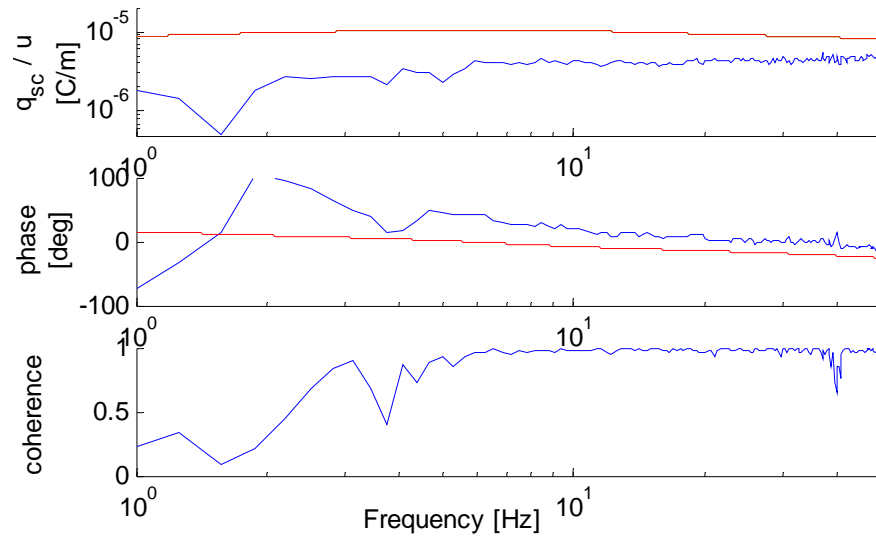


Figure 4.8: Sensing test results for unencapsulated transducer III

Blocked Force

Figure 4.9 is a plot of the blocked force for transducer I, two data sets are shown, the blue line a data test taken over a larger frequency range (truncated here) and the green line is a set taken from 1-20Hz to try to establish a dc level blocked force estimation (with a higher data coherence than attainable with broadband excitation tests). According to the model, the blocked force should follow the decreasing value of the d function. What is interesting is that the model actually underpredicts the blocked force, indicating a low dc gain of the d function, opposite what the sensing tests support. This could possibly be due to a difference in actual fundamental mechanisms responsible for sensing and actuation in ionic polymer transducers (not assumed with this model).

Figure 4.10 is a figure of the blocked force for transducer III, the low coherence makes it difficult to glean much from the data due to the scatter. Contrary to the underprediction of the blocked force response for transducer I, the results for transducer III are much closer, this is again with the reservation of relatively low data signal coherence.

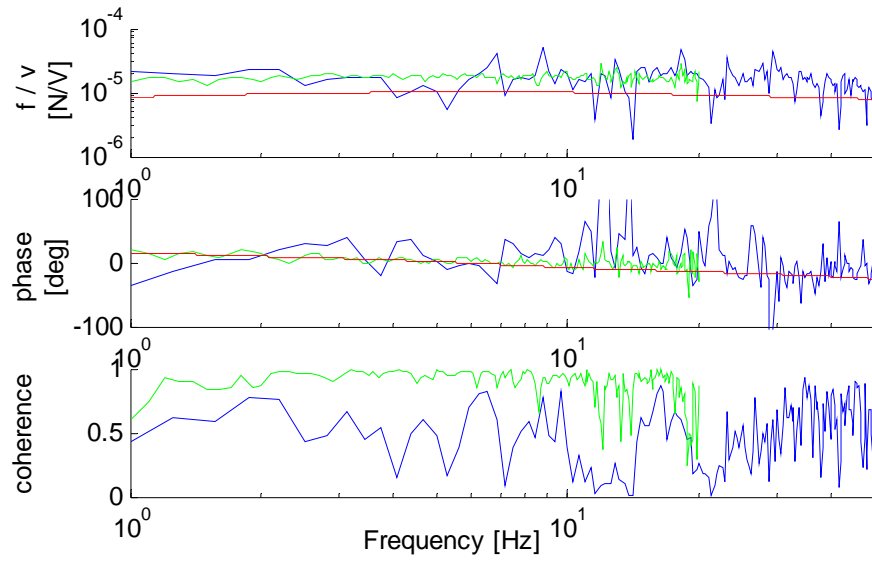


Figure 4.9: Blocked force test results for unencapsulated transducer I

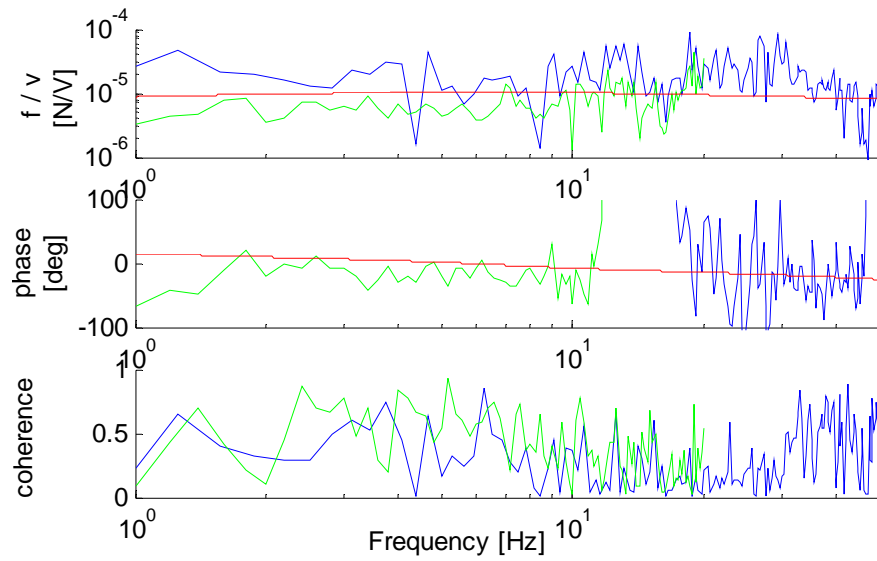


Figure 4.10: Blocked force test results for unencapsulated transducer III

Electrical Impedance

Figure 4.11 is a plot of the electrical impedance of transducer I. Electrical impedance is probably the most easily repeatable and predictable property of the polymers tested in this work. The only exception was one outlier (shown in the encapsulated section) where the impedance was an order of magnitude higher than predicted. In general the electrical impedance decreases with frequency to an asymptotic value, with the phase going from mostly capacitive to mostly resistive. The electrical impedance used for the model was one that was fit to run07 (encapsulated transducer II, (refer to Section 4.1)).

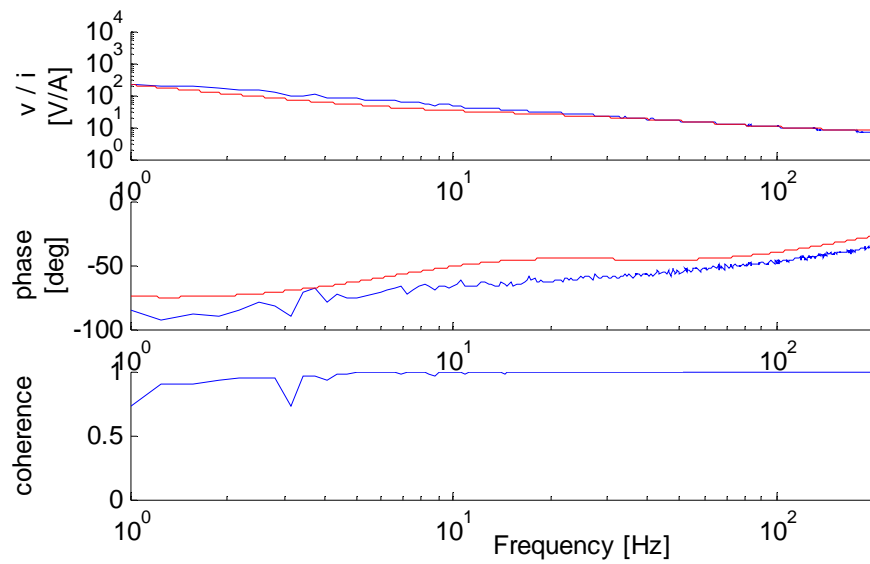


Figure 4.11: Electrical impedance test for unencapsulated transducer I

Figure 4.12 is plot of electrical impedance for transducer III, and again is a typical electrical impedance response.

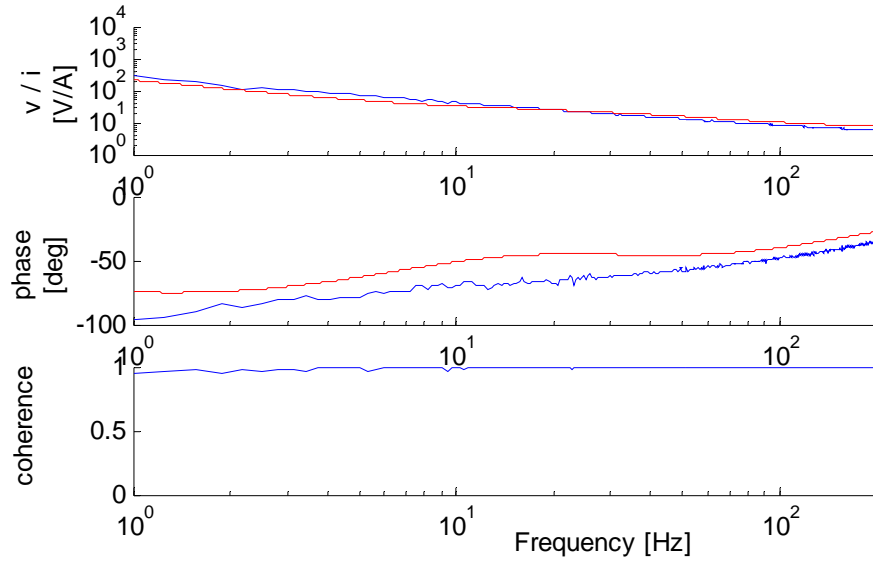


Figure 4.12: Electrical impedance test for unencapsulated transducer III

4.3.2 KaptonTM Encapsulated Transducers

This section will again present a best and worst transducer data set of the encapsulated tests taken, now for the KaptonTM encapsulated transducers.

Mechanical Stiffness Modeling

Figure 4.13 is a plot of the measured mechanical stiffness of transducer III encapsulated in KaptonTM. There is a substantial increase in the static stiffness when compared to the unencapsulated transducer test. This is consistent with the three layer theory. The stiffness of the model matches the measured response very well from dc levels through the first observed resonance (second mode of siding-pinned beam). This results supports and validates the separate characterizations of both the NafionTM and the KaptonTM film and indicates a good mechanical material model.

Figure 4.14 is a plot of the measured vs the predicted stiffness of transducer I. Again the stiffness matches very well across the entire range of valid data, the second resonant peak is believed to be a torsional mode of the beam not modeled in this work.

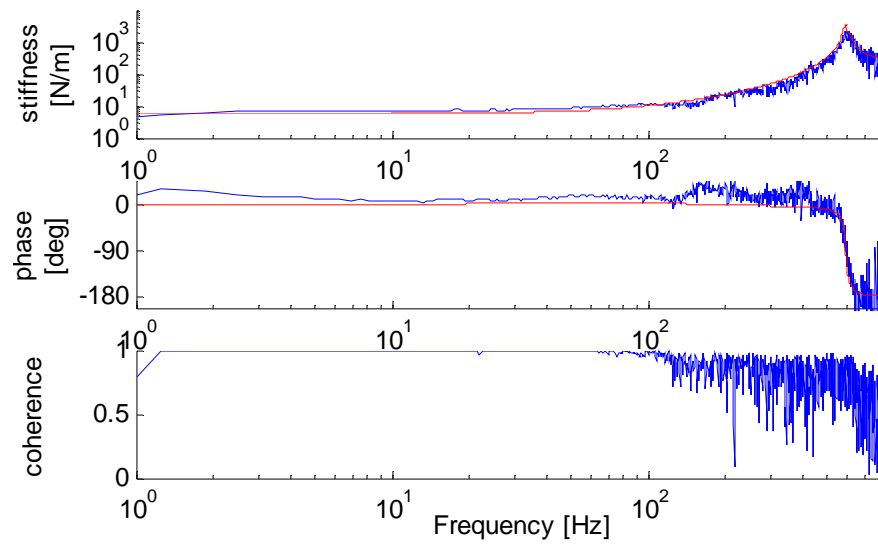


Figure 4.13: Stiffness test results vs model for encapsulated transducer III, blue is data, red is predicted response

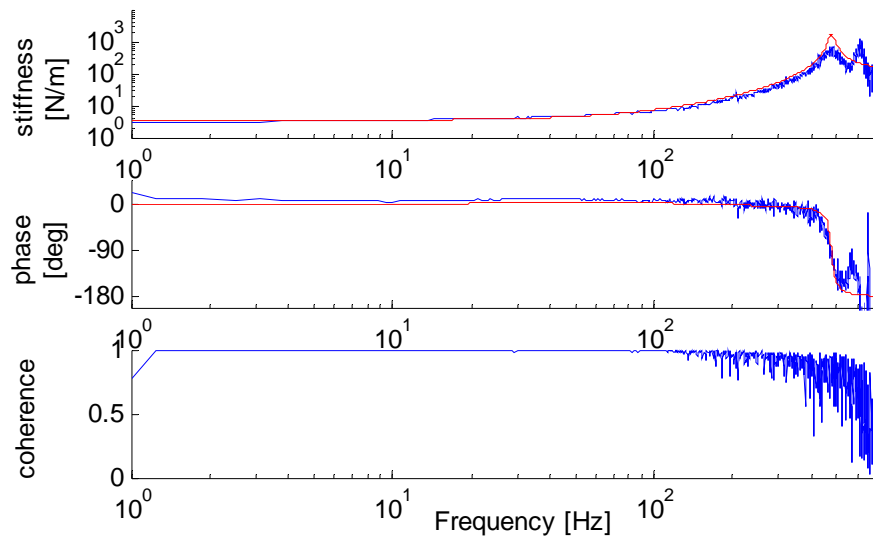


Figure 4.14: Stiffness test results vs model for encapsulated transducer I, blue is data, red is predicted response

Free Deflection

Figure 4.15 is a plot of the free deflection of transducer III after encapsulation in Kapton™ film. The response of the distributed parameter model matches the measured response well near resonance, but is overdamped and does not capture the complete peak, this overdamping is also evident in the slower phase roll of both models when compared to the measured transducer response. What is interesting about the encapsulation results is that the two best and worst transducers from the four are the same, but have now switched roles. Possible reasons for this could be linked to the order of magnitude increase in the electrical impedance of transducer III after encapsulation, this will be discussed in the following electrical impedance section. It should also be noted that in general in all tests the low frequency free deflection is reduced nearly an order of magnitude with encapsulation.

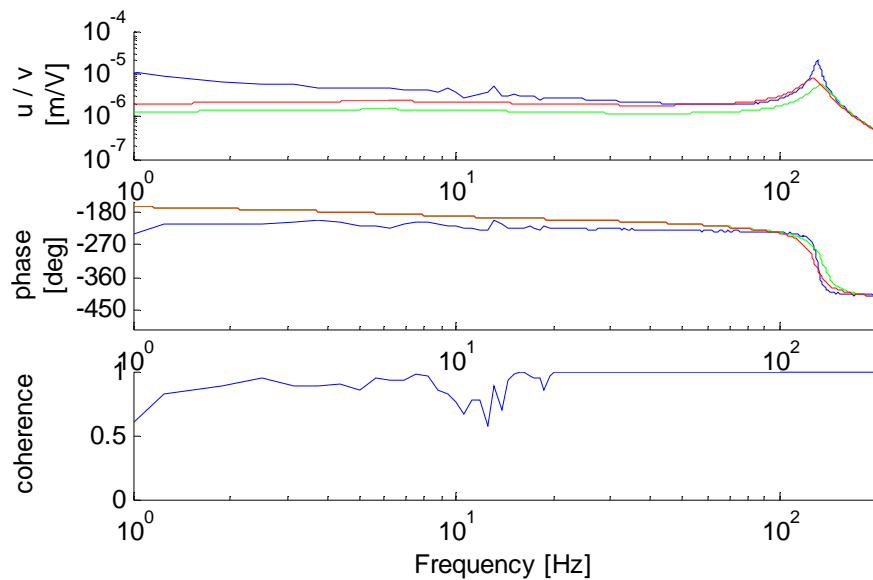


Figure 4.15: Free deflection test results for encapsulated transducer III: blue is data, red is distributed parameter model, green is lumped parameter model.

The free deflection response of transducer I shown in Figure 4.16 is close to the models' predictions for low frequencies, but still almost an order of magnitude lower than transducer III. The measured response approaching resonance differs greatly between model and measured data. Poor low frequency test data coherence could be partly at fault for this result, but is unlikely.

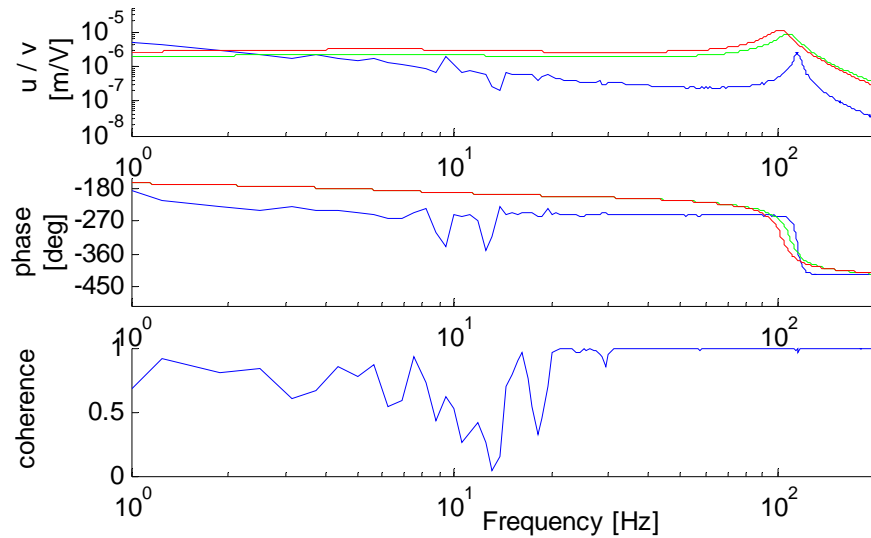


Figure 4.16: Free deflection test results for encapsulated transducer I: blue is data, red is distributed parameter model, green is lumped parameter model.

Charge Sensing

Figure 4.17 is a plot of the short circuit charge sensing with displacement input response of encapsulated transducer III. It is presented here as a good transducer when comparing the measured data to the modeled response. The modeled response does however seem to underpredict the apparent curvature of the sensing frequency response magnitude. The phase of the response for the lumped parameter model is out of phase by 180° due to the sign convention chosen in Newbury and Leo (2003a).

Figure 4.18 is a plot of the sensing response for transducer I after encapsulation and as seen in the free deflection response, the actual response is much lower than the predicted response of both modeling methods. This again is thought to be due to an increase in transducer impedance, most likely due to poor electrical contact in the test fixture. The measured sensing response seems to follow the same decreasing trend as the model, but starts at a much lower amplitude at low frequencies and decays faster with frequency, it is over an order of magnitude lower by 10Hz and gets worse over the frequency range shown.

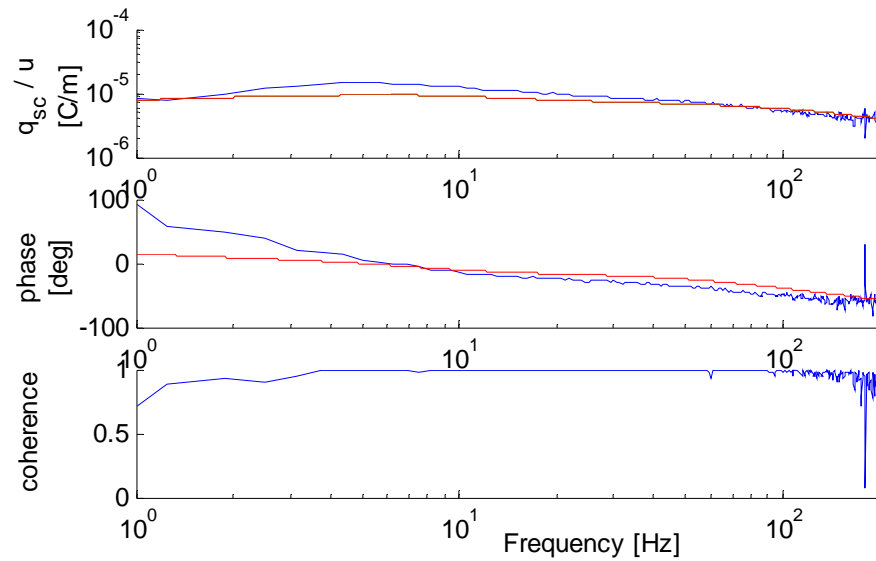


Figure 4.17: Sensing test results for encapsulated transducer III, blue is measured data, red is distributed parameter model, green is lumped parameter model.

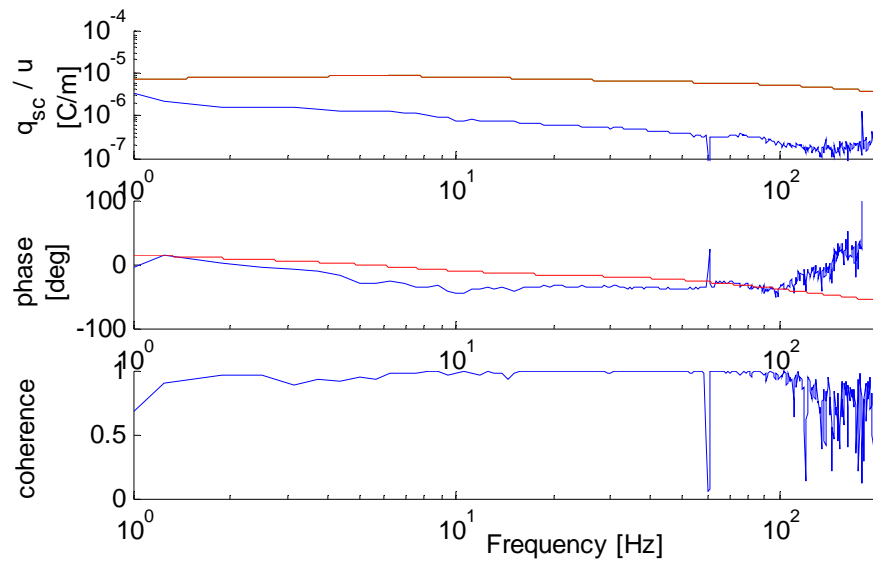


Figure 4.18: Sensing test results for encapsulated transducer I, blue is measured data, red is distributed parameter model, green is lumped parameter model.

Blocked Force

Figure 4.19 is a plot of the measured blocked force vs the predicted model response. The blocked force is considerably higher than the modeled response up to 20Hz. This should not be due to an inaccurate d function since the sensing response is very good for the transducer, leading to the inference that either reciprocity of ionic polymers believed to occur in this model does not hold, or the fundamental mechanisms are different. The encapsulation should not effect the blocked force as shown in Equation 2.26, however the blocked force of the same transducer (III) is twice as large when encapsulated than unencapsulated. The

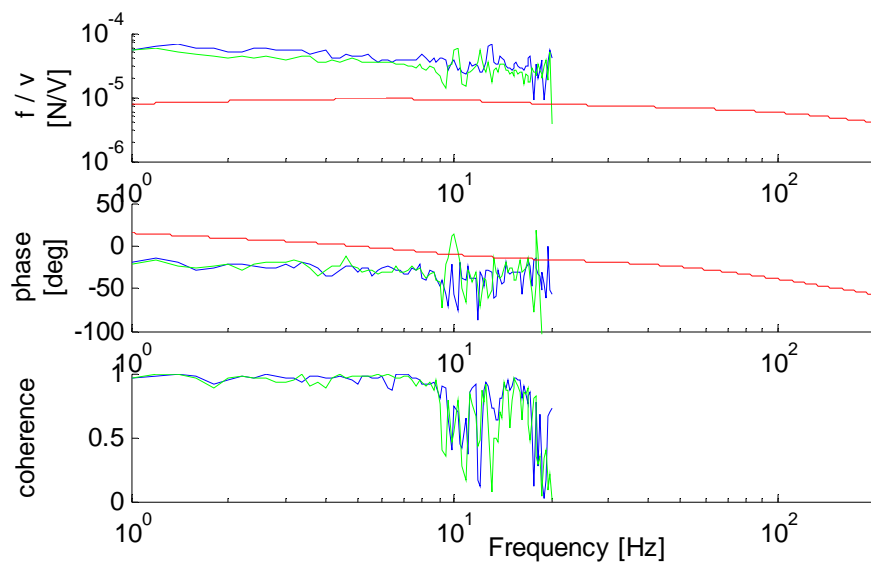


Figure 4.19: Blocked force test results for encapsulated transducer III

plot of the blocked force of transducer I in Figure 4.20 is difficult to assess due to the low signal coherence, but the blocked force is expected to be lower than predicted due to the reciprocity assumed between sensing and blocked force and the poor sensing performance of transducer I after encapsulation.

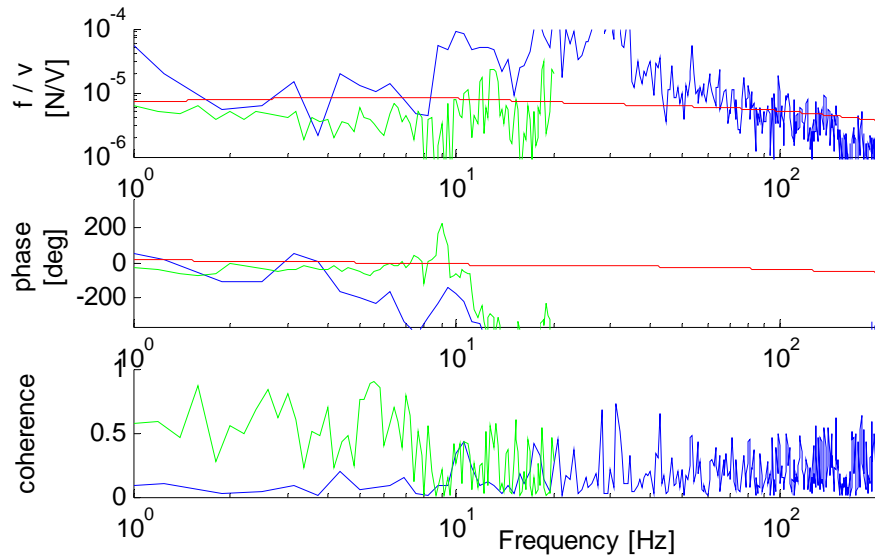


Figure 4.20: Blocked force test results for encapsulated transducer I

Electrical Impedance

Figure 4.21 is a plot of the electrical impedance for transducer III vs the predicted model response. The predicted and measured values correlate well, as typically seen in electrical impedance data.

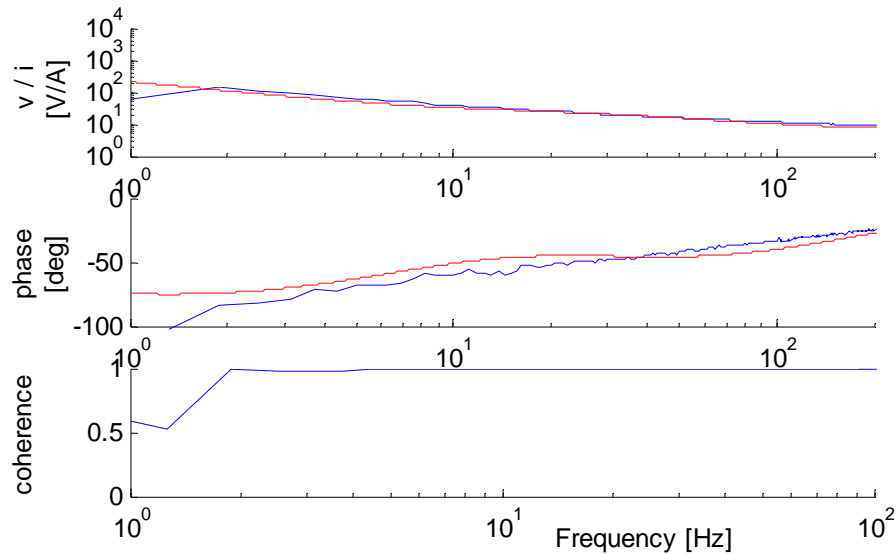


Figure 4.21: Electrical impedance test for encapsulated transducer III

Figure 4.22 is plot of the electrical impedance of transducer I after encapsulation. This is the one transducer tested that had a considerably higher impedance than predicted

and most note worthy, much higher than its unencapsulated value. This could be due to encapsulation, but is most likely due to poor contact between the electrodes and the test fixture. The encapsulation process could have caused an increase in the electrode resistance, possible slight separation of the electrode, although no change was visually apparent, and this would have thrown off the stiffness measurement for the sample, which was not observed. Tests were performed with other polymers after this test was taken with normal results indicating that it was not a data acquisition or circuitry problem. The increased electrical impedance of this transducer and subpar performance in all measured i/o relationship aspects points to a correlation between high electrical impedance and poor transducer performance.

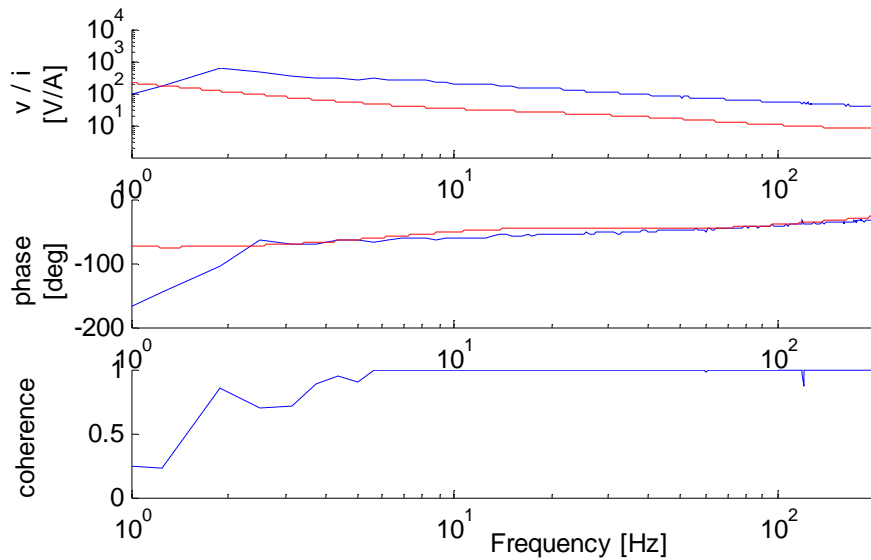


Figure 4.22: Electrical impedance test for encapsulated transducer I

Table 4.3 summarizes the low frequency results of the unencapsulated and encapsulated ionic polymer transducers.

Table 4.3: Table of comparison of low frequency transducer response change with encapsulation

| I/O relationship | Unencapsulated | Encapsulated | Model correlation |
|--|----------------|--------------|-----------------------------|
| Free deflection [$\mu\text{m}/\text{V}$] | 100 | 10 | good, predicts same trend |
| Charge sensing [$\mu\text{C}/\text{m}$] | 1 | 10 | poor, predicts equal values |
| Blocked force [$\mu\text{N}/\text{V}$] | 10 | ~ 80 | poor, predicts equal values |
| Stiffness [N/m] | 0.1 | 1.0 | good, predicted well |
| Electrical Impedance [V/A] | 200@1Hz | 200@1Hz | good, predicted well |

KaptonTM GHM Value Exploration

Since the predicted free deflection response for encapsulated transducers is overdamped through resonance for all cases, the variation in KaptonTM GHM parameters will be explored briefly in this section. The NafionTM GHM parameters will not be explored, but a similar effect occurs when they are varied. The transducer chosen for use in the investigation was encapsulated transducer III. Using the results from run 8 (ref. Table 3.2 and Figure 3.5) because it was the lowest loss factor found, results in the resonance peak being better represented in the distributed parameter model, see Figure 4.23.

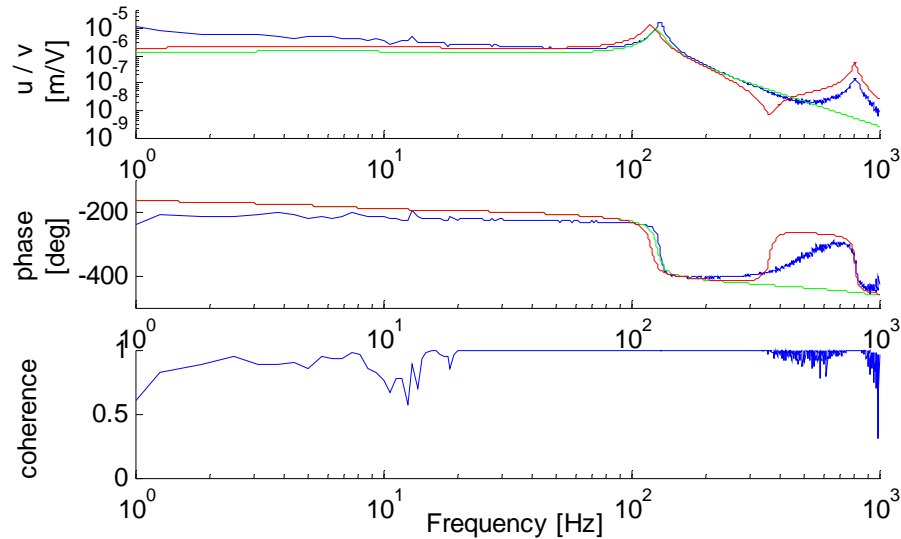


Figure 4.23: Free deflection of encapsulated transducer III with low KaptonTM GHM fit

The modeled resonant peak shows a higher Q, but the lower stiffness of the high frequency modulus results in a lower prediction of resonant frequency by 10% than was

measured experimentally. This trend is supported by the comparison of the predicted and measured stiffness resonant response of transducer III shown in Figure 4.24.

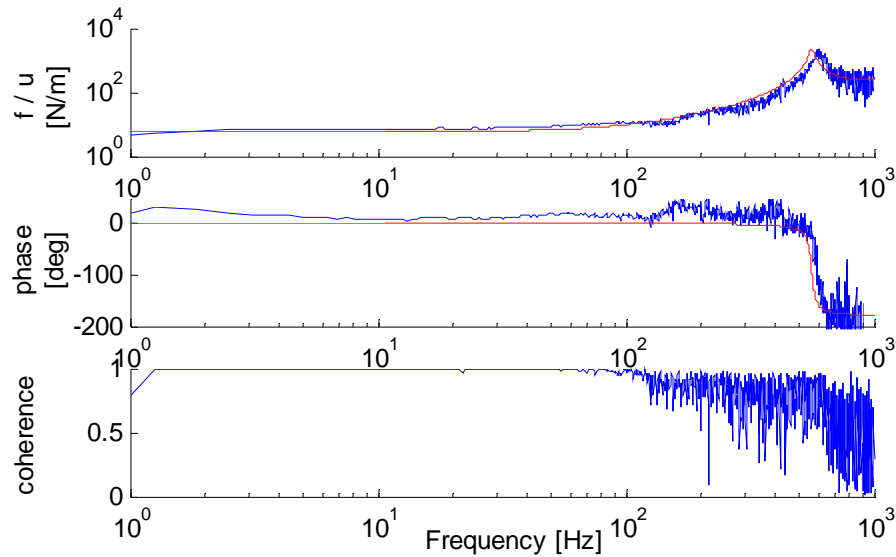


Figure 4.24: Stiffness of encapsulated transducer III with low Kapton™ GHM fit

This illustrates the some of the trade offs when selecting the GHM parameters of the materials. Some values found for the GHM parameters allow a better fit of some responses at the expense of others. The general results for free deflection in this work show an overdamped resonant response prediction by the model when compared to measured transducer response. This extra damping found in all tests other than free deflection could be caused by the testing setup. For example, friction between the beam and the load cell could be providing energy loss not present when the beam is cantilevered for free deflection testing.

4.4 Higher Frequency Data Observations

This section will discuss some interesting trends and phenomena seen in the data taken to 500Hz for the nonencapsulated transducers, and to 1kHz for the encapsulated transducers.

4.4.1 Non Encapsulated Transducers

For unencapsulated transducers in general, an accurate stiffness prediction will produce accurate free deflection resonant frequency predictions, and this is more sensitive in higher

modes. The majority of the problem in prediction of stiffness/free deflection natural frequency is in measuring geometry, possibly thickness reduction by electroding prep (sanding surface?). Generally, if in error, transducers are softer than predicted. The tests were performed without moving the sample for each run, so if L_d is off it will be off for all tests, this allows correlation between modulus and free deflection trends as well as the resonances seen in the sensing response (match stiffness resonances). The free deflection prediction is always overdamped for all tests at and near resonance. In general the zeros modeled in

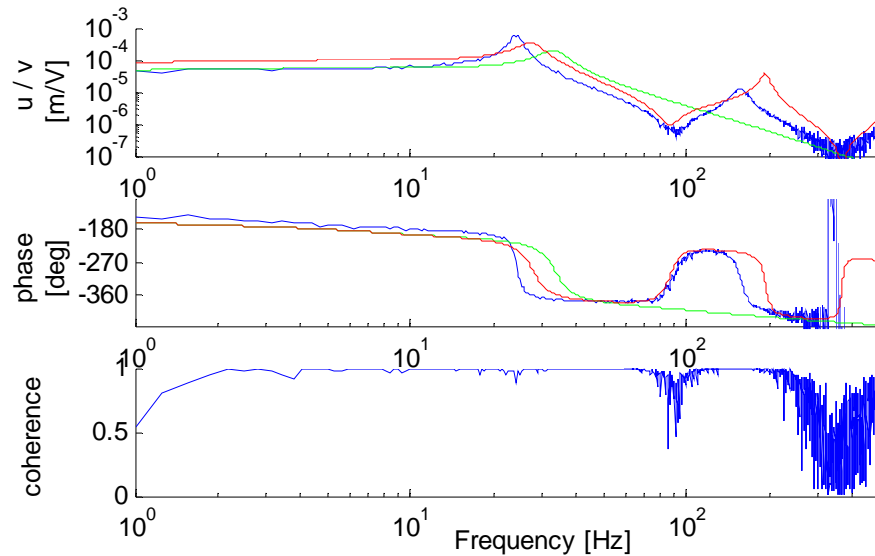


Figure 4.25: Free deflection response of unencapsulated transducer III, full frequency range: blue is data, red is distributed parameter model, green is lumped parameter equivalent.

the applied moment distributed parameter cantilever BC (used in free deflection) are only visible in some runs (transducer I and III) and this is independent of data coherence, ie the coherence is good in the range of zeros for the tests that don't show them. Figure 4.25 is plot of the free deflection of transducer III, note the phase of the measured response vs distributed parameter model. simulation.

The sensing tests in general for unencapsulated transducers show clear beam dynamics in the response. The resonant frequencies match measured stiffness resonance exactly, see Figure 4.26 and refer to Figure 4.3. To capture this phenomenon requires remodeling beyond just the equivalent circuit, the underlying coupling interaction needs to be re-evaluated to include beam dynamics of motion (not necessarily d function itself, just how it propagates through model and into the i/o relationships). The coupling d does really roll off with

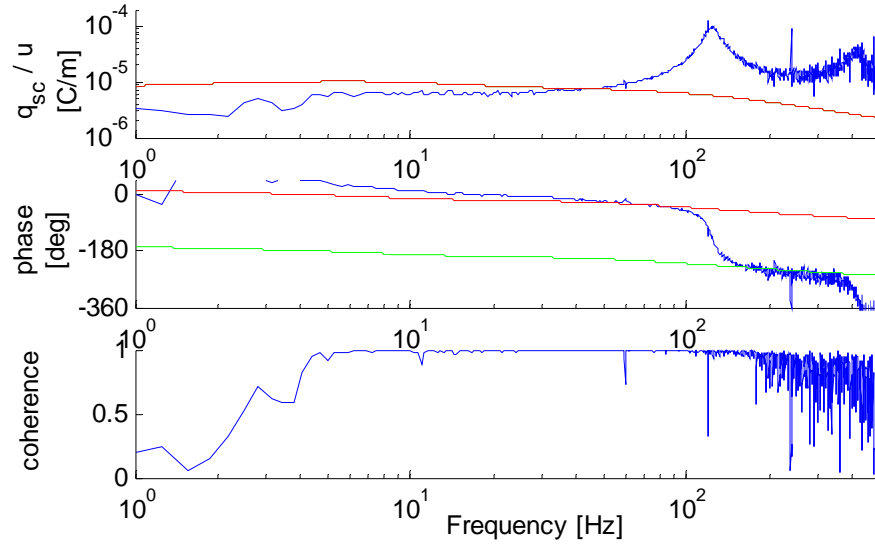


Figure 4.26: Sensing response of unencapsulated transducer I, full frequency range: blue is data, red is distributed parameter model, green is lumped parameter equivalent.

frequency, the sensing dynamics peak is lower at third mode than the second (not so in stiffness prediction and measurement). This is seen regardless of coherence (ie coherence is still good), transducer I is the only visible one, the rest of the runs have too poor of high frequency coherence in the sensing tests.

In general, there is definitely sensor dynamics in the blocked force response, this is inferred despite the low coherence of the higher frequency data. Note the peak frequency is the same as the response seen in sensing and in the mechanical stiffness results. This phenomena is also not possible to capture with current model. This would need at least a change of BC's, ie clamped, pinned with distributed moment forcing (consistent with cantilever), then coupling the applied moment to the applied voltage. It is probable that the same method that will model beam dynamics in the sensing response will also create them in the blocked force response.

All tests performed but plots omitted in the body of this work can be found in Appendix A for reference.

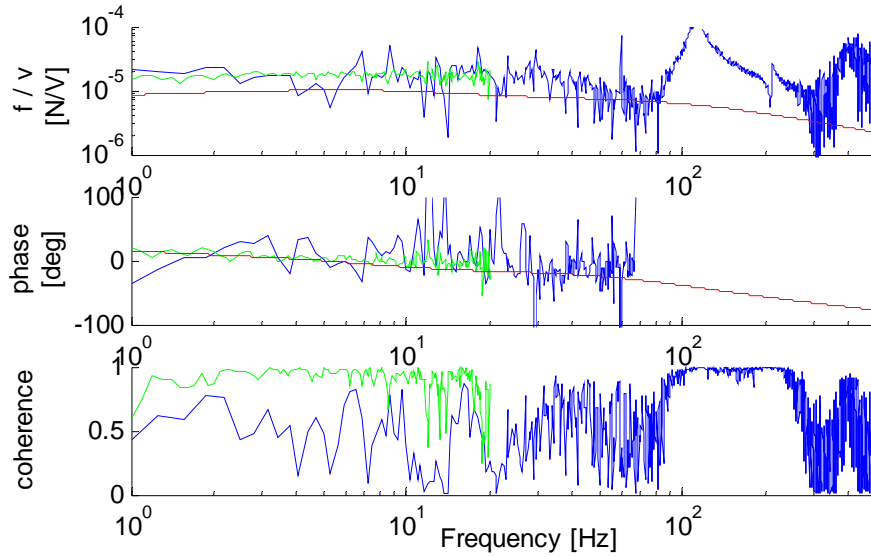


Figure 4.27: Blocked force response of unencapsulated transducer I, full frequency range.

4.4.2 Encapsulated Transducers

In general the performance of the transducers in this work were improved with encapsulation except for reduction in free deflection. The modulus predictions using the model are acceptable for all these runs, it shows in the good natural frequency prediction seen in the free deflection responses. The free deflection predictions in general correlate well with the model (looking at low frequency and around resonances). There are only zero's visible in one run, see Figure 4.28. There is also an expected response reduction of approximately an order of magnitude between the encapsulated and unencapsulated transducers, regardless of the predicted value comparison.

In general there are definite beam dynamics in the sensing response of the encapsulated transducers (again match the stiffness peaks, in frequency and shape). Refer to Figure 4.13 for stiffness results to compare to the sensing results plotted in Figure 4.29 for encapsulated transducer III. The sensing estimates are acceptable in general, encapsulated transducer I has issues but it is most likely due to the high impedance problem.

It is difficult to see beam dynamics in the blocked force response, but this makes sense since the beams are much stiffer when encapsulated and the induced moment from actuation can't cause as much beam flexure. The blocked force is generally an order of magnitude higher than the sensing response, the model predicts they would be the same.

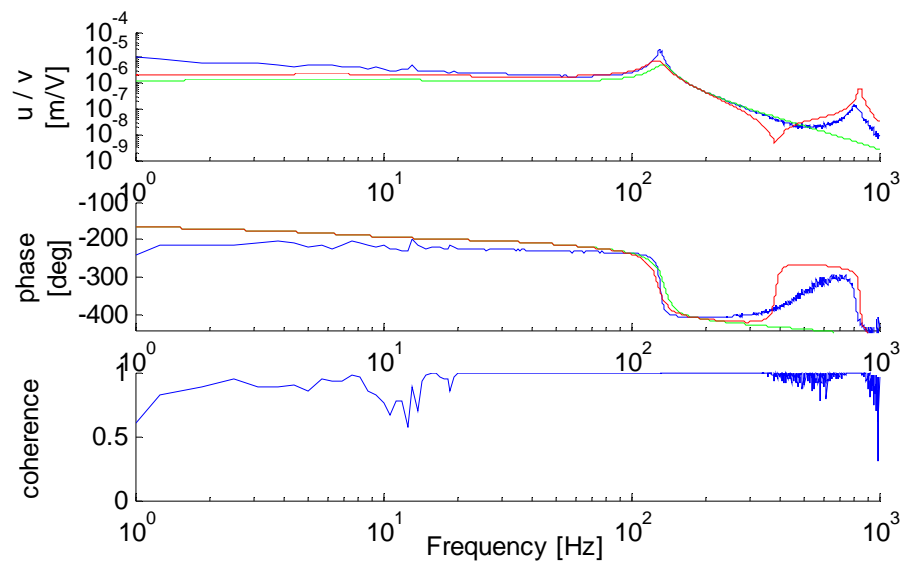


Figure 4.28: Free deflection response of encapsulated transducer III, full frequency range: blue is data, red is distributed parameter model, green is lumped parameter equivalent.

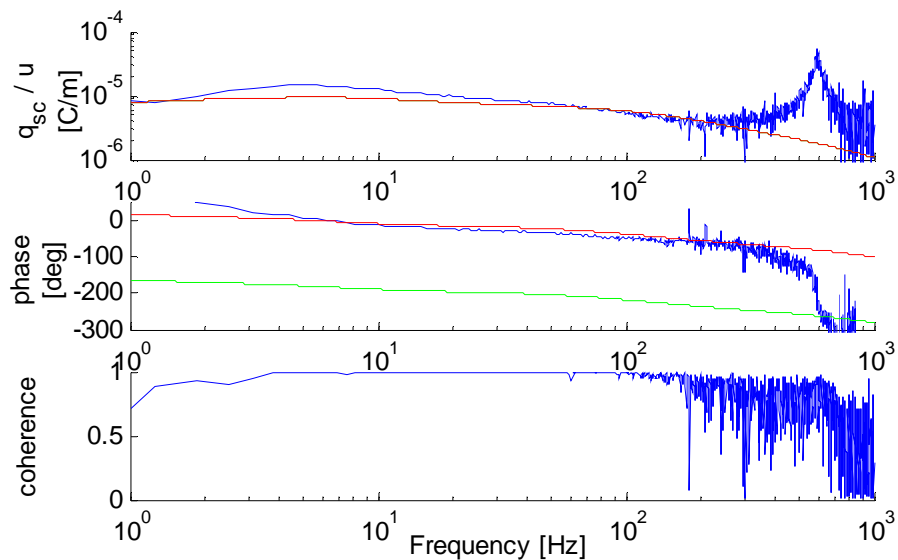


Figure 4.29: Sensing response of encapsulated transducer III, full frequency range: blue is data, red is distributed parameter model, green is lumped parameter equivalent.

Chapter 5

Discussion and Conclusions

This chapter will give a brief summary of the results and observations of this work as well as propose some possible future work.

5.1 Summary of Results

In this thesis a model was proposed to predict ionic polymer transducer performance with the addition of a passive encapsulation layer. This model is based on the work of Newbury (2002) with the addition of multi-layer beam theory and the utilization of distributed parameter system modeling to define the mechanical impedances and transfer functions of the transducer. The viscoelastic properties of NafionTM as they pertain to this work were investigated and a test method was proposed. This method was used to find the GHM parameters used in the model and validated with experimental data. Electrode stiffness effects were investigated through transducer stiffness measurements and explored with additional electroplating. This resulted in the justification of neglecting the electrodes as a mechanical layer in the model for the current manufacturing process (Bennett, 2002) and NafionTM thickness used in this work (NafionTM 117, 200 μ m thick). The proposed model was validated with test data taken from various transducers tested both before and after encapsulation with a 1 μ m thick KaptonTM film. Test fixture improvements allowed the extension of the frequency range of investigation above that of Newbury (2002) and Newbury and Leo (2003b). This range was divided into two ranges for comparison purposes, referred to as low and high. The low frequency range includes up to and including the first resonance of the transducer, which was ~ 50 Hz for unencapsulated and 200 Hz for

encapsulated transducers. The high frequency range extended to 500Hz for unencapsulated and 1kHz for encapsulated transducers.

The remainder of this section will summarize observations and conclusions made throughout this work. The trends predicted by the model between transducer performance before and encapsulation compared to the trends observed in experimental data will be the main focus.

The stiffness of transducers were increased by approximately a factor of 10 when encapsulated, this was predicted very well by the model. The typical values of stiffness for unencapsulated transducers were around 0.1 N/m and increased to around 1 N/m after the addition of KaptonTM film adhesive tape with thickness of 2 μ m of which 1 μ m was KaptonTM film.

A reduction in free deflection by an order of magnitude with encapsulation is predicted by the model and was observed in the experimental data. Typical low frequency deflections of 100 μ m/V were observed in unencapsulated transducers. The typical free deflection observed in encapsulated transducers was 10 μ m/V. For ionic polymer transducers in general, an accurate stiffness prediction will produce accurate free deflection resonant frequency predictions, and this is more sensitive in higher modes. Results presented in this thesis show a direct correlation between the accuracy of the stiffness measurement and the accuracy of the natural frequency prediction, as expected. The prediction of the stiffness and natural frequency response was better for encapsulated transducers presented in this work. The majority of the problem in prediction of stiffness/free deflection natural frequency is in measuring geometry, possibly thickness reduction by electroding preparation (sanding the surface of the polymer?). Generally, if in error, unencapsulated transducers are softer than predicted. The free deflection prediction is always overdamped for all tests at and near resonance.

The typical low frequency sensing response of unencapsulated transducers is $\sim 1\mu\text{C}/\text{m}$, this is approximately an order of magnitude below the typical observed encapsulated response of 10 $\mu\text{C}/\text{m}$. This is contrary to the model prediction of equal values (there is no encapsulation terms in the equation for charge sensing with a displacement input). The data was generally cleaner (higher coherence) for the encapsulated transducers than for the same transducer after encapsulation, this could have some effect on the values attained. The sensing tests in general show clear beam dynamics in the response, (the peaks match

measured stiffness response exactly). This is pronounced in the unencapsulated transducers where the beam is softer and more vibration amplitude occurs. To capture this phenomenon requires remodeling beyond just the equivalent circuit, underlying coupling interaction needs to be re-evaluated to include beam dynamics of motion (not necessarily d function itself, just how it propagates through model and into the i/o relationships). The coupling d does really roll off with frequency, the sensing dynamics peak is lower at third mode than the second (not present in stiffness prediction and measurement). This is seen regardless of coherence (ie coherence is still good). Transducer I is the only visible one of the unencapsulated transducers, and transducer III is the best example of the encapsulated transducers, the rest of the runs have too poor of high frequency coherence.

The blocked force typically seen in the unencapsulated transducers is about $10\mu\text{N}/\text{V}$, which is in contrast to the $80\text{-}100\mu\text{N}/\text{V}$ observed in the encapsulated transducers. This is consistent with the near order of magnitude increase in observed sensing response with encapsulation (charge sensing and blocked force are negative reciprocals in the model developed in this work). In general, there is definitely transducer dynamics in the blocked force response of unencapsulated transducers, this is also not possible to capture with current model. This would need at least a change of BC's, ie clamped, pinned with distributed moment forcing (consistent with cantilever), then coupling the applied moment to the applied voltage. It is probable that the same method that will model beam dynamics in the sensing response will also create them in the blocked force response. It is difficult to see beam dynamics in the blocked force response, but this makes sense since the beams are much stiffer encapsulated and the moment can't get as much beam flexure. The blocked force is generally an order of magnitude better than the sensing response, while the model predicts they would be the same.

The contributions of this work include:

- The development of a multi-layered-beam model to model the effects of the addition of an outer passive layer on ionic polymer transducer performance. This outer layer could be an encapsulation layer or possibly the transducer electrodes at lower transducer thickness.
- The Golla-Hughes-McTavish (GHM) method is applied to the characterization of the

viscoelastic properties of NafionTM and results are presented.

- The current ionic polymer test fixture is refined to address data quality issues and allow a higher frequency range of transducer response exploration.
- The valid frequency range of the model created is explored and phenomena observed gives further insight into the fundamental characteristics of ionic polymer transducers and how subsequent models may be improved to better model higher frequency macroscopic transducer response.

5.2 Future Work

This section will propose future work that would enhance the knowledge and understanding of ionic polymer transducer behavior and modeling. The model presented here, while extending the frequency range of validity for the mechanical impedance and incorporating a passive layer for encapsulation, does not address the coupling of these additional dynamics into transducer performance. The model this work was based on, (Newbury, 2002), assumes the coupling is through the static deflection of the beam and will never predict the mechanical resonances observed in all the sensing and some of the blocked force experiments. Perhaps a model derivation similar to that of a piezoelectric bimorph where the electromechanical coupling is introduced through the moment created by the forces at work microscopically in the transducer could give insight and additional modeling power.

Further work towards the baseline characterization of the material properties of saturated NafionTM, specifically the viscoelastic response and its change with hydration. This could possibly be accomplished through the generation of a test setup allowing the isolation of viscoelastic response specifically tailored toward ipmc uses. Better investigation of the value and form of the d function used as the main coupling mechanism in this model could possibly be better characterized and understood now that higher frequency response data is attainable.

The effects and applicability of electrode stiffness with smaller transducer thicknesses are still not well understood. While the electrodes were found to be neglectable in this work with the thickness of NafionTM used and the current electroding process, the motivation for this work was partly because of the reduction of free deflection in experimental vs predicted model results observed in 50 μ m thick ionic polymer transducers. The multilayer theory

here could be applied to an electrode layer easily and experiments performed to validate the correlation between electroding process and electrode thickness and effective stiffness.

Bibliography

Akle, B., 2003, **Multilayer Ionic Transducers**, M.S. Thesis, Virginia Polytechnic Institute and State University.

Bar-Cohen, Y., 2001, "Topic 1 Introduction," in: **Electroactive Polymer (EAP) Actuators as Artificial Muscles**, ed. Y. Bar-Cohen, SPIE press, pp. 20–34.

Bennett, M., 2002, **Manufacture and Characterization of Ionic Polymer Transducers Employing Non-Precious Metal Electrodes**, M.S. Thesis, Virginia Polytechnic Institute and State University.

Blevins, R. D., **Formulas for Natural Frequency and Mode Shape**, Krieger Publishing Company, Malabar, Florida, 1995.

Dupont, 2000a, **Kapton polyimide film, General Specifications**.

Dupont, 2000b, **NafionTM prefluorinated polymer products, Product Information**.

Fanson, J. and Caughey, T., Positive Position Feedback Control for Large Space Structures, **AIAA Journal**, Vol. 28, No. 4, pp. 717–724, 1990.

Gere, J. M. and Timoshenko, S. P., **Mechanics of Materials**, Fourth Edition, PWS Publishing Company, Boston, MA, 1997.

Inman, D., **Engineering Vibrations**, Second Edition, Prentice-Hall, Upper Saddle River, NJ, 2001.

Kanno, R., Kurata, A., Hattori, M., Tadokoro, S., Takamori, T., and Oguro, K., Characteristics and Modeling of ICPF Actuator, **Proc. Japan-USA Symposium on Flexible Automation**, pp. 691–698, 1994.

- Macosko, C. W., **Rheology: Principles, Measurements, and Applications**, Wiley-VCH, New York, 1993.
- McTavish, D. and Hughes, P., Modeling of Linear Viscoelastic Space Structures, **Journal of Vibration and Acoustics**, Vol. 115, pp. 102–110, 1993.
- Nemat-Nasser, S., Micro-mechanics of actuation of ionic polymer-metal composites, **Journal of App. Physics**, Vol. 92, No. 5, pp. 2899–2915, 2002.
- Nemat-Nasser, S. and Li, J. Y., Electromechanical response of ionic polymer-metal composites, **Journal of App. Physics**, Vol. 87, No. 1, pp. 3321–3331, 2000.
- Nemat-Nasser, S. and Thomas, C. W., 2001, “Topic 6 Ionomeric Polymer-Metal Composites,” in: **Electroactive Polymer (EAP) Actuators as Artificial Muscles**, ed. Y. Bar-Cohen, SPIE press, pp. 140–191.
- Newbury, K., 2002, **Characterization, Modeling, and Control of Ionic Polymer Transducers** Ph.D. Thesis, Virginia Polytechnic Institute and State University.
- Newbury, K. M. and Leo, D. J., Linear Electromechanical Model of Ionic Polymer Transducers Part I: Model Development (Revised), **to appear, Journal of Intelligent Material Systems and Structures**, 2003a.
- Newbury, K. M. and Leo, D. J., Linear Electromechanical Model of Ionic Polymer Transducers Part II: Experimental Validation (Revised), **to appear, Journal of Intelligent Material Systems and Structures**, 2003b.
- Shahinpoor, M., Bar-Cohen, Y., Simpson, J., and Smith, J., Ionic Polymer-Metal Composites (IPMC) As Biomimetic Sensors, Actuators, and Artificial Muscles – A Review, **Journal of Intelligent Materials and Smart Structures**, Vol. 7, pp. R15–R30, 1998.
- Tadokoro, S., Yamagami, S., Takamori, T., and Oguro, K., Modeling of Nafion-Pt composite actuators (ICPF) by ionic motion, **SPIE Proceedings**, Vol. 3987, pp. 92–102, 2000.
- Techniques, T., 2000, **TMO-1 Amplifier/Conditioner Module, Operators Manual**.

Uan-Zo-li, J. T., 2001, **The Effects of Structure, Humidity and Aging on the Mechanical Properties of Polymeric Ionomers for Fuel Cell Applications**, M.S. Thesis, Virginia Polytechnic Institute and State University.

Appendix A

Full Results Plots

The data used for the plots presented in this appendix are located in the 'final' folder under the 'thesis data' folder on the CD given to Dr. Leo. The Matlab file to create them is in the 'finaltest' folder in the 'matlabmodels' folder and is called 'model and plots results.m'. The file 'model and plot results big.m' places all the plots for each run on the same big plot instead of creating individual plots. All matlab figures used in this thesis are in the 'figures for thesis' folder in the 'final' directory. For a more detailed explanation of the CD contents, see the README file on the CD.

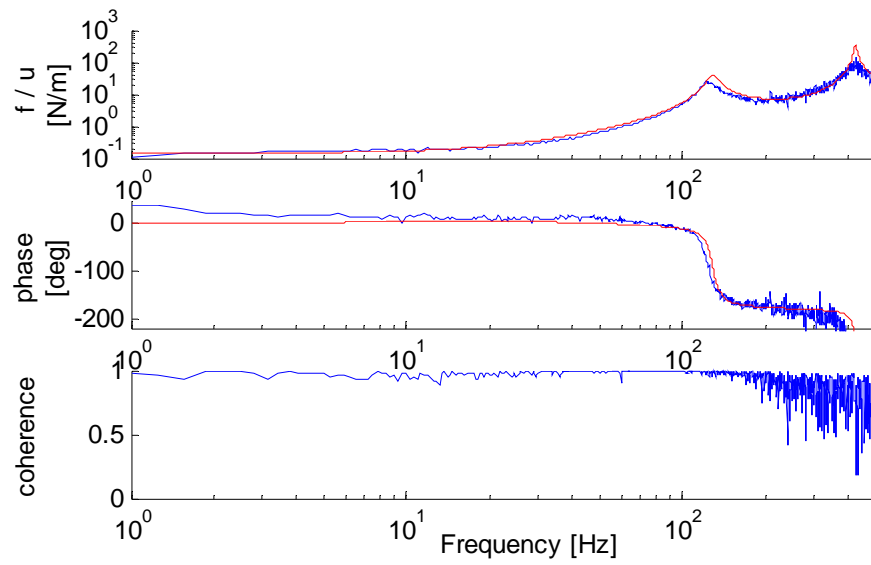


Figure A.1: Unencapsulated transducer I stiffness.

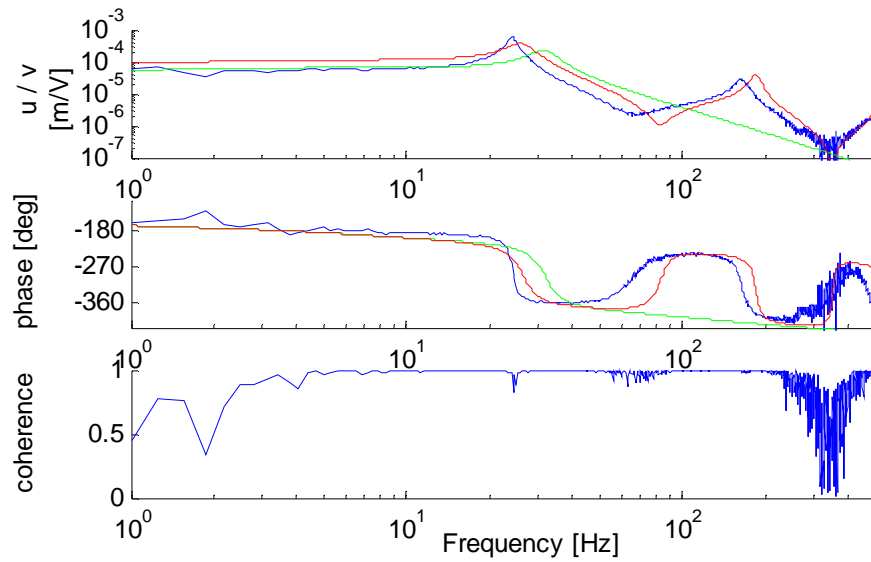


Figure A.2: Unencapsulated transducer I free deflection.

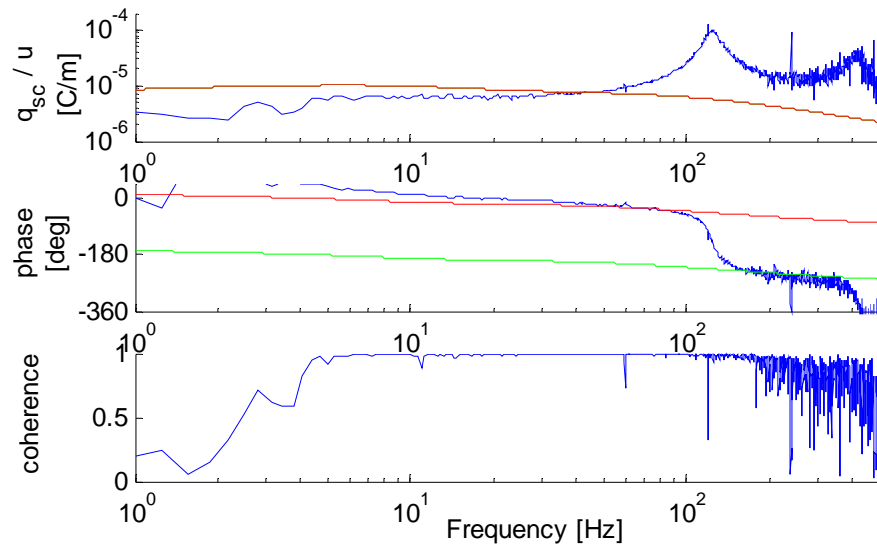


Figure A.3: Unencapsulated transducer I charge sensing.

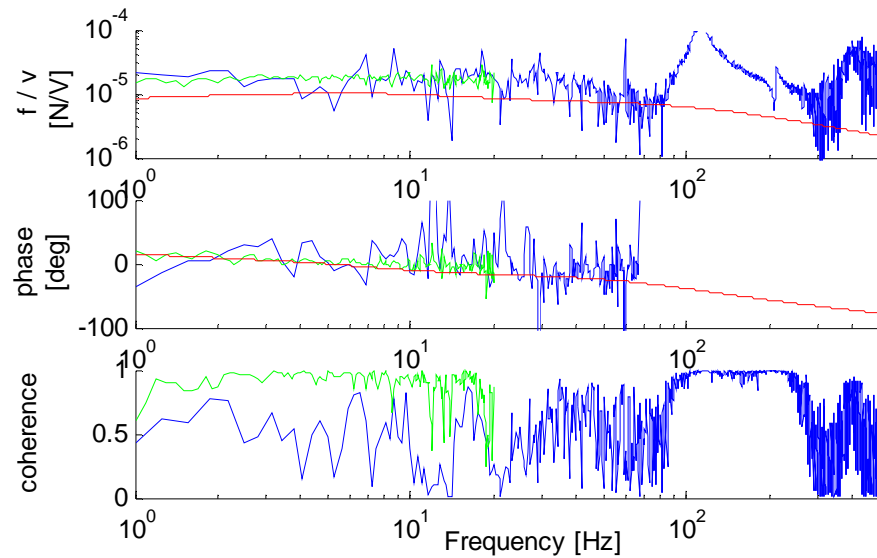


Figure A.4: Unencapsulated transducer I blocked force.

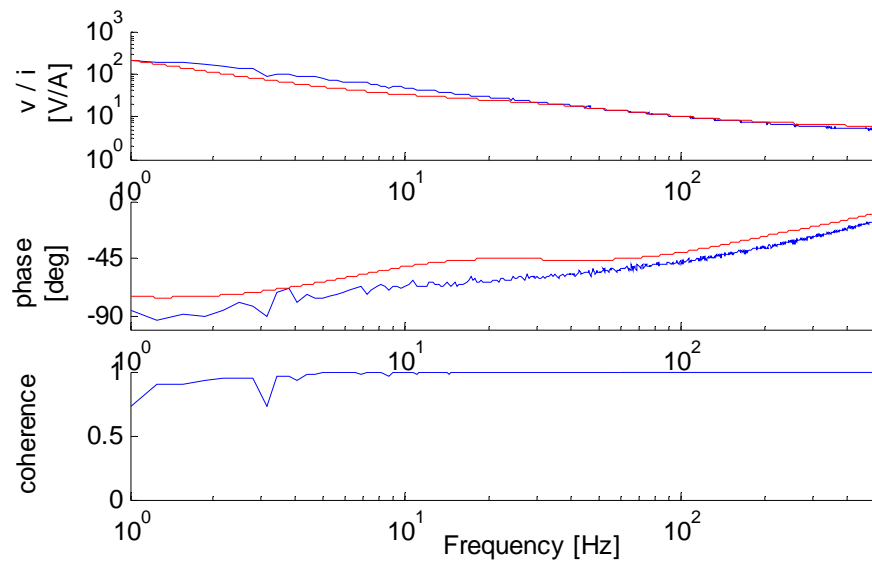


Figure A.5: Unencapsulated transducer I electrical impedance.

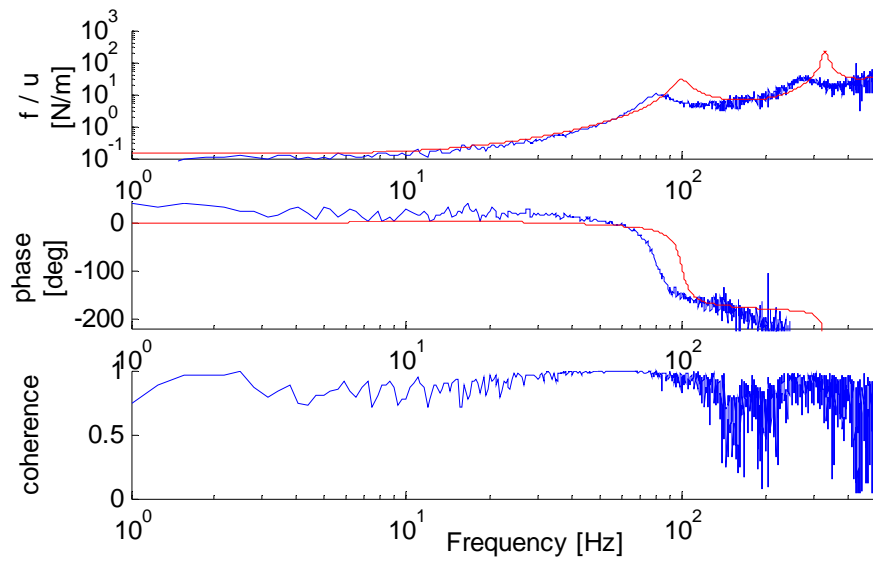


Figure A.6: Unencapsulated transducer II stiffness.

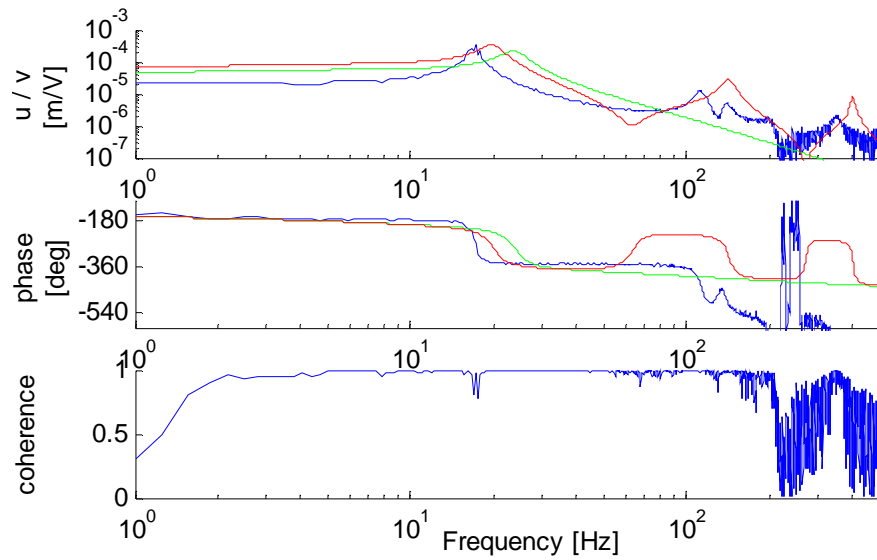


Figure A.7: Unencapsulated transducer II free deflection.

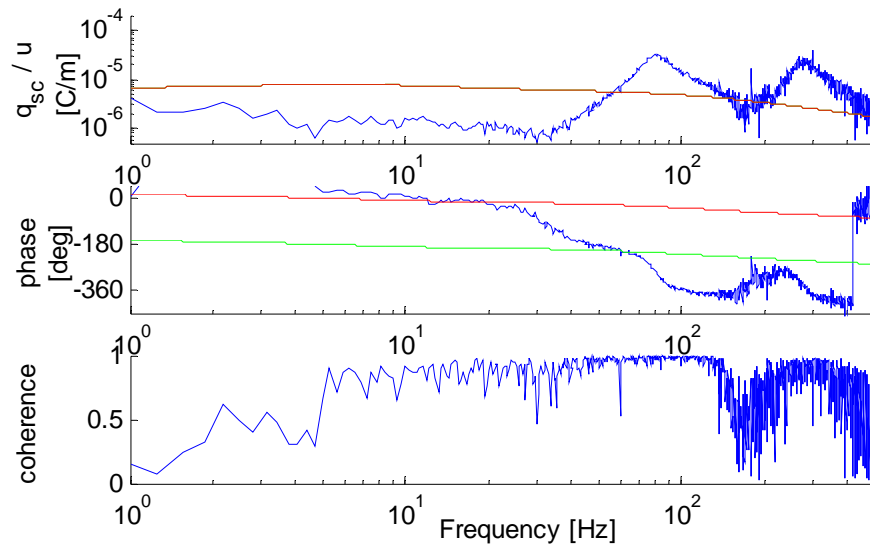


Figure A.8: Unencapsulated transducer II charge sensing.

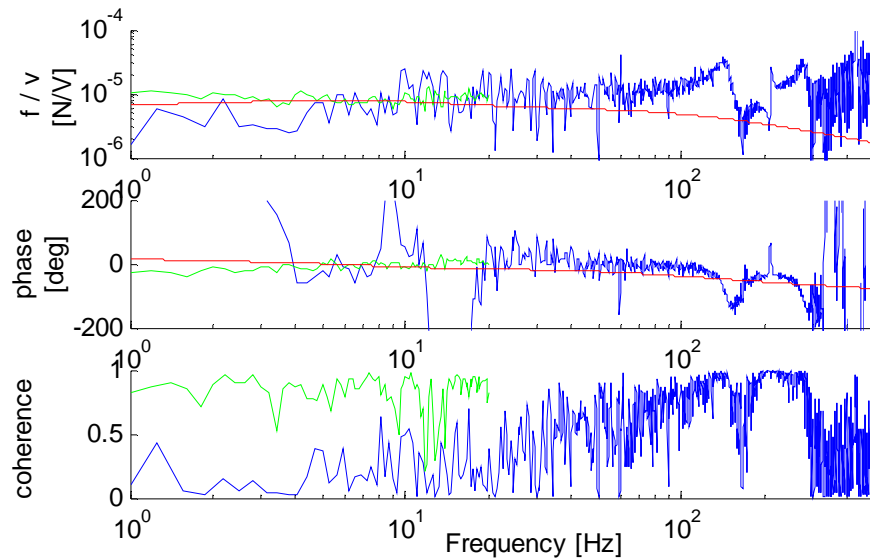


Figure A.9: Unencapsulated transducer II blocked force.

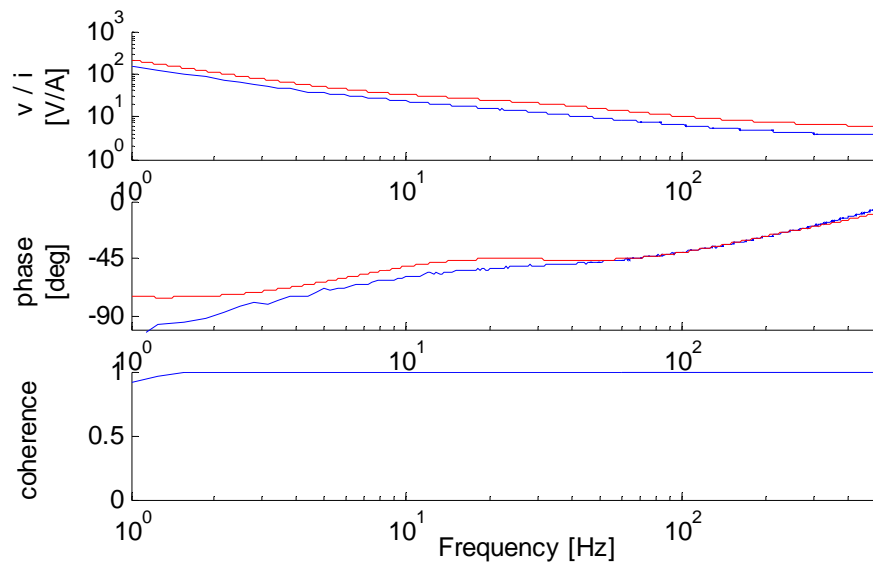


Figure A.10: Unencapsulated transducer II electrical impedance.

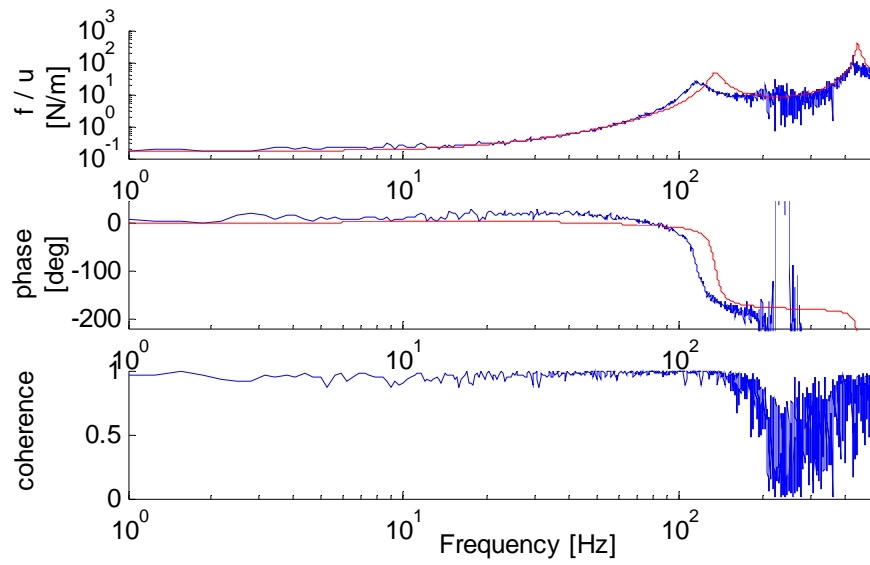


Figure A.11: Unencapsulated transducer III stiffness.

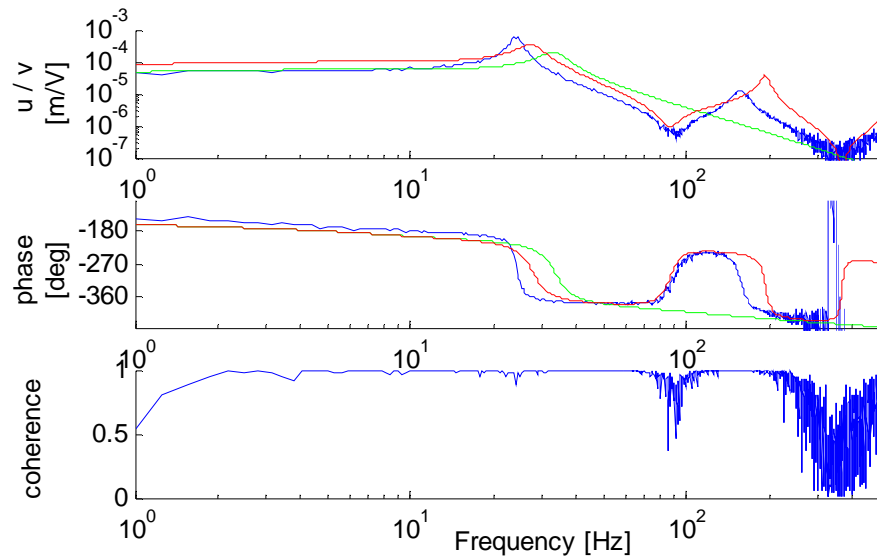


Figure A.12: Unencapsulated transducer III free deflection.

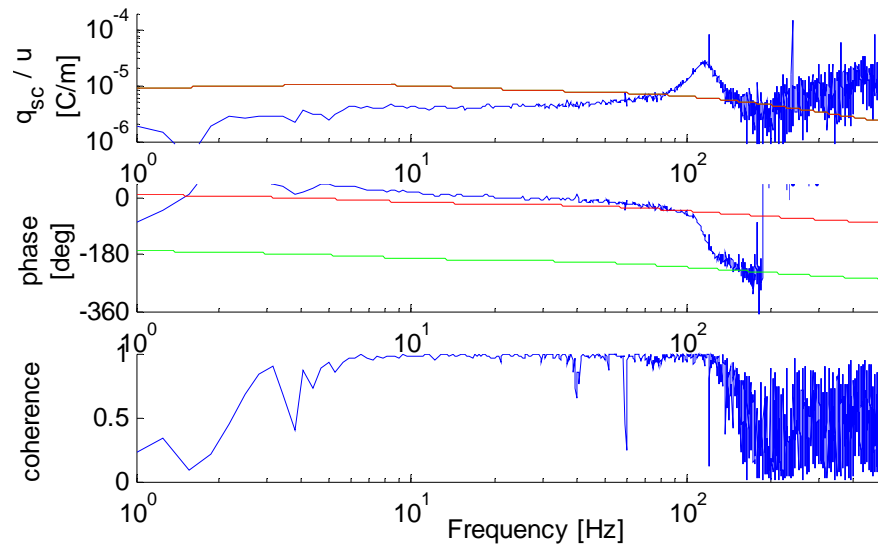


Figure A.13: Unencapsulated transducer III charge sensing.

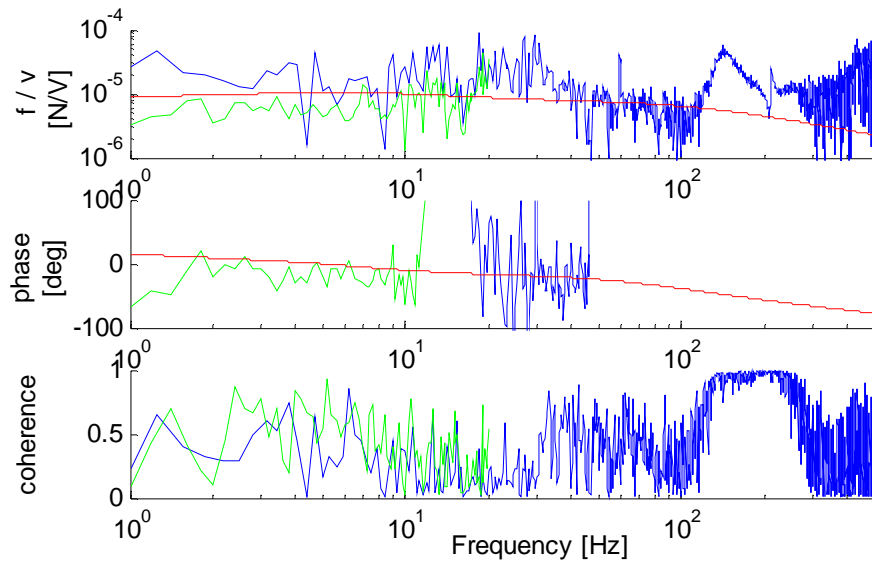


Figure A.14: Unencapsulated transducer III blocked force.

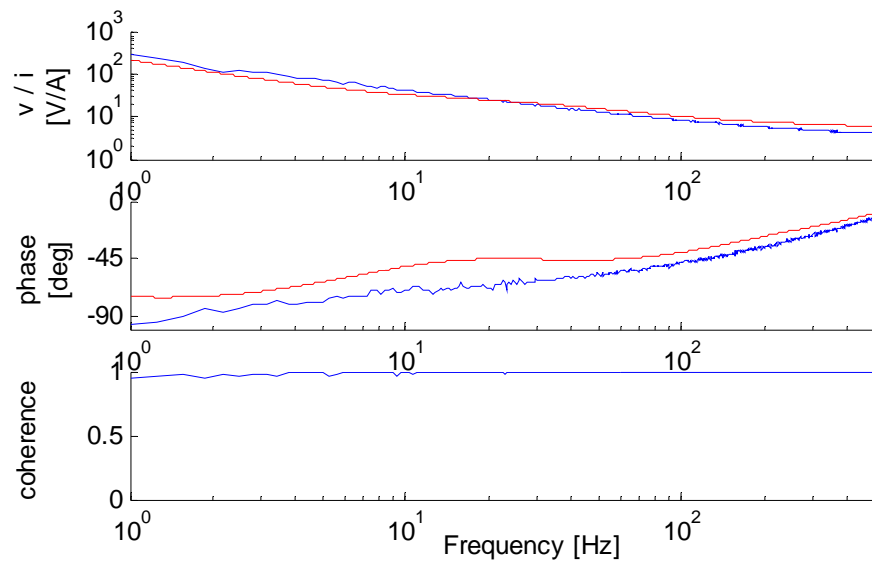


Figure A.15: Unencapsulated transducer III electrical impedance.

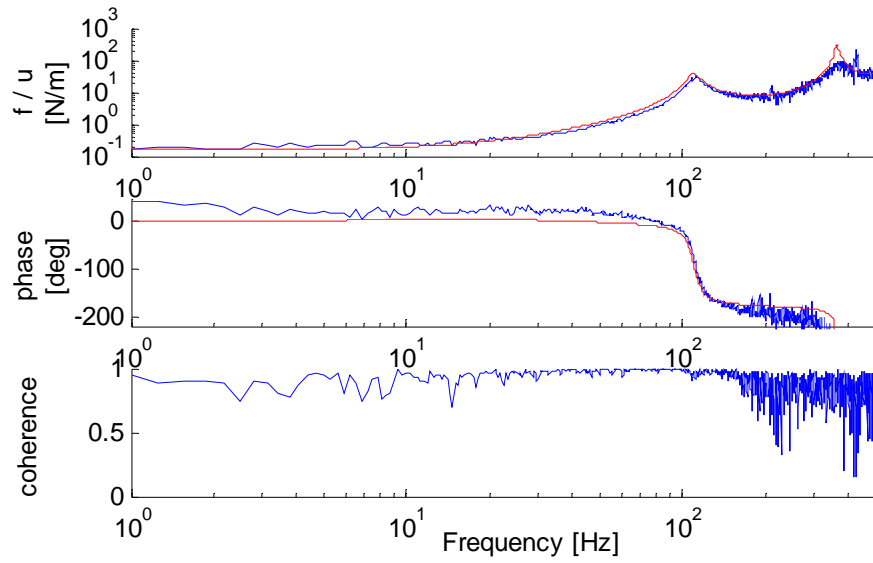


Figure A.16: Unencapsulated transducer IV stiffness.

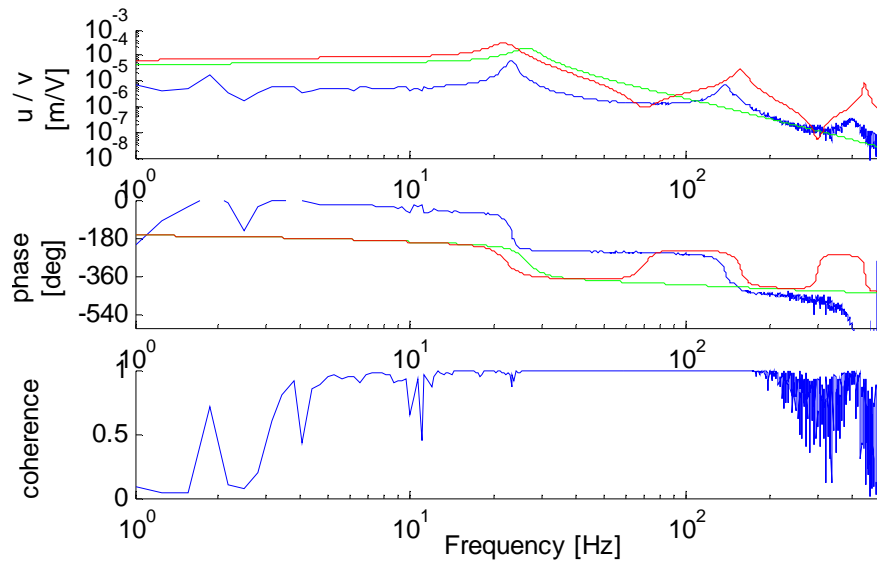


Figure A.17: Unencapsulated transducer IV free deflection.

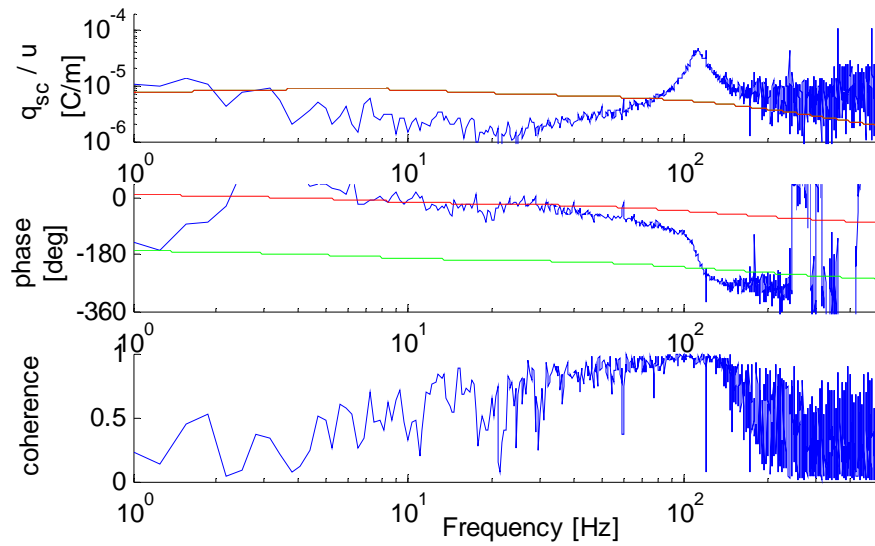


Figure A.18: Unencapsulated transducer IV charge sensing.

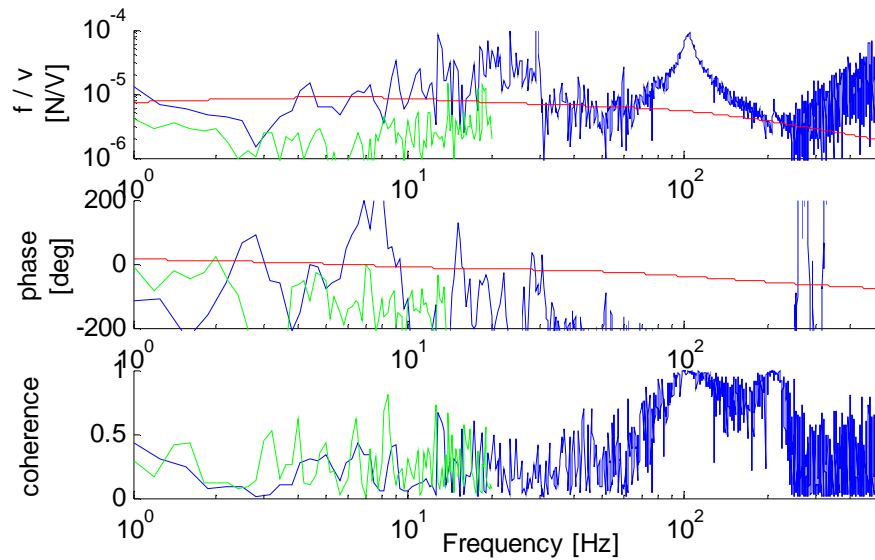


Figure A.19: Unencapsulated transducer IV blocked force.

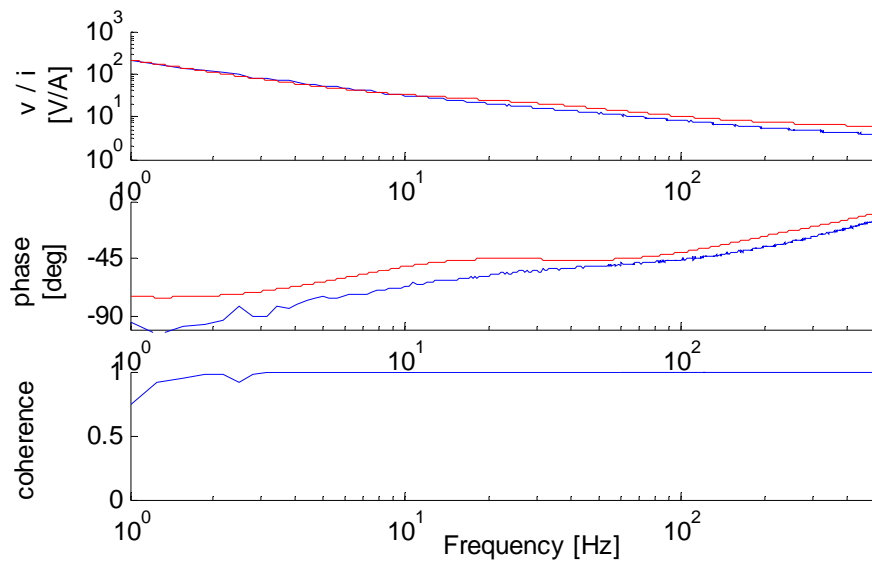


Figure A.20: Unencapsulated transducer IV electrical impedance.

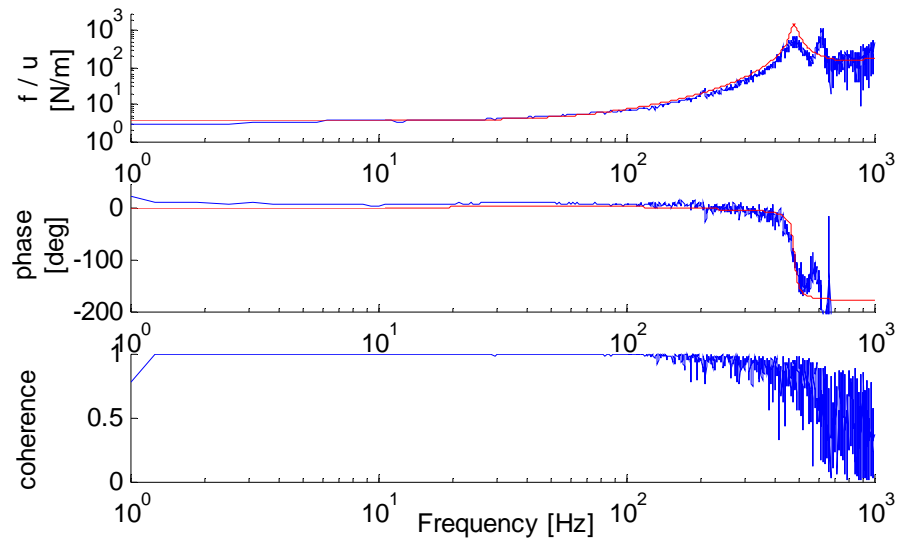


Figure A.21: Encapsulated transducer I stiffness.

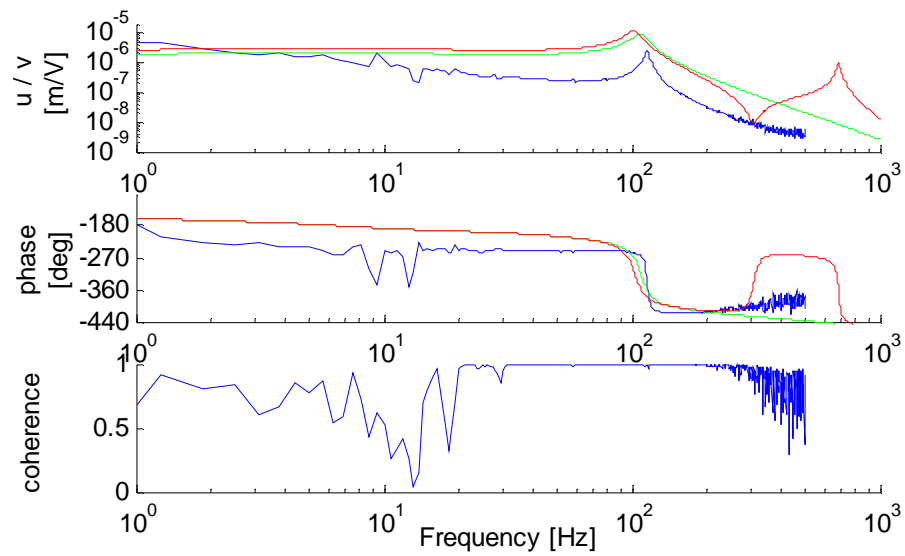


Figure A.22: Encapsulated transducer I free deflection.

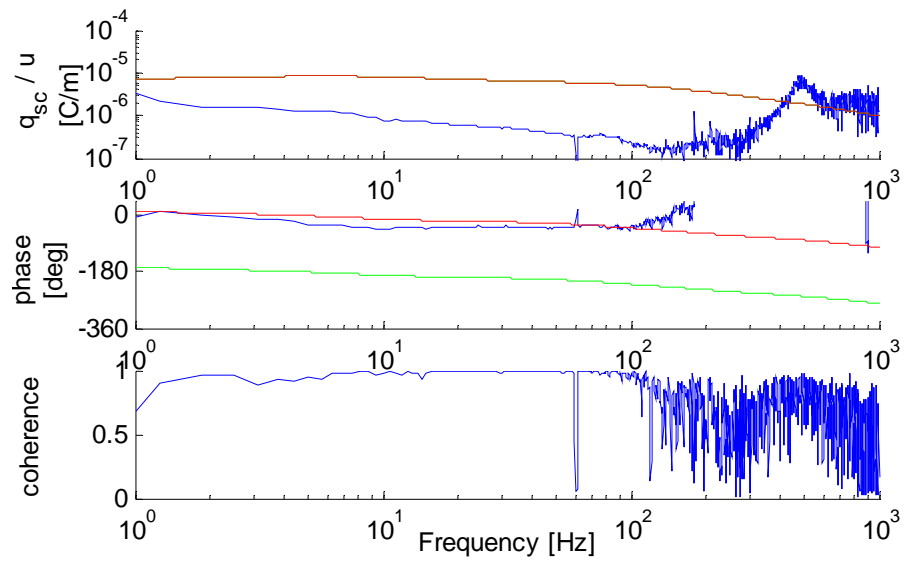


Figure A.23: Encapsulated transducer I charge sensing.

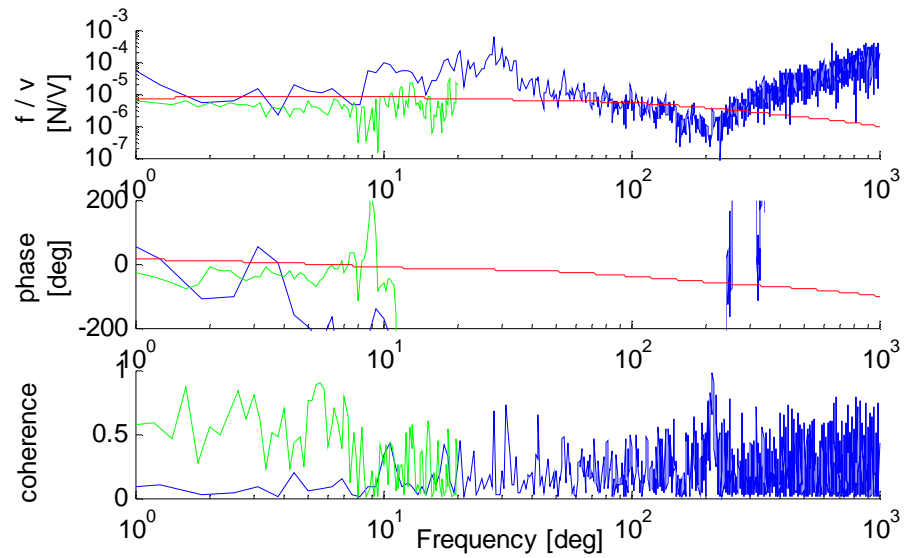


Figure A.24: Encapsulated transducer I blocked force.

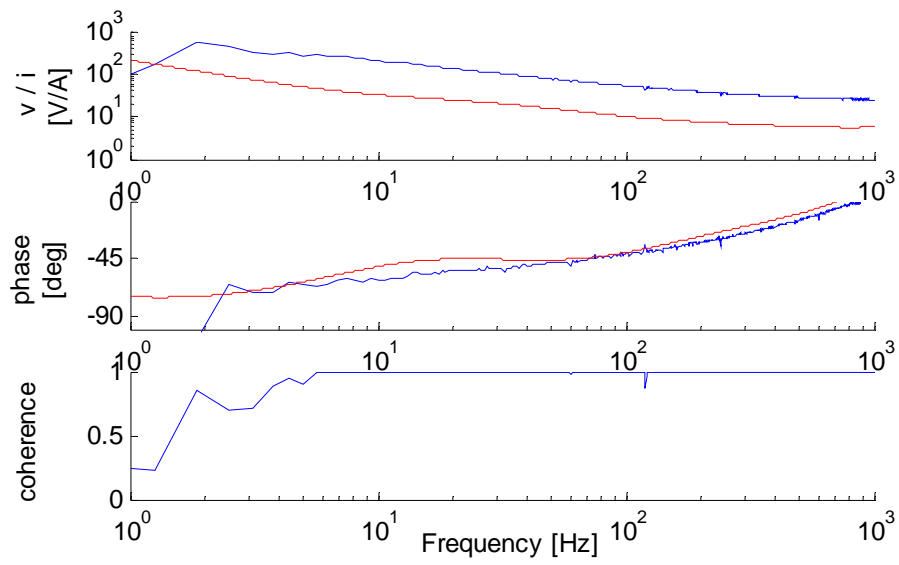


Figure A.25: Encapsulated transducer I electrical impedance.

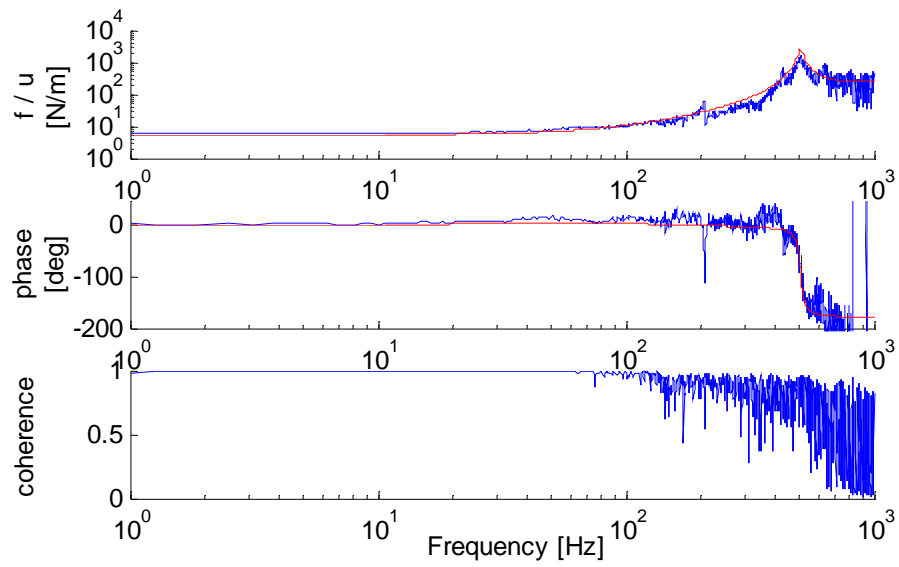


Figure A.26: Encapsulated transducer II stiffness.

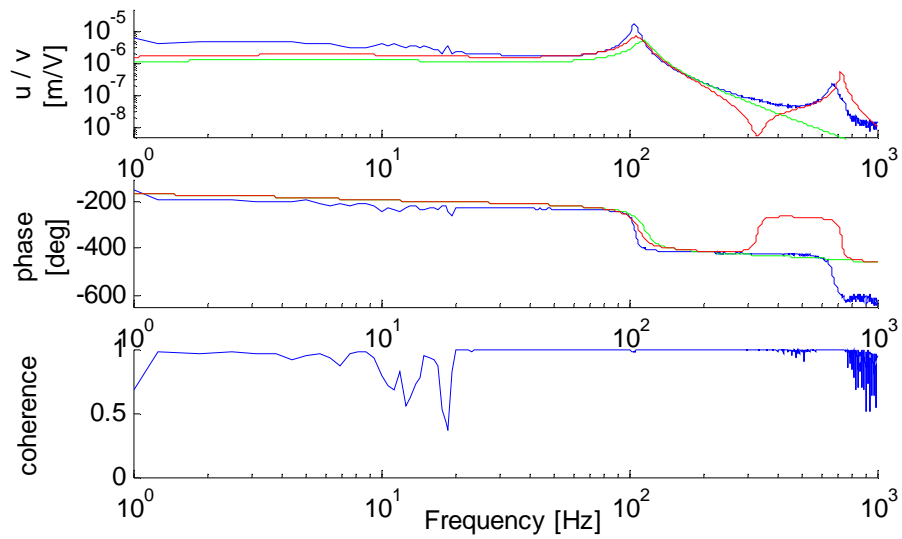


Figure A.27: Encapsulated transducer II free deflection.

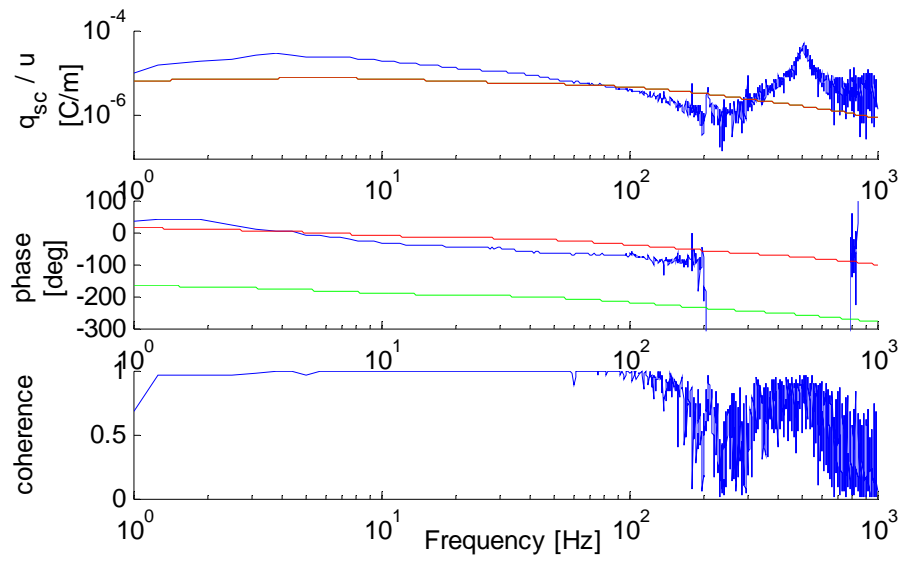


Figure A.28: Encapsulated transducer II charge sensing.

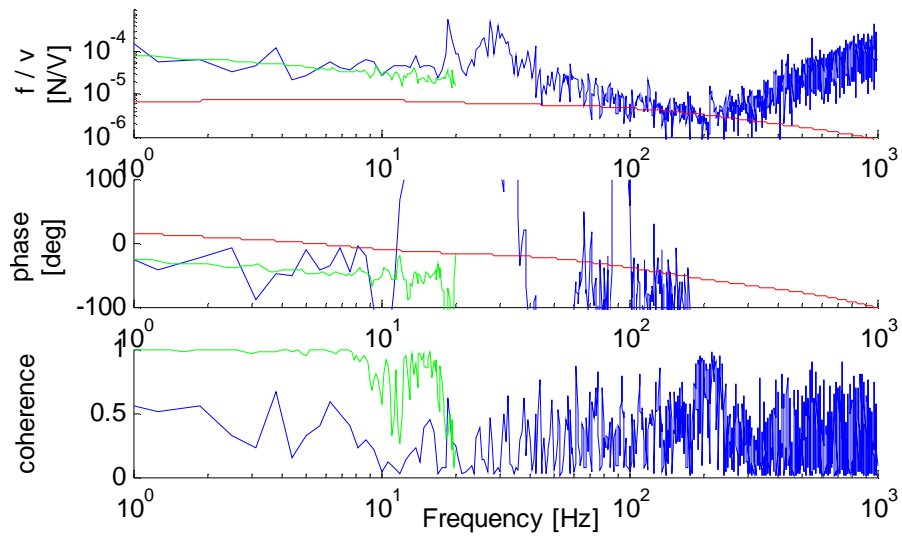


Figure A.29: Encapsulated transducer II blocked force.

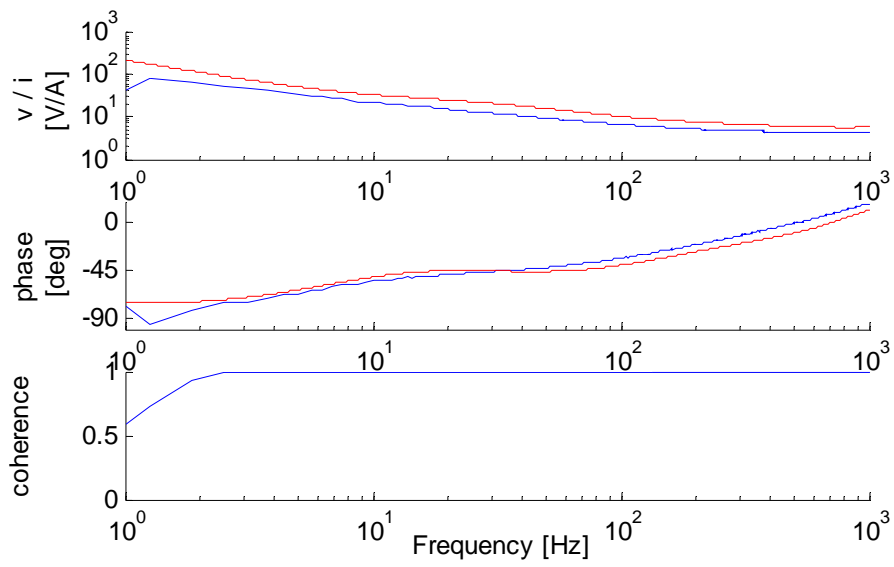


Figure A.30: Encapsulated transducer II electrical impedance.

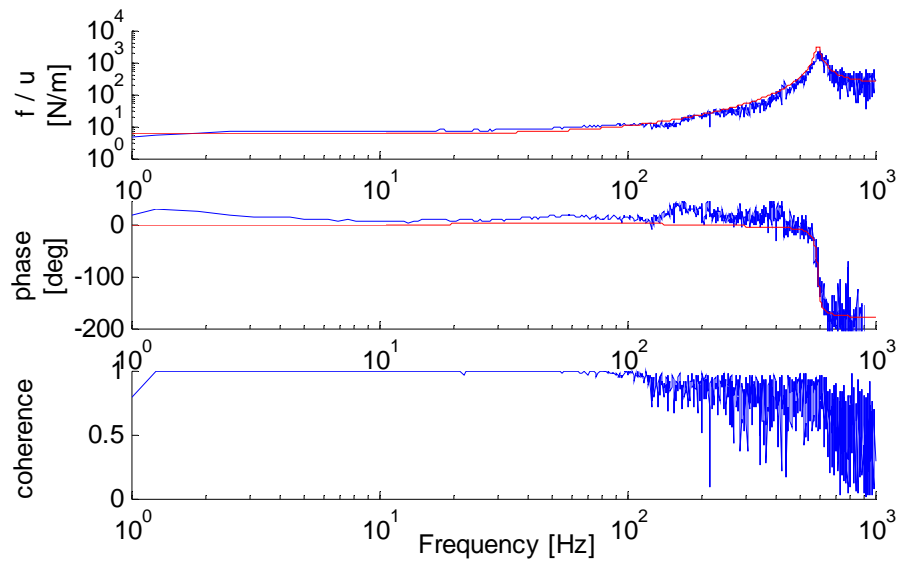


Figure A.31: Encapsulated transducer III stiffness.

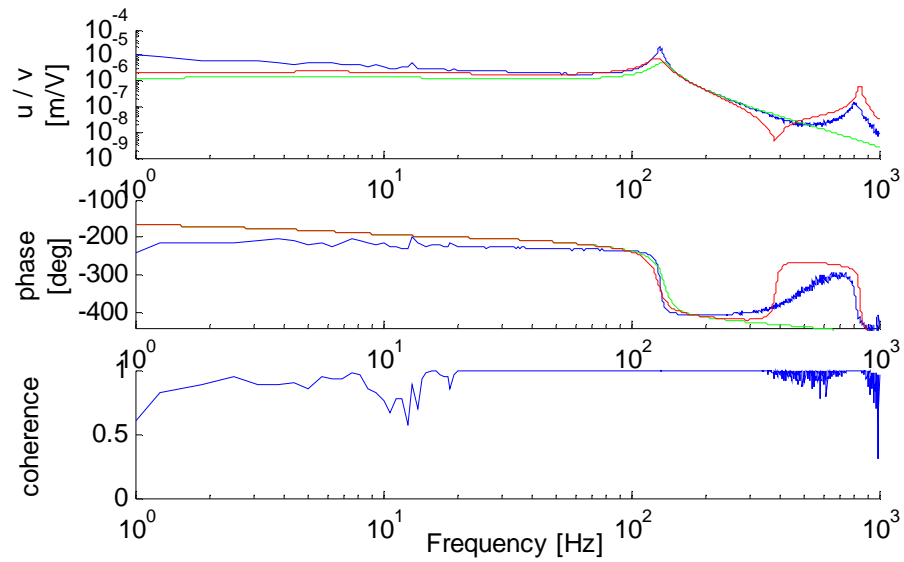


Figure A.32: Encapsulated transducer III free deflection.

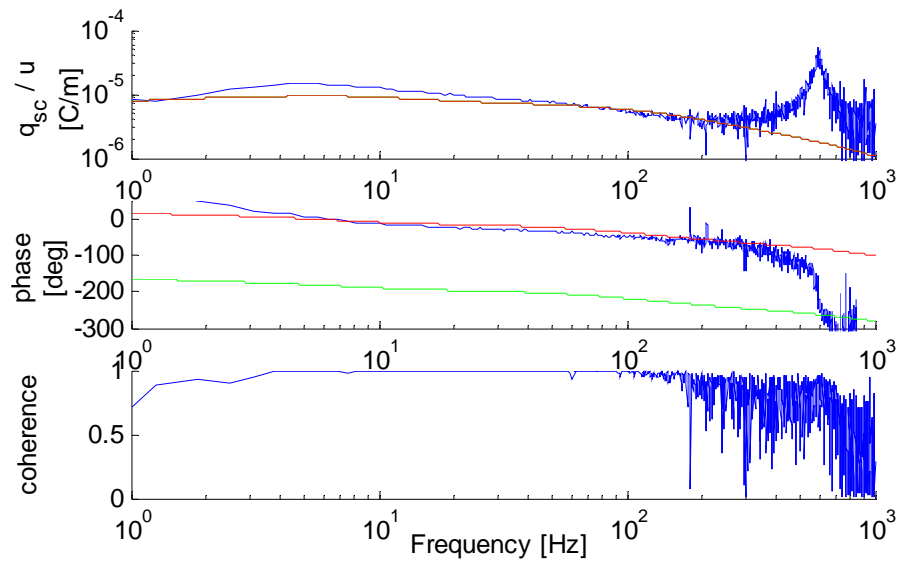


Figure A.33: Encapsulated transducer III charge sensing.

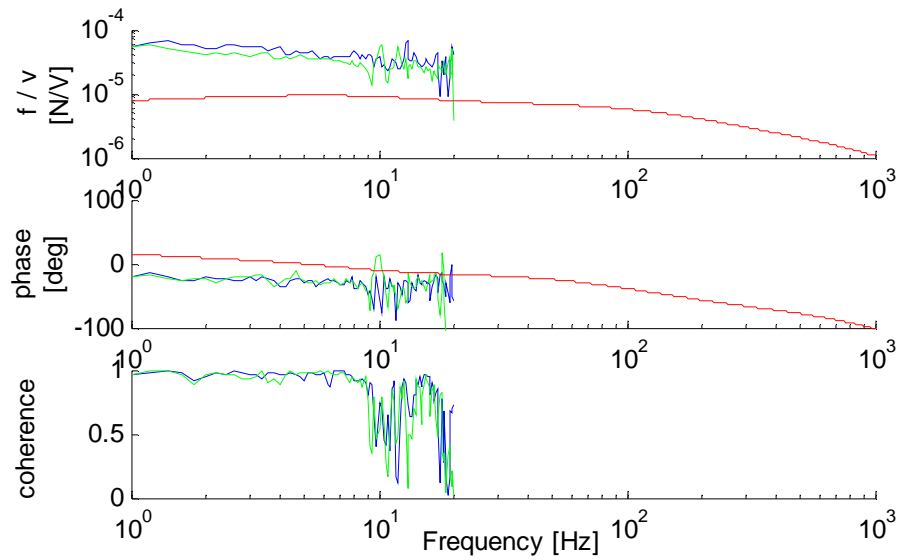


Figure A.34: Encapsulated transducer III blocked force.

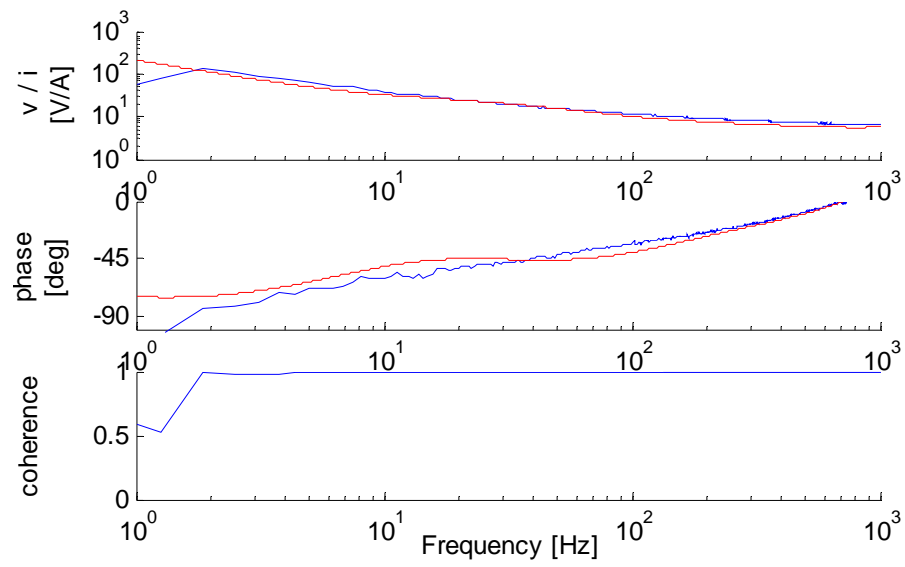


Figure A.35: Encapsulated transducer III electrical impedance.

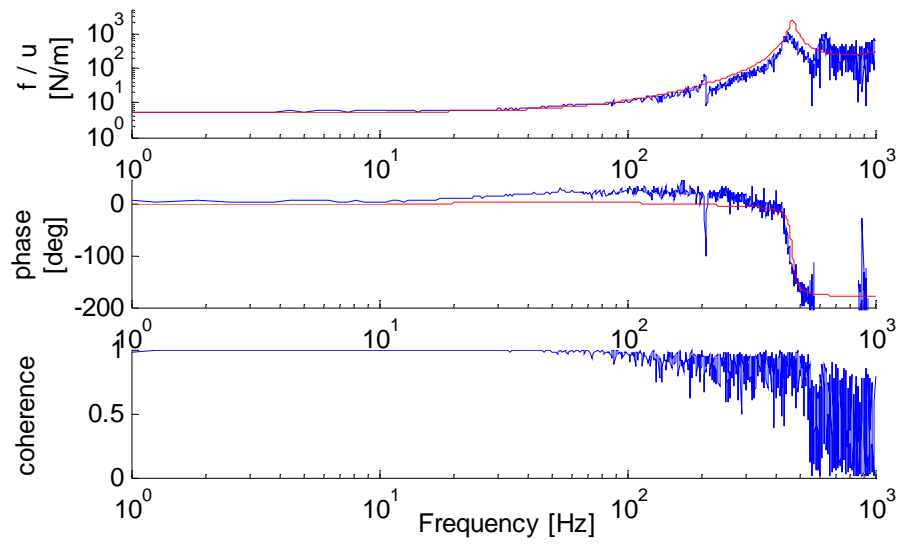


Figure A.36: Encapsulated transducer IV stiffness.

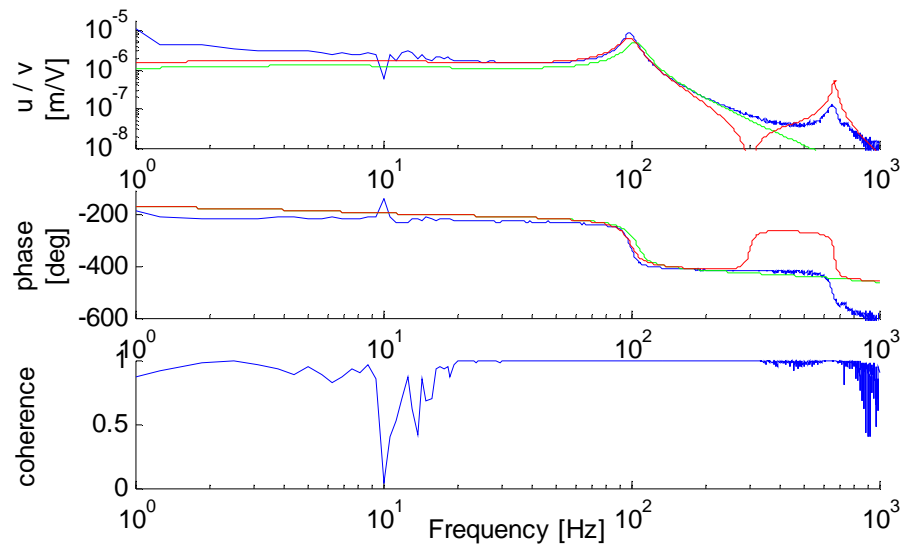


Figure A.37: Encapsulated transducer IV free deflection.

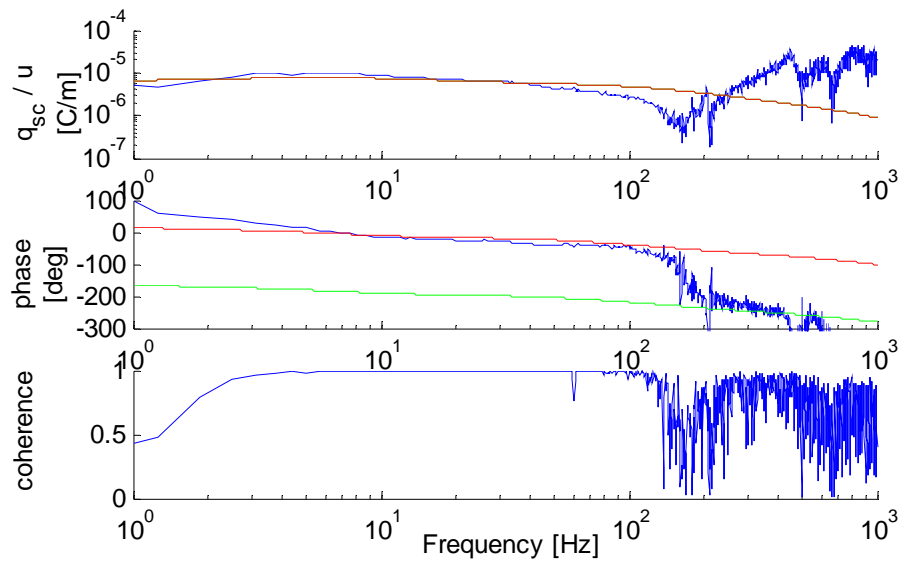


Figure A.38: Encapsulated transducer IV charge sensing.

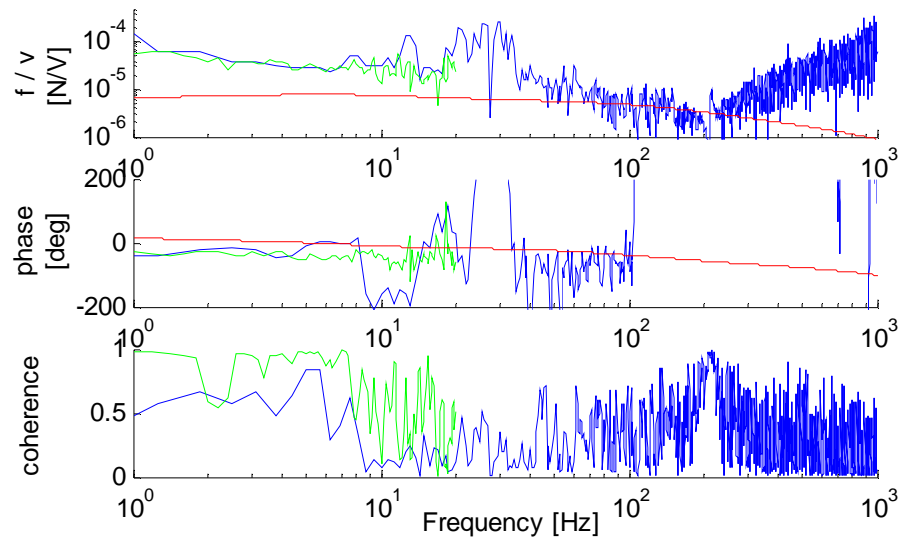


Figure A.39: Encapsulated transducer IV blocked force.

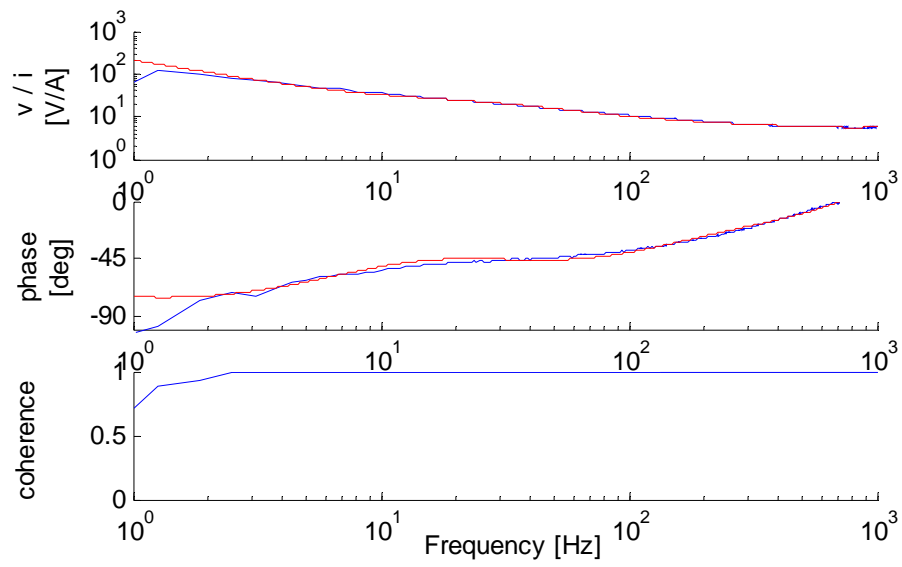


Figure A.40: Encapsulated transducer IV electrical impedance.

Vita

John Wesley Franklin was born on October 25, 1977 to Wesley and Janel Franklin in San Diego, California. He grew up in Carson City, Nevada and graduated from Carson City High School in May of 1996. The following August he began his college education at the University of Nevada, Reno. He interned at Bently Nevada Corporation during breaks throughout his undergraduate education. He recieved his Bachelor of Science degree in Mechanical Engineering with High Distinction in December of 2000 from the University of Nevada, Reno, and then accepted a Mechanical Engineer position at Bently Nevada. During the summer of 2001 he married Jennifer Smith and they moved to Virginia in August 2001 to persue Master of Science degrees at Virginia Polytechnic Institute and State University. John accepted a TA offer from the Mechanical Engineering Dept. at Virginia Tech and worked under Dr. Harry Robertshaw as a TA for ME senior Lab for the Fall of 2001. He began his research spring of 2002 under the guidance of Dr. Donald Leo in the Center for Intelligent Materials and Smart Structures (CIMSS) in the field of MEMS microfilter arrays, then changed to the study of ionic polymer transducers during the summer of 2002.

Address: Center for Intelligent Material Systems and Structures
310 Durham Hall
Blacksburg, VA 24061

This thesis was typeset with $\text{\LaTeX} 2_{\epsilon}$ ¹ by the author.

¹ $\text{\LaTeX} 2_{\epsilon}$ is an extension of \LaTeX . \LaTeX is a collection of macros for \TeX . \TeX is a trademark of the American Mathematical Society. The macros used in formatting this thesis were written by Greg Walker, Department of Mechanical Engineering, Virginia Tech.